Examining the consistency between subglacial hydrology and basal friction inversion modeling for Slessor Glacier, East Antarctica

by

Dylan Ruth

A thesis
presented to the University of Waterloo
in fulfillment of the
thesis requirement for the degree of
Master of Mathematics
in
Applied Mathematics

Waterloo, Ontario, Canada, 2022

Author's Declaration

I hereby declare that I am the sole author of this thesis. This is a true copy of the thesis, including any required final revisions, as accepted by my examiners.

I understand that my thesis may be made electronically available to the public.

Abstract

In light of rising global surface temperatures and sea-level rise, it is more important now than ever to understand what role the cryosphere will play in the Earth's evolution. The Antarctic ice sheet contains enough ice to raise the global sea-level by approximately 58 m, and for this reason alone, it is essential for scientists to be able to predict how the ice masses within will behave in the future. One way to study the future behaviour of glaciers and ice sheets is by applying geospatial data to mathematical models based on the relevant physics. In this thesis, the Glacier Drainage System model (GlaDS) and the Ice-sheet and Sea-level System Model (ISSM) are used to model subglacial hydrology and ice dynamics, respectively, for Slessor Glacier, East Antarctica.

First, an in-depth description of the necessary physics and numerical framework governing the two models is presented. With this framework in place, a sensitivity test comprised of 48 transient runs is performed with the GlaDS model, and 13 inversion simulations are performed with ISSM. The sensitivity test consists of altering several poorly constrained parameters to understand their impact on the modeled hydrological network beneath Slessor Glacier. The results from the sensitivity test are then used to determine which model configuration is most appropriate based on the current understanding of subglacial networks beneath the Antarctic Ice Sheet. However, this is a limited method of model validation in the absence of observed data such as specularity content (data derived from geophysical radar surveys to determine locations of distributed subglacial water). To mediate this issue, the model outputs from the inversion simulations, observed ice sheet melt rates, and a hydrostatic inversion of high resolution ice shelf surface elevation data are used to validate the model outputs. This is followed by a suggested workflow that can be adopted by modelers to use inverse methods to validate subglacial hydrology model outputs.

The model outputs from this study suggest an active subglacial hydrological network beneath Slessor Glacier and the surrounding area. There is good agreement between areas of fast ice flow and areas where the model predicts deep water, low effective pressure and an efficient drainage network. These results are consistent with areas of inferred low basal friction coefficient from the ice dynamics model, which also recovers observed velocities from a stress balance simulation.

The results of this thesis demonstrate some control of basal hydrology on ice dynamics in the Slessor Glacier study area. Furthermore, the methods used here provide subglacial hydrology modelers an additional means of model validation, which is valuable where observed data is sparse or not available.

Acknowledgements

Dedication

This thesis and all the work that went into it is dedicated to Dr. Pierre-Michel Rouleau. You taught me what it means to "think like a physicist".

Merci pour tout.

Table of Contents

List of Figures

xiv

List of Tables

Chapter 1

Introduction

Glaciology is a field that is becoming increasingly crucial in light of global climate change. Melting ice sheets and glaciers cause global sea level rise, alter the path in which waterways flow, and have major implications for tourism, hazard warning, and clean water supply for many northern/indigenous communities (Hovelsrud et al., 2011; Edwards et al., 2021). This leads to the need to be able to predict the future behaviour of glaciers and ice sheets.

Advancements in technology and field work methods have led to the generation of data (e.g., Morlighem et al., 2020; Prior-Jones et al., 2021) that have improved our understanding of glaciers and ice sheets. However, there are still many crucial aspects of glaciers that in many areas cannot be measured or tested due to ice thickness being on the order of kilometres. It is important to understand the drivers of glacier flow as they govern the speed at which ice flows into the ocean, and thus how fast the global sea level will rise. The subglacial hydrological system is a known driver of ice dynamics and a crucial component of the glaciological system (Iken and Bindschadler, 1986; Fountain and Walder, 1998; Clarke, 2005). Ice rigidity and basal drag are two parameters directly related to ice deformation and basal velocity respectively, yet, like the subglacial hydrological system, they are difficult to measure and so remain poorly constrained despite being the two main physical components that parameterize glacial dynamics (Cuffey and Paterson, 2010).

Mathematical models are tools that can be used to characterize unknown parameters and project the behaviour of ice masses into the future. To create an effective model, one needs a sound physical basis, a mathematical framework and high quality data sets of quantities that can be measured. This has been done in glaciology, and there exists many models and methods to extract details about subglacial hydrological networks (e.g., Flowers, 2015) and to constrain physical parameters (e.g., MacAyeal, 1992; Morlighem et al., 2013; Brinkerhoff et al., 2021). Since it is not possible to know the exact nature of basal processes and parameters beneath glaciers and ice sheets without direct measurement, mathematical modelling is the only method currently available to estimate these important quantities. It is therefore of the utmost importance to model carefully and accurately as the timeline of global climate change, and what it will do to the Earth's cryosphere, still remains unknown.

1.1 Subglacial Hydrology

For a typical mountain glacier, hydrology is broken down into three components, supraglacial (surface), englacial (middle), and subglacial (basal) hydrology. In Antarctica, there is no supraglacial nor englacial hydrological systems (see section 1.1.6 for more on this), and so this study focuses on the subglacial hydrological system only.

1.1.1 The Subglacial Hydrological System

Water at the base of a glacier is considered to form the subglacial hydrological system. Many glaciers have water at their base (though there are cold-based glaciers that are frozen to their base) and several processes/properties are responsible for generating this meltwater: (1) heat from the Earth, or geothermal heat, that warms the base of ice; (2) heat production from friction as the ice slides over hard sediment/bedrock heat; (3) the pressure-dependence of the melting/freezing point of ice, by which water at the base of the glacier/ice sheet is under pressure from the overlying ice, and water can persist at temperatures below 0°C when under sufficiently high pressure; and (4) water at the base of a glacier is insulated from cold atmospheric temperatures from the overlying ice.

The persistence of liquid water at the base of a glacier/ice sheet has many implications for glacier movement and ice dynamics. It follows that an important consideration for understanding the impact of subglacial hydrology on ice dynamics is the complex system of subglacial channels (or conduits) and cavities that forms beneath the glacier.

1.1.2 Channels and Cavities

The following section will provide an introduction to subglacial channels and cavities, including how they open and close, the R-channel theory, and a review of cavitation.

A channel beneath a glacier that is completely void of water will close due to a process called ice creep - the inward closure of ice due to the weight per unit area of the overlying ice, i.e., ice overburden pressure:

$$p_i = \rho_i g H, \tag{1.1}$$

where p_i is the ice overburden pressure, ρ_i is the density of ice, g is the acceleration due to gravity, and H is the thickness of the ice. Ice-creep will not close a water-filled channel if the water pressure, p_w, is equal to or greater than the ice overburden pressure (Fountain and Walder, 1998). As water flows through these channels, there is melting of the channel walls due to heat from friction, and if this heat energy is sufficiently high, channels can persist and grow at pressures $p_w \leq p_i$ (Röthlisberger, 1972; Fountain and Walder, 1998).

A common theory used for treating channel formation beneath glaciers was described by Röthlisberger (1972). In his paper, Röthlisberger (1972) derives a governing differential equation for water pressure when the melting of ice in a channel wall (expansion) and closure from ice creep (shrinkage) are in balance for a given discharge. The result was a

simplified model simulating a channel with a circular cross-section completely embedded in ice (englacial channel), and a semicircular shape if at the base of the glacier (subglacial). These channels are commonly referred to as Röthlisberger-, or R-channels.

The R-channel theory is not the only treatment of subglacial channels, and it is not without its limitations and criticisms (e.g., Walder, 2010). It has previously been suggested that broad, low channels may capture basal water measurements more accurately (Hooke et al., 1990), however, the R-channel theory provides a tractable mathematical formulation for channel development, and has served as the basis for many hydrology models in glaciology (e.g., see table 3 in Flowers, 2015).

In contrast, subglacial cavities form from the separation of sliding ice and the glacier bed, and the faster the ice and rougher the bed, the more likely cavities are to form (Fountain and Walder, 1998). Lliboutry (1976) described two regimes that cavities fall under: (1) an autonomous regime, in which meltwater within the cavities stagnates and has no effect on the subglacial system, and (2) a connected hydraulic regime where cavities are linked to R-channels. The second regime is more relevant to dynamical changes in the subglacial system, and widespread cavitation as it is in the second regime will be referred to as a "linked-cavity system", which is nonarborescent in shape, and contains a large volume of water with very little flux (figure 1.1).
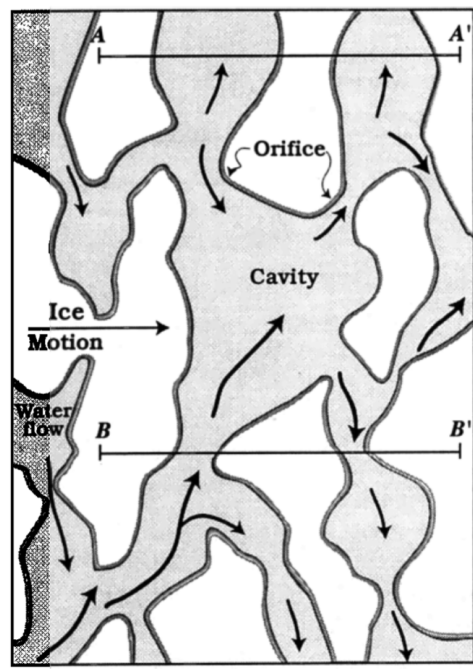
Figure 1.1: An idealized subglacial cavity network. From Fountain and Walder (1998).

There have been investigations into other states of the linked-cavity system as well. A useful quantity in glaciology that couples subglacial hydrology to the ice above it is *effective pressure*:

$$N \equiv p_i - p_w, \tag{1.2}$$

3

where N is the effective pressure and p_w is the pressure of the subglacial water. Water flow beneath a glacier is driven by gradients in hydraulic potential, which is stated as

$$\phi = \phi_m + p_w, \tag{1.3}$$

where $\phi_m = \rho_w g B$ is the elevation potential, ρ_w is the density of water, and B is the bed elevation. Creyts and Schoof (2009) found that by varying combinations of the gradient of hydraulic potential ($\nabla \phi$) and effective pressure, the distributed system can exist at multiple different steady states. This differs from what was suggested by the classic theories suggested by Röthlisberger (1972) and Shreve (1972) as they theorized that water flux may only increase monotonically as a function of $\nabla \phi$ and N.

1.1.3   Subglacial Water Pressure and Surface Velocity

A pressurized basal water system will have an influence on the entire glacier/ice sheet. Indeed, after running a finite element scheme in an idealized numerical model, Iken (1981) found that subglacial water pressure, p_w, has an effect on the glacier sole which can be broken down into two phases. The first phase is a transient phase, which consists of two sub-phases: the first describes how the action of p_w re-distributes the pressure of the overlying ice, and the second states that there are stages of water-filled cavity growth and shrinkage. The second phase describes steady state sliding of ice over cavities at a fixed p_w. Iken (1981) went on to characterize an important relationship between the sliding velocity of a glacier and subglacial water pressure; sliding velocity is a *function* of both subglacial water pressure, and cavity size.

However, in an analysis of p_w and surface velocity at Findelengletscher, Switzerland, Iken and Bindschadler (1986) discovered that p_w does not affect the sliding velocity of a glacier if it is just localized to a small number of channels. It is when p_w is widespread over large portions of the glacier bed that the relationship between sliding velocity and subglacial water pressure comes into effect.
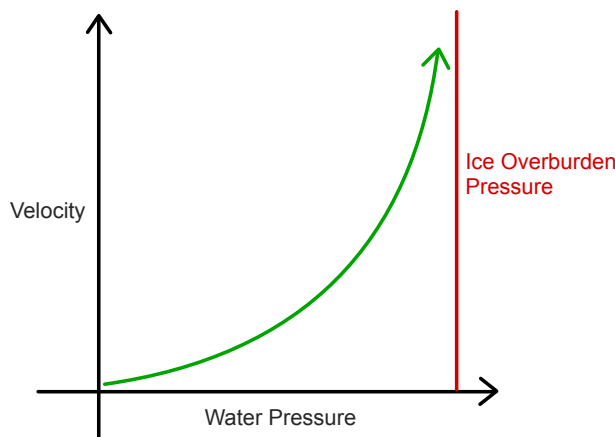
Figure 1.2: Idealized visualization of velocity as a function of subglacial water pressure. Adapted from Iken and Bindschadler (1986).

In the experiment carried out by Iken and Bindschadler (1986), the depth of water below the glacier surface was used to measure p_w, i.e., as the water becomes more pressurized, it will push itself up further into boreholes. At the same time, they used a pole to measure the horizontal velocity of the glacier. In figure 1.2, an idealized version of these data are plotted and two important things can be seen:

1. a functional relationship between sliding velocity and p_w, and

2. a vertical asymptote at the ice overburden pressure.

As p_w approaches the same value as that from the overlying ice, the horizontal velocity of the glacier increases very quickly. It is concluded that short-term velocity variations are related to the sliding velocity of the base of the glacier, and the mechanism behind this is that the growth of water filled cavities is dependent on p_w, i.e., subglacial cavity growth is a function of p_w (Iken and Bindschadler, 1986). This established relationship between basal velocity of ice and subglacial water pressure can be thought of as a hierarchy, and Le Brocq et al. (2013) provide evidence that this relationship also applies to the ice sheets as well as alpine glaciers.
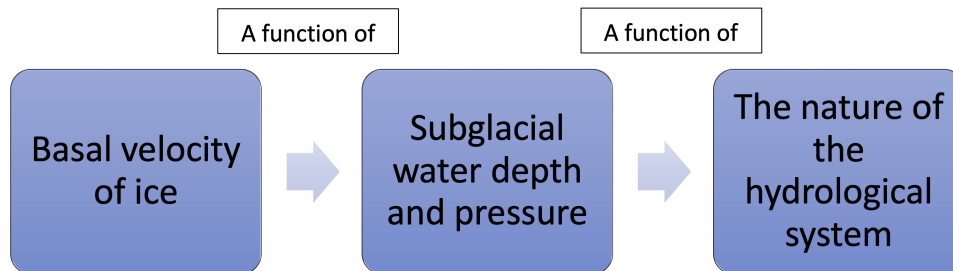
Figure 1.3: Visualization of functional relationship between basal velocity of ice, subglacial water depth and pressure, and the nature of the hydrological system.

1.1.4 Channelized and Distributed Subglacial Drainage Networks

Subglacial drainage networks are typically divided into two types (Fountain and Walder, 1998):

1. Channelized/fast/efficient, and

2. Distributed/slow/inefficient.

Both of these systems host unique properties that distinguish one from the other (table 1.1 and figure 1.4).

Table 1.1: Characteristics of the channelized and distributed subglacial drainage systems.

Channelized/Fast	Distributed/Slow
Relatively large basal melt	Limited basal melt
Large supply of meltwater	Limited supply of meltwater
Efficiently removes water from system	Inefficiently removes water from system
Lower pressure	Higher pressure
Total discharge sensitive to changes in system volume	Total discharge relatively insensitive to changes in system volume
Low surface-to-volume ratio	Relatively high surface-to-volume ratio
Arborescent in shape (tree-like)	Non-arborescent with many complicated flow paths
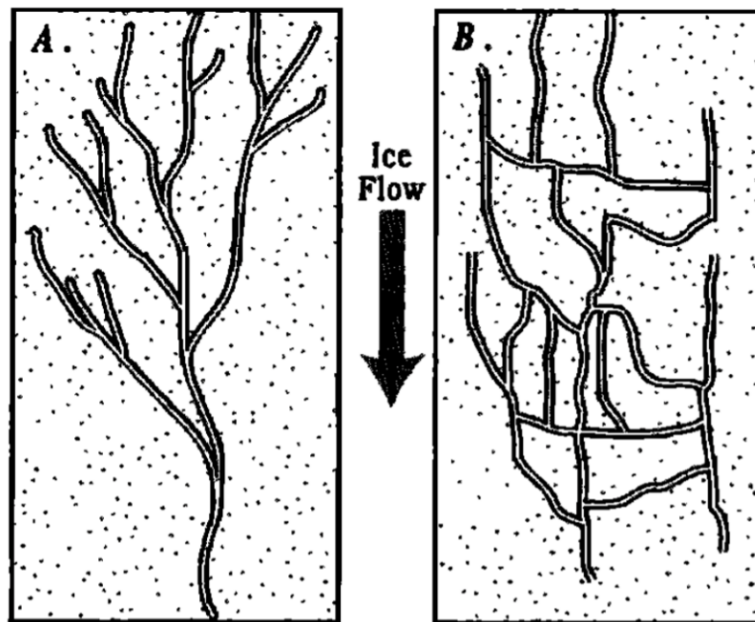
Figure 1.4: (a) Cross sectional view of a channelized drainage network.(b) Cross sectional view of a distributed drainage network. From Fountain and Walder (1998).

Glaciers and ice sheets are also not restricted to just hosting one network or the other, it is entirely possible that part of the bed may host a channelized network whereas another part may host a distributed system as large-scale changes to a subglacial network are not instantaneous. Moreover, any region can switch between one system or the other in response to perturbations in melt input (Fountain and Walder, 1998).

A natural question that might arise is what triggers the switch between the drainage modes? For most glaciers, the answer to that question is typically meltwater input from the supraglacial system. For alpine glaciers, in the fall and winter months there is little to no input from the surface. In this situation, the subglacial system hosts a distributed drainage network. This system is highly pressurized due to the small flux; this is a system inefficient at removing water. Other important characteristics of the distributed system include water moving through the underlying sediment, for which the meltwater flux, Q_{Darcy}, can be calculated via

$$Q_{\text{Darcy}} = \left(\frac{\kappa BW}{\rho_w g} \right) \left(\frac{d\phi}{ds} \right), \tag{1.4}$$

where κ and B are the hydraulic conductivity and thickness of the sediment/till layer respectively, W is the glacier bed width, $d\phi/ds$ is the hydraulic gradient, and s is a coordinate which increases upglacier. As well, a thin water film can exist which affects water chemistry and sliding speed, but allows very little flux (Fountain and Walder, 1998).

During the spring and summer months at a temperate mountain glacier, meltwater input is increased, and suddenly the highly pressurized distributed system is met with a large flux of water. As water is forced into this linked-cavity system, frictional heat production from the flow of water will increase, and ice will begin to melt. This melt will continue until a threshold is passed, and at that point, unstable channel growth begins where the melt rate is significantly larger than the rate of closure due to ice creep. As the cavity gets larger, water will begin to flow here preferentially, and will be poached from nearby cavities. At this point, as the water keeps flowing through the cavity, it eventually becomes an R-channel. Once summer is over and fall begins, the meltwater input to the system will decrease until the closure rate of the channels due to ice-creep surpass the melt rate, and the distributed network will reform.

If this system is to be modelled in a way that reflects reality, the switch between the channelized and distributed drainage modes is needed. For example, Schoof (2010) captured the change by introducing a critical discharge, for which once the discharge falls below, the system will behave as a distributed drainage system, and while above, an efficient drainage system. Currently, models simulate subglacial hydrology by allowing the distributed system to naturally evolve into an efficient drainage system over time (e.g., Werder et al., 2013; Sommers et al., 2018). For Antarctic glaciers the nature of the subglacial system is quite different as there is no surface water input, and the subgalcial hydrological system beneath Antarctica will be covered in-depth in section 1.1.6.

1.1.5   Overdeepenings and Subglacial Lakes

Overdeepenings refer to subglacial basins that are a consequence of glacier erosion, and they have been found beneath mountain and outlet glaciers, as well as beneath ice masses on the Greenland Ice Sheet (GrIS) and the Antarctic Ice Sheet (AIS) (Cook and Swift, 2012). Overdeepenings found beneath large outlet glaciers in Antarctica have been shown to be linked to unstable retreat over adverse slopes, and through modeling studies, the presence

of an overdeepening has been linked to the hysteresis mechanism unique to marine ice sheets (Schoof, 2007; Garbe et al., 2020).

Modeling work suggests that subglacial hydrology plays a role in the formation of overdeepenings near glaicer outlets (e.g., Herman et al., 2011), and Alley et al. (2003) suggest that the depth of an overdeepening is stabilized by subglacial hydrology. Overdeepenings certainly play a role in the subglacial drainage network as water is predicted to flow into these areas, pool, and increase water pressure resulting in a localized inactive hydrological system within the overdeepening, whereas glacier margins may be active (Dow et al., 2014).

It was hypothesized that if the bed of a glacier (the adverse slope) is at a sufficiently steep angle, viscous dissipation (internal friction of water) produces too little heat for the pressure-melting point to keep subglacial channel opening rates above zero, and hence the channelized system is shut down completely by ice-creep (Alley et al., 2003). This angle is referred to as the *supercooling threshold*, and when it is reached, the drainage system switches to distributed. This supercooling threshold was met by satisfying the following inequality

$$-Q\phi' + \gamma Q p'_w \leq 0, \tag{1.5}$$

where Q is channel discharge, ϕ' and p'_w are the gradients of hydraulic potential and water pressure respectively, and γ is a dimensionless constant that is the product of specific heat capacity, the density of water, and the Clausius-Clapeyron coefficient. Noting that $\phi = p_w + \rho_w g B$, equation (1.5) can be rewritten as

$$\frac{\rho_w g B'}{p'_w} \leq \gamma - 1. \tag{1.6}$$

However, in the study by Alley et al. (2003) it was assumed that water pressure was at overburden, yet observations do not support this assumption as water pressures downstream of overdeepenings are often less than overburden pressure. This led Werder (2016) to develop a new supercooling threshold.

At any point within an R-channel, the water pressure is dependent on the conditions downglacier, which means that pressures will usually be less than overburden by a factor f, the flotation fraction. In equation (1.6), if the adverse bed slope of the overdeepening is high, then to remain at the threshold the pressure gradient must also be high. This means that the steeper the adverse slope, the larger the water pressure must be in the basin of the overdeepening to ensure that the supercooling threshold is met, and so when the water pressure upstream of the adverse slope is at overburden, this is when the highest pressure gradient will occur.

To account for this pressure gradient, a new supercooling threshold formula is presented by Werder (2016):

$$\frac{\Delta B}{\Delta S + h_1(1-f)} \leq \kappa \approx -1.6, \tag{1.7}$$

where h_1 and f are the ice thickness and flotation fraction at the downstream end of the overdeepening respectively.
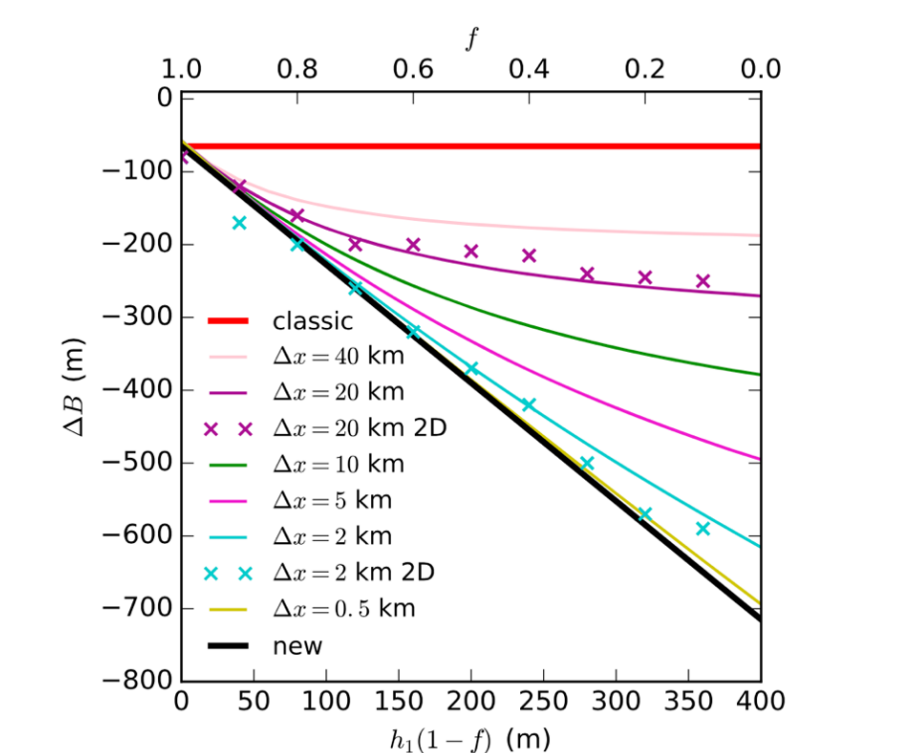
Figure 1.5: Flotation fraction f (top) and correction factor $h_1(1-f)$ (bottom) versus overdeepening depth ΔB at supercooling threshold for $h_1 = 400m$ and $\Delta S = 40m$. Solid red line represents the classical result, and the solid black line represents equation (1.7). Δx represents the different adverse bed slope lengths for various model runs. From Werder (2016).

It is concluded that the classical result (solid red line in figure 1.5) gives the depth where supercooling can occur, but not where it *must* occur, the latter is represented by the curves for various adverse bed slope lengths, Δx (Werder, 2016).

Overdeepenings can also give rise to another phenomenon found beneath the AIS. At the base of the AIS, geothermal heat is sufficiently high (approximately 70 mWm^{-2} in West Antarctica, and 50 mWm^{-2} in East Antarctica) to melt the overlaying ice and produce water at the base of the ice sheet (Wright and Siegert, 2012). This water then flows according to the Earth's gravitational influence and ice overburden pressure where it eventually collects in local hydrological sinks. These sinks are typically bedrock troughs (overdeepenings), and these collections of liquid water beneath the ice sheet are referred to as *subglacial lakes* (figure 1.6).
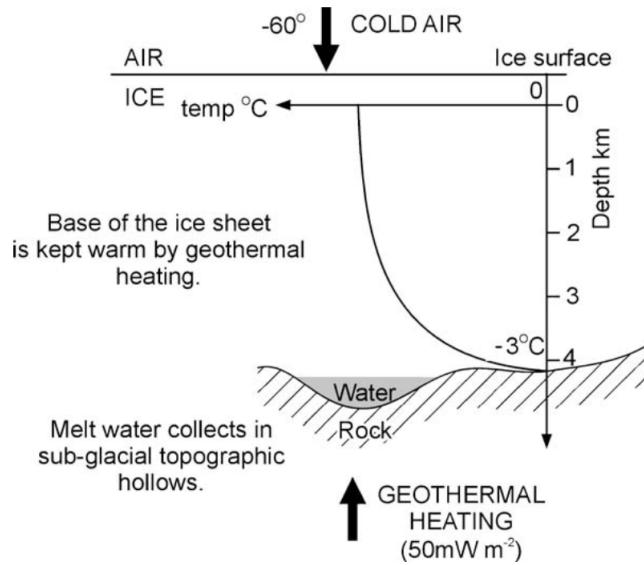
Figure 1.6: Conceptual diagram of subglacial lake formation. From Siegert (2005)

The most recent inventory of subglacial lakes beneath the AIS accounts for 675 lakes (Livingstone et al., 2022) (figure 1.7), and Wright and Siegert (2012) give three reasons why subglacial lakes are of significant interest:

1. subglacial lakes provide unique habitats for microbial life to persist,

2. subglacial lakes are locations where it may be possible to collect sedimentary records of past climate history, and

3. subglacial lakes are an important component of the subglacial hydrological system as they are known to fill and drain over time.

Subglacial lakes can be classified into three different types, (1) lakes found in overdeepenings in the interior of the ice sheet, (2) lakes found on the side of subglacial mountains, and (3) lakes beneath areas near the onset of fast ice flow (Siegert, 2005).
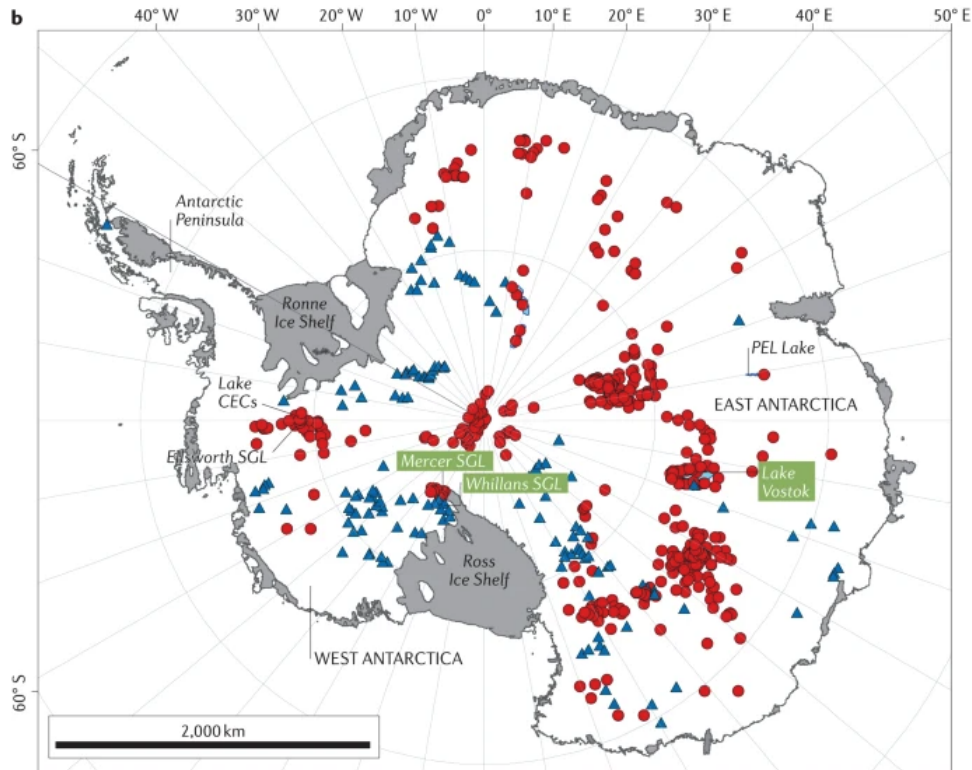
Figure 1.7: Subglacial lake inventory beneath Antarctica. Red circles are stable lakes (i.e., those that are either closed systems or have balanced inflow and outflow) and blue triangles represent active lakes that periodically fill and drain. Image from Livingstone et al. (2022).

1.1.6 Subglacial Hydrology Beneath the Antarctic Ice Sheet and Floating Ice Shelves

The subglacial hydrological network beneath the AIS is not seasonally driven, meaning the nature of the network is fundamentally different than those found beneath mountain glaciers and the GrIS. The reason the subglacial network beneath the AIS is not seasonally driven is that air temperatures remain too cold year-round to allow for surface melt. This does not mean that an active subglacial hydrological system does not exist, and in fact, an active system of subglacial lakes and geomorphological evidence suggest the opposite. Ashmore and Bingham (2014) show that a landscape in Victoria Land, East Antarctica, contains evidence for the former existence of an extensive subglacial network (figure 1.8).

Figure 1.8: Photo evidence of a subglacially formed channel system incised into the bed in western Wright Valley, Dry Valley region, East Antarctica. From Ashmore and Bingham (2014).

The geomorphological evidence presented by Ashmore and Bingham (2014) consists of a deglaciated landscape containing channels up to 30 km in length, potholes and plunge pools, and areas of stripped bedrock. All of these features are indicative of the existence of a subglacial network beneath the AIS. Water beneath the AIS is produced from geothermal and frictional heat (ice sliding over hard sediment/bedrock) only, and this water persists beneath the thick Antarctic ice for the same reasons it exists beneath other ice masses (see points (3) and (4) in paragraph 1 of section 1.1.1).

Moreover, ice surface altimetry data show that subglacial lakes both fill and drain over time (to the order of years for active subglacial lakes), and interact with downstream lakes and the subglacial hydrological system by routing water towards the grounding line (Dow et al., 2016).

Dow et al. (2016) used a subglacial hydrology model over a synthetic ice stream (an area within an ice sheet where ice flows faster than at its margins) to analyze the drain/fill cycle of subglacial lakes. An ice stream is a good selection for a synthetic model run as they can often contain many subglacial lakes (e.g., Recovery Glacier contains up to 13 subglacial lakes (Fricker et al., 2014)). Two basal topographies were chosen for the domain of the project, one of which hosted an overdeepening.

The results of the study gave rise to a mechanism of pressure waves that encourage both growth and drainage of subglacial lakes within their synthetic ice stream by steepening the hydraulic gradient, and moreover, as these pressure waves propagate downstream (at a rate of approximately 220 meters per day), both flux and channel growth are enhanced. Once these waves subside, pressure and water flux fall and channels shut down. The original study over the synthetic domain was expanded upon by a second modeling project by Dow et al. (2018a), where this time, instead of a synthetic ice stream, real topography data from Recovery Glacier was used to investigate subglacial lake activity in this area. Their

model also simulated the pressure wave phenomenon beneath the Recovery Glacier study area, and the following characterization of the pressure waves are given:

- the pressure waves are caused by large quantities of subglacial water constricting the neck of the ice stream by entering a drainage catchment,

- as these pressure waves propagate, subglacial hydraulic potential continually changes, contributing to both subglacial lake drainage and growth,

- water is driven downstream as potential gradients steepen from increasing pressures within the basin,

- this driven water permits channel growth at the lip of the overdeepening, and

- these channels expand to the point where they can drain the lake and move the water downstream to the next subglacial lake.

Once this process completes, it starts over in what Dow et al. (2018a) refer to as a cascading pattern. Furthermore, they were able to use their model to predict subglacial lake locations that were generally in good agreement with those found with ice altimetry data (figure 1.9).
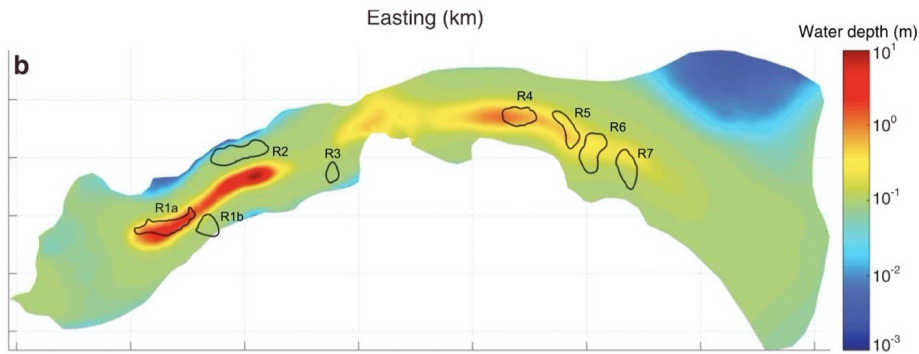
Figure 1.9: Comparison of predicted lake locations between a model run (areas of high water depth) and altimetry data (black polygons). From Dow et al. (2018a).

There is a disagreement between the locations found from altimetry and the model outputs for subglacial lakes R1b and R2 in figure 1.9, and the model predicts a lake at a location between R3 and R4 that the altimetry data did not pick up. The authors did mention, however, that this is possibly a consequence of data being too sparse to accurately invert for the RIS topography.

Willis et al. (2016) modeled subglacial water flux beneath the entire AIS by calculating subglacial hydraulic potential via the Shreve equation (Shreve, 1972),

$$\phi = \rho_i g z_s + (\rho_w - \rho_i) g z_b, \tag{1.8}$$

where z_s and z_b are the ice surface and bed elevations, respectively, and in this context, subglacial water pressure is assumed to be at overburden everywhere. The results from their modeling project by suggest that the AIS can annually drain approximately 31% (21.4km^2) of the ice sheet's total mass balance, and a map of water flux in the ice sheet's main drainage pathways can be seen in figure 1.10.
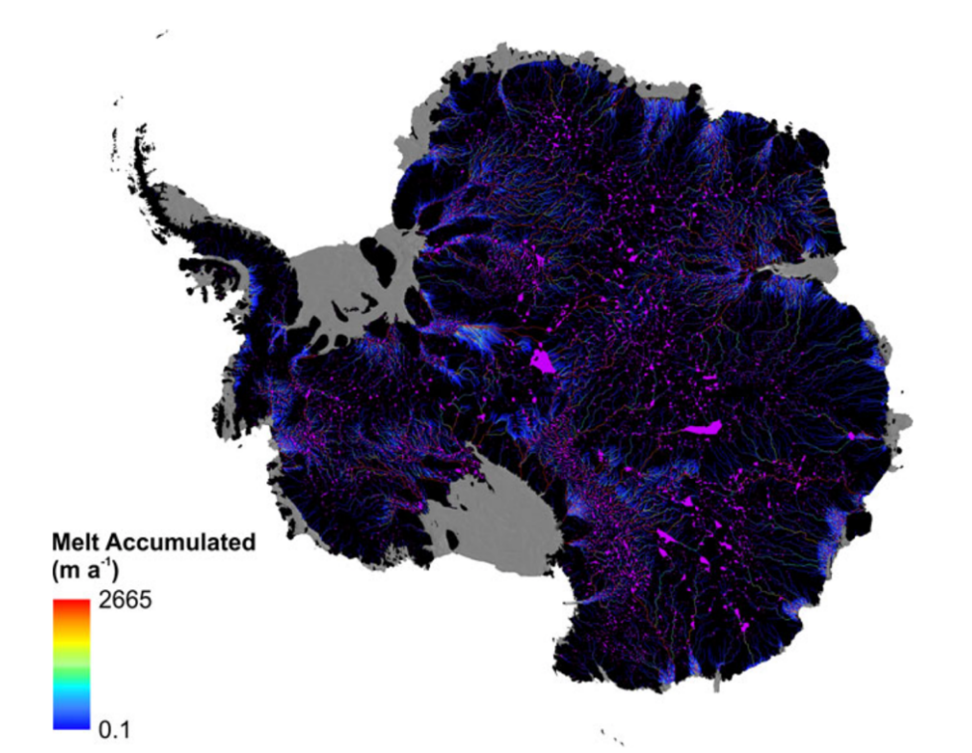
Figure 1.10: Pathways with accumulated melt flux greater than 0.1 ma^{-1}. Magenta represents filled sinks/potential subglacial lake locations. From Willis et al. (2016).

Over 80% of grounded ice in Antarctica drains into floating ice shelves, and the subglacial system beneath grounded ice often drains fresh water into floating ice shelves (e.g., in East Antarctica, Slessor Glacier, Bailey Ice Stream and Recovery Glacier all drain into the floating Filchner Ice shelf) (Le Brocq et al., 2013). Floating ice shelves in Antarctica are typically maintained by mass gain due to snow accumulation and mass loss when icebergs calve off their fronts Adusumilli et al. (2020). An important aspect of ice shelves in Antarctica is that they provide buttressing, or, back stress from friction on the valley walls and basal pinning points (localized high points of basal topography where floating ice shelves reattach to the bed), which stabilizes the speed of grounded ice flowing into ice shelves (Thomas et al., 1979). However, many ice shelves in Antarctica are not being maintained and experiencing thinning and net mass loss (Pritchard et al., 2012; Paolo et al., 2015), which reduces the buttressing effect and enhances flow of grounded ice. Sun et al. (2020) demonstrated that the loss of ice shelf buttressing could lead to total collapse of ice shelves through the marine ice sheet instability hypothesis (MISI)[1] at areas with

---

[1]The MISI states that glaciers on a retrograde slope could experience fast and irreversible grounding

retrograde slopes, which has the potential to raise sea-level by $1.91 - 5.08$ m.

Ice shelves host their own collection of topographic features such as fractures and basal channels (Le Brocq et al., 2013; Indrigo et al., 2021). Le Brocq et al. (2013) used airborne remote sensing techniques to highlight that several areas on floating ice shelves in Antarctica host basal channels that form as a consequence of channel discharge at glacier and ice stream outlets. When channel discharge exits the grounding line of grounded glaciers connected to floating ice shelves, the discharge is fresh relative to the ocean water beneath the ice shelf. Due to the difference in salinity, the glacier discharge rises to the base of the ice shelf entraining comparatively warm ocean water with it. This process can incise a small ice shelf channel which rapidly enlarges due to high localized melt rates, focusing meltwater plumes into these ice shelf basal channels. These channels continue across the base of the floating ice shelf, typically aligned with the direction of flow, until eventually the pressure is sufficiently low to supercool the channel, and it freezes shut. This process is shown graphically in figure 1.11.
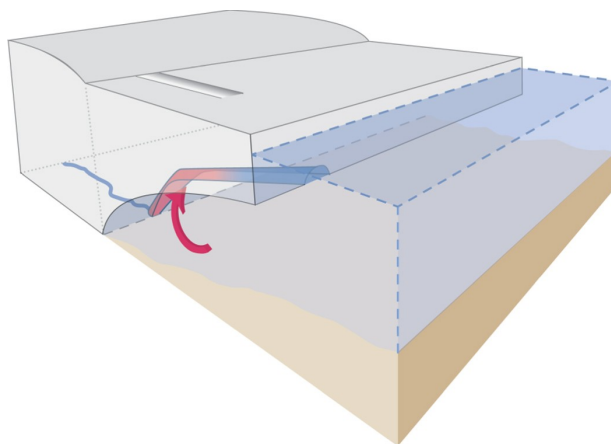
Figure 1.11: Pictorial representation (not to scale) of ice shelf basal channel formation. The red arrow represents the relatively warm ocean water being entrained by the channel discharge. Image from Le Brocq et al. (2013)

1.2 Subglacial Hydrology Models and their Limitations

1.2.1 The Basics of a Subglacial Hydrology Model

Following the modeling groundwork of Shreve (1972), Röthlisberger (1972), Iken (1981), Fountain and Walder (1998), and others, many subglacial hydrology models have been developed over roughly 60 years.

For this section, the development of a subglacial hydrology model will follow that laid out by Flowers (2015). Conservation of water mass for a distributed water sheet demands

line retreat if their fringing ice shelves are removed (Diez et al., 2018; Bamber et al., 2009)

15

that

$$\frac{\partial h}{\partial t} + \nabla \cdot \mathbf{q} = b, \tag{1.9}$$

where h is the water volume or depth of the water sheet, q is the water flux per unit area and b is a source and sink term. Equation 1.9 is sometimes referred to as the *continuity equation*, and some examples of sources and sinks are supraglacial runoff, englacial water production, recharge or discharge from adjacent aquifers, or basal water production. A common method for computing the sheet discharge flux is to use the empirical expression

$$\mathbf{q} = -Kh^\alpha \left(\nabla\phi\right)^\beta, \tag{1.10}$$

as opposed to deriving an expression for fluid velocity which is integrated over some depth h to compute the sheet flux. In equation 1.10, K is a rate factor, $\nabla\phi$ is the gradient of hydraulic potential and exponents α and β correspond to either laminar flow ($\alpha = \beta = 1$) or turbulent flow ($\alpha = 5/4, \beta = 1/2$) from Darcy's law.

To apply this model to a channelized/efficient drainage system, the flux $\mathbf{q}$ would become a channel discharge, Q, and a channel cross-sectional area (CSA), S, would replace the water sheet depth h. Moreover, for a model to include an evolution between a distributed sheet model and a channelized model, a relation of the form

$$\frac{\partial h}{\partial t} = \mathcal{O} - \mathcal{C}, \tag{1.11}$$

would have to be imposed, where $\mathcal{O}$ determines the rate of cavity opening and $\mathcal{C}$ determines the rate of cavity closing, and a relation based on the chosen theoretical framework will have to be introduced to relate the contribution from the sheet system to the channel system.

To move a fluid from one state to another, where states differ by pressure and elevation, mechanical energy is required. This mechanical energy is referred to as hydraulic potential, ϕ, and in the subglacial hydrology system, the pressure and elevation correspond to water pressure, p_w, and bed elevation, B, respectively (equation 1.2). It is common for subglacial hydrology models to form their governing equations as partial differential equations (PDEs) of ϕ (e.g., Werder et al., 2013).

1.2.2 Limitations of Subglacial Hydrology Models

Subglacial hydrology modeling in glaciology started in the 1970s with early groundwater models and has since progressed to sophisticated multi-element models that can capture the evolution and interaction of multiple drainage components (Flowers, 2015). An illustration of how far modelling has come, along with its sophistication and spatial dimensionality can be seen in figure 1.12.
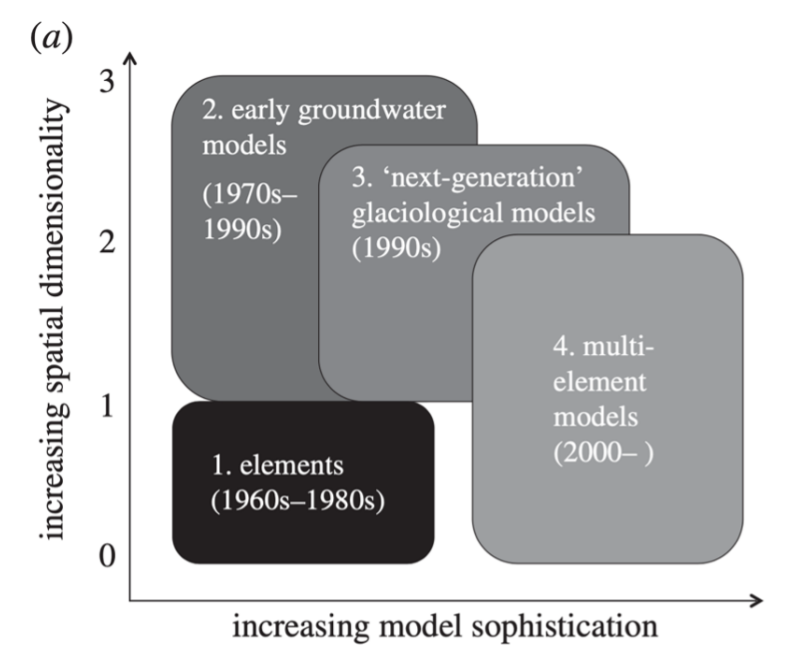
Figure 1.12: Illustration of spatial dimensionality and model sophistication from the early 1970s to present day. From Flowers (2015).

Flowers (2015) highlights some of the obstacles that models have already overcome, for instance, models have successfully

- applied necessary physics to model both distributed and channelized drainage systems,

- created an elegant numerical framework to mathematically solve the equations governing the physics,

- simulated the spontaneous development of complicated channel networks from both point- and distributed sources of water, and

- coupled ice dynamics to glacier hydrology (albeit with several assumptions due to computational restrictions).

Many issues with subglacial hydrology remain yet to be addressed completely. One issue is that assumptions have to be made (e.g., the most simple models assuming water pressure at overburden everywhere) in order to come up with mathematical frameworks that can be computed in a reasonable amount of time, or at all. In situations where surface melt is a key factor, the R-channel formation framework along with the linked-cavity system is used almost exclusively to represent the channelized and distributed drainage modes, without exploring the possibility of other, perhaps more realistic approaches (e.g., Hooke et al., 1990). In addition, it is important to constrain and validate models with observational data, yet, model development in glaciology has moved at a pace much faster than data acquisition (Dow et al., 2018a, 2020). Moreover, while progress has been made

for models that couple distributed and channelized drainage systems (by starting with the distributed system and letting the channelized network form naturally), parameters such as basal sliding rate, water input rate, and basal distributed system conductivity are still left unknown/poorly understood, due to the inherent difficulty in measuring these quantities directly (Dow et al., 2020).

The subglacial hydrological system in Antarctica is more poorly constrained and less extensively studied than glaciers in any other area of the world (Ashmore and Bingham, 2014). Since there is little to no precipitation or surface melt in Antarctica, the basal melting rate is extremely important for applying an accurate model to the region. As well, geothermal heat is a key process in determining ice temperature and basal melt rates, yet, it is not clear which estimate is most appropriate to represent reality despite substantial differences between several estimates due to the lack of necessary data (Burton-Johnson et al., 2020) (figure 1.13).
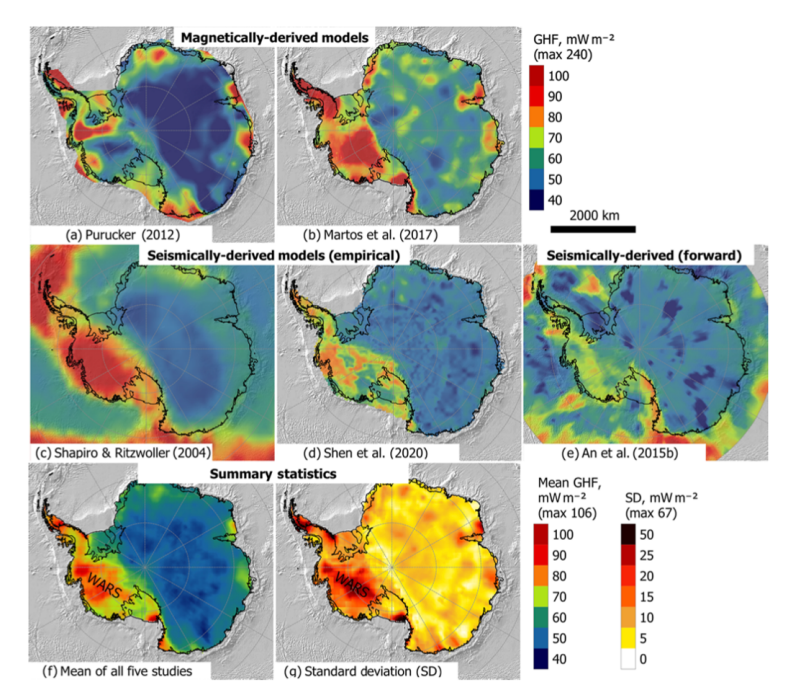
Figure 1.13: Various estimates of geothermal heat flux beneath the AIS. From Burton-Johnson et al. (2020).

1.3 Inverse Modeling for Ice Dynamics

Subglacial hydrology models like those described in section 1.2 are *forward models* that make approximations of relevant physics, and like any model that utilizes approximations, cannot represent reality exactly. Forward models use parameters, that are often constrained by reality, and they are mathematically well-posed.

Inverse models are *backwards models* which are used to estimate unknown or poorly

constrained parameters from data. Unlike forward models, inverse models are ill-posed meaning (1) there might not be any solution to the problem, (2) there may be infinite solutions to the problem, and (3) even when a solution is found, it may be sensitive to initial conditions (i.e., not robust). Generally, inverse methods are iterative processes which start from some initial guess of a control parameter (e.g., basal friction), and with each iteration progressively improve that guess getting closer to the true value based on its relationship to the measured data.

Forward and backwards models are both important elements in characterizing the nature and future behaviour of glaciers and ice sheets. Furthermore, using both hydrology and inversion models in tandem can generate a more holistic set of outputs.

1.3.1 Inverting for Ice Rigidity and the Basal Friction Coefficient

In the simplest terms, glacier motion is a result of downward forces that are opposed by resisting forces. In Antarctica, however, resisting forces are difficult to measure directly because of kilometer thick ice, and so parameters important to resisting forces remain poorly constrained. Two parameters that play a major role in resisting glacier motion are ice viscosity and basal drag, which characterize how well ice resists internal deformation and the slipperiness of the base over which a glacier or ice stream slides, respectively. Ice viscosity is governed by Glen's flow law (Glen and Perutz, 1955) (equation 2.35 in section 2.2), and basal drag is governed by friction laws, for which there are several different options (e.g., Weertman, 1957; Budd et al., 1979; Schoof, 2005). The lack of data regarding ice viscosity and basal drag has motivated researchers to find alternative methods to approximate these quantities, and one such method is performing an inversion simulation (MacAyeal, 1992; Morlighem et al., 2013; Arthern et al., 2015). The two parameters that the inversion simulations compute are ice rigidity (sometimes called ice hardness or stiffness) and the basal friction coefficient (sometimes called basal drag coefficient).

Inverse methods were first used in glaciology by MacAyeal (1992) and, since then, they have become much more sophisticated and are calculated in several different ways (e.g. adjoint methods, least-squares inversion, Bayesian methods, inverse Robin problems, etc. (Barnes et al., 2021)). An example of this is can be found in the modeling study by Morlighem et al. (2013), where the basal friction coefficient over the entire Antarctic continent was calculated (figure 1.14) using an inversion of exact and incomplete adjoints.
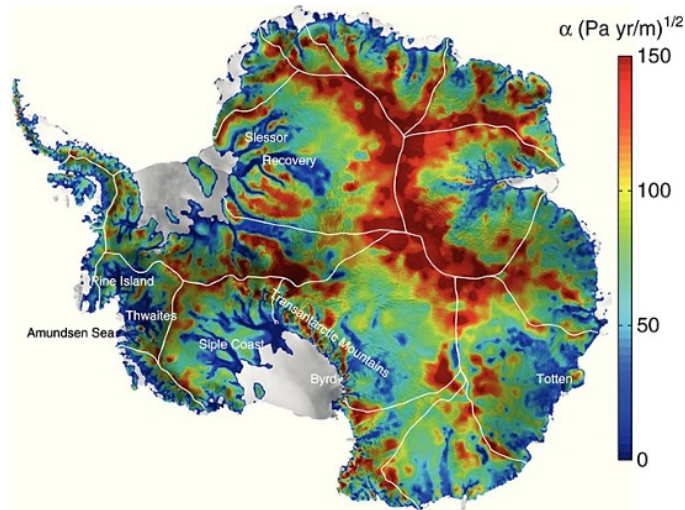
Figure 1.14: Basal friction calculated from exact and incomplete adjoint inversion method. From Morlighem et al. (2013).

In another study, Arthern et al. (2015) invert for the ice rigidity coefficient, which they used to calculate Antarctic-wide ice viscosity. (figure 1.15).
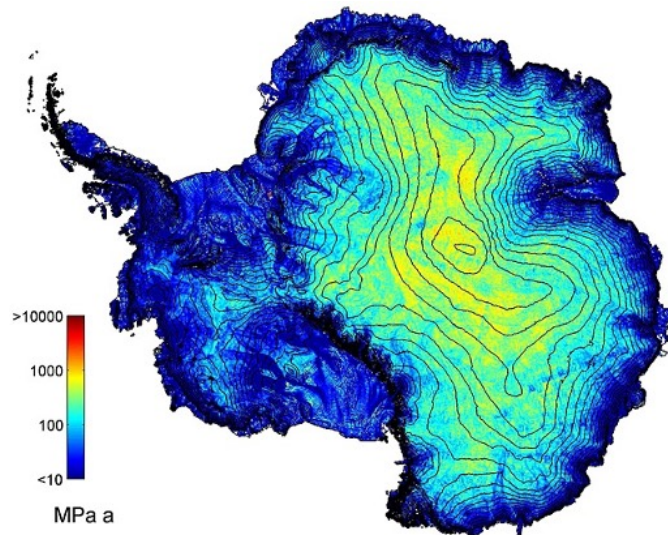
Figure 1.15: Depth averaged, Antarctic-wide viscosity from an inversion model. From Arthern et al. (2015).

1.3.2 Limitations of Inverse Models

Inverse methods are ill-posed (see section 1.3), and this is an issue that must be dealt to ensure inversion outputs are meaningful and representative of reality. One such way that this ill-posedness is dealt with is by introducing regularization terms (e.g., Tikhonov regularization), however, each different regularization technique could introduce its own

bias (Barnes et al., 2021), and furthermore, regularization can cause small-scale features to be lost (Arthern et al., 2015).

There is also the issue of the nonlinearity of basal drag; to completely describe basal drag mathematically would mean introducing parameters that are not distinguishable by surface data alone, and to this end, governing equations for basal drag are oversimplified approximations (Arthern et al., 2015). Babaniyi et al. (2021) also highlight that ice velocity can be heavily dependent on properties of ice rheology, yet, ice rheology is not known exactly.

Another present problem is that ice velocity data represent motion that is due to both the deformation of ice as well as basal sliding, so when an inversion is performed, it is possible that basal drag is estimated incorrectly as the velocity due to ice deformation is not properly accounted for (Wilkens et al., 2015). This can be somewhat remedied by inverting for both the ice rigidity and drag coefficient simultaneously, which Ranganathan et al. (2021) demonstrate is effective in some circumstances, however, inverting for two parameters at once increases ill-posedness via extra regularization, as well as increases computational costs (Babaniyi et al., 2021).

1.4   Slessor Glacier, East Antarctica

1.4.1   Importance of the Study Area

The study area for this project is Slessor Glacier, East Antarctica (figure 1.16). There are two other glaciers in the immediate vicinity of Slessor Glacier, (1) Bailey Ice Stream (BIS), and (2) Recovery Glacier, and the three of these together account for 15% of Antarctica's grounded ice and drain 5% of Antarctica's fresh water into the Filchner Ice Shelf (Rignot et al., 2008, 2011), whereas Slessor itself has a sea level equivalent of 2.92 ± 0.04 m (Morlighem et al., 2020).
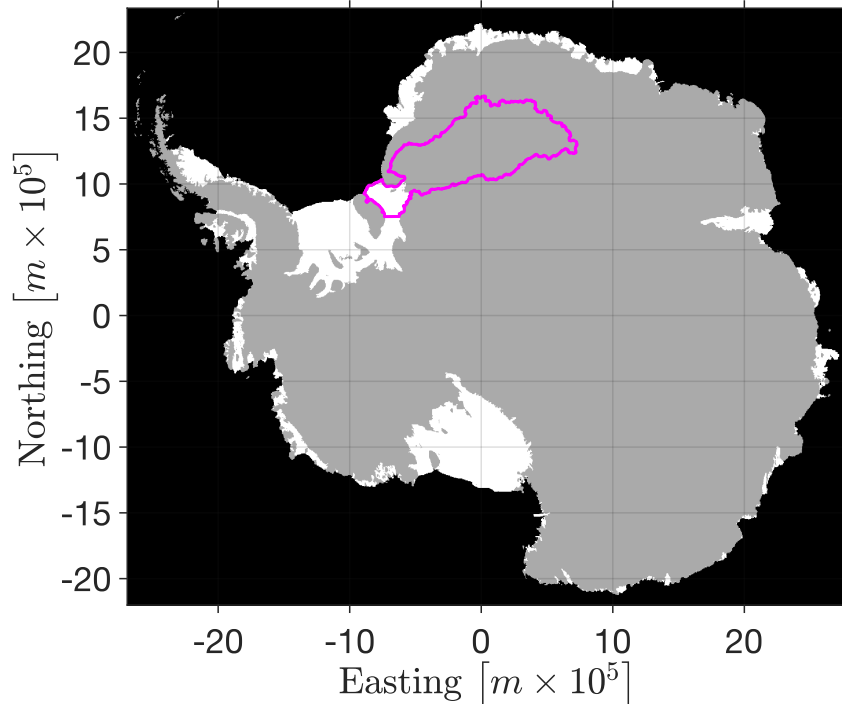
Figure 1.16: Outline of study on top of mask of Antarctic Ice Sheet in magenta. Black represents ocean water, white represents floating ice, and black represents grounded ice.

This is a crucial area for future sea level rise, as this area has been identified as not only the site for the majority of future ice loss in East Antarctica, but also an area with the potential to amplify climate variability on both a global and regional scale (Golledge et al., 2017; Bakker et al., 2017). Furthermore, Slessor Glacier is on a retrograde slope, meaning that it is susceptible to consequences of the Marine Ice-Sheet Instability (MISI) hypothesis.

The potential to impact sea level rise, amplify climate variability, and experience the MISI all make the Slessor Glacier study area important to understand in the future, and serve as a source of motivation to perform modeling studies of the subglacial hydrology and ice dynamics systems in the area.

1.4.2   Notable Features of Slessor Glacier

Much of the literature specifically related to Slessor Glacier is focused on basal conditions, topographic features, and subglacial lakes (e.g., Rippin et al., 2006; Koike et al., 2012; Diez et al., 2018). Rippin et al. (2006) highlights three troughs containing tributaries of enhanced ice flow at Slessor Glacier (figure 1.17):

1. A fast flowing tributary (STN in figure 1.17) containing the region's thickest ice (> 2800 m) lying in a deep topographic depression where ice flow is characterized by basal motion,

2. moderately fast flowing tributaries (STC and STS in figure 1.17) where ice flow is suggested to be solely from ice deformation,

3. and a third area (DSET in figure 1.17) with a smooth bed and slow ice flow with no basal motion.
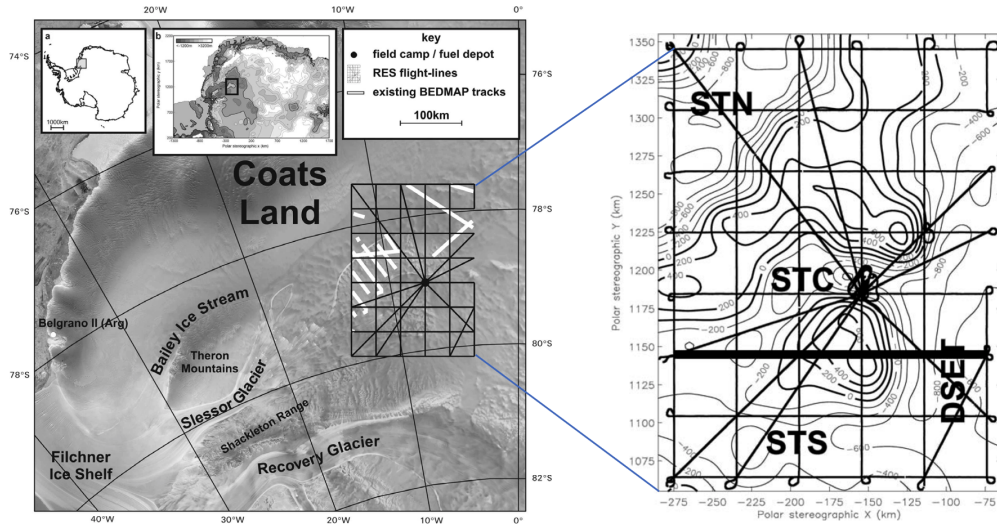
Figure 1.17: Left: mosaic of Antarctica with flight lines and field camp. Right: Close up of flight survey area with four troughs containing the investigated tributaries: Slessor tributary north (STN), Slessor tributary central (STC), Slessor tributary south (STS), and the deep southeastern trough (DSET). Adapted from Rippin et al. (2006).

Koike et al. (2012) highlight two distinct topographic features in a northern tributary of Slessor Glacier (figure 1.18) during an analysis of mosaic processing of SAR images[2].

---

[2]The synthetic aperture radar (SAR) microwave system is a remote sensing technique based on satellite observations Koike et al. (2012)
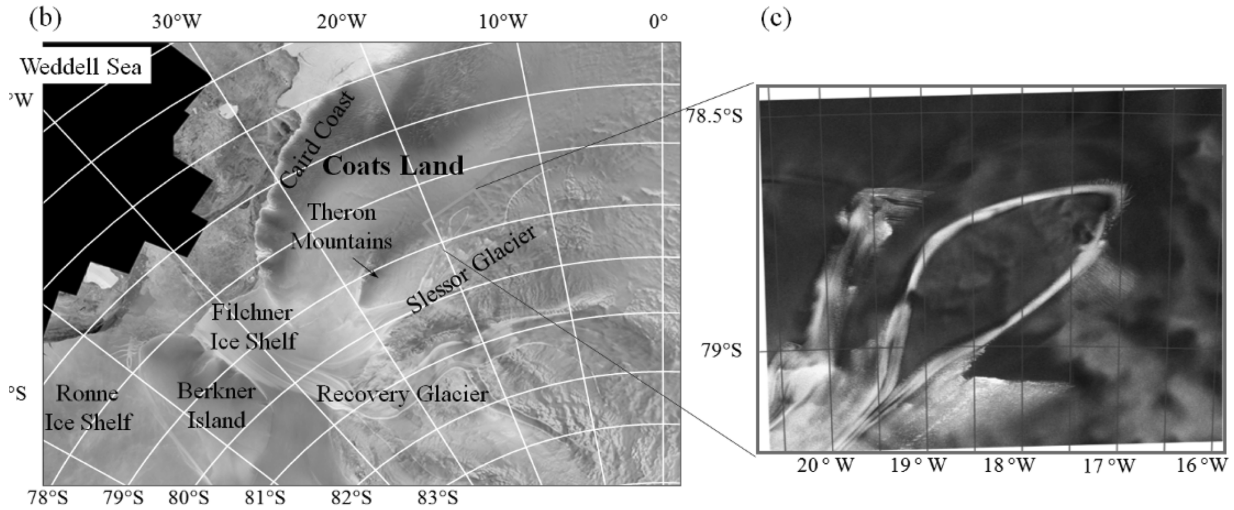
Figure 1.18: Left: Mosaic of the study area containing two features. Right: Enlargement of the two features found in the study area. On the left is the feather-shaped feature, and on the right is the oval shaped feature. Adapted from Koike et al. (2012).

The first surface feature they discuss is an oval shaped feature that is 60 km long in the longest axis, and 30 km long in the shortest axis (figure 1.18). The second surface feature is a feather-shaped feature that corresponds to a zone that is heavily crevassed. The oval shape feature has an escarpment on its east side that is 300 m high, as well as an escarpment on the west side that is 500 m high. As for the feather shaped feature, this is also situated in a valley that is surrounded by high escarpments. Magnetic lineaments perpendicular to the northern tributary of Slessor glacier are interpreted as faults (Shepherd et al., 2006), and these faults are oriented similarly to the zones of heavy crevassing found at the feather-shaped feature. Koike et al. (2012) suggested that these faults and their impact on the subglacial topography are causing the ice fractures and zones of heavy crevassing.

Slessor Glacier also hosts a network of subglacial lakes, and it is estimated that there are six active subglacial lakes beneath the glacier (Livingstone et al., 2022). The drainage of one of these lakes (Slessor$_{23}$ in 1.19) was captured using CryoSat-2 and ICESat-2 altimetry data (Siegfried et al., 2021), and to date, this was the most rapid lake drainage event ever captured in Antarctica, with volume changes up to $-227\mathrm{m}^3\mathrm{s}^{-1}$, which is $\sim 40\%$ larger by volume than the second largest drainage event captured (McMillan et al., 2013; Siegfried and Fricker, 2018).
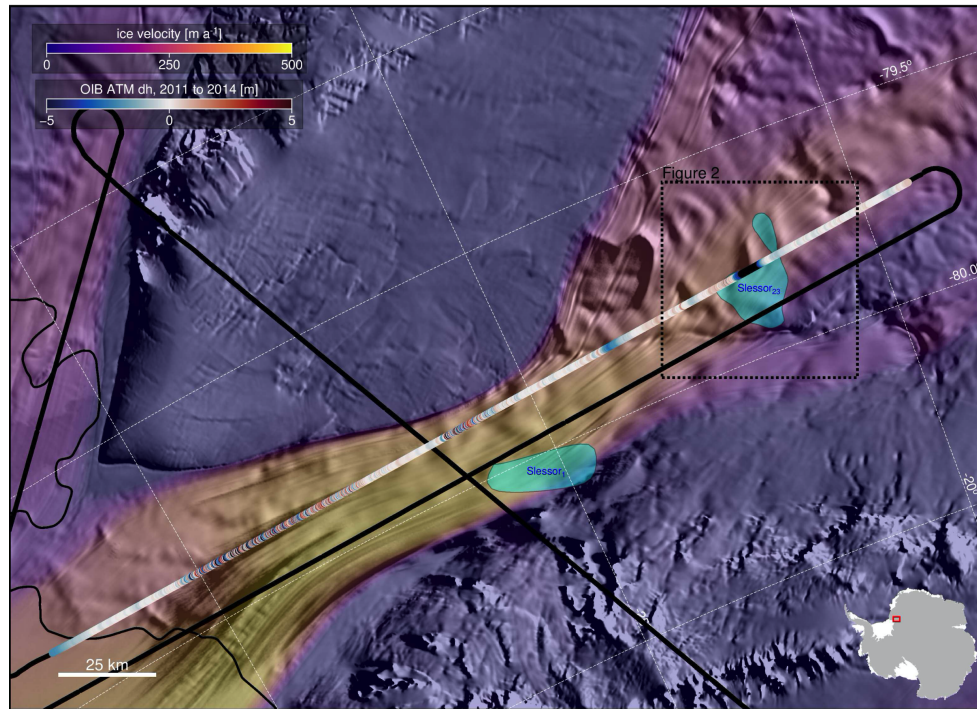
Figure 1.19: Slessor Glacier outlet containing subglacial lakes Slessor$_1$ and Slessor$_{23}$ (inset figure 2). The inset in the bottom right represents the location in Antarctica, the black lines indicate flight lines for Operation IceBridge, coloured circles along the flight line reflect surface-elevation change, and cyan polygons represent the subglacial lakes. From Siegfried et al. (2021).

The drainage event was captured by studying large surface height changes over the location of subglacial lake Slessor$_{23}$. When the lake drained, CryoSat-2 SARIn captured up to 40 m of surface lowering in the final nine months of 2014, and when the lake began to refill, ICESat-2 laser altimetry captured the recovery of the surface from March 2019 to September 2020, at a rate which Siegfried et al. (2021) approximate to be 0.67 m/month.

This study agrees well with one performed by Fan et al. (2022), where they obtained a time series of ice surface elevation changes based on data from CryoSat-2 and ICESat-2 altimetry data. In their time series, they captured a surface elevation change of 5.4 m over 7 months in 2019 (i.e., 0.77 m/month) where a high of 9.2 m was reached over subglacial lake Slessor$_{23}$. By extending the time series to present day, Fan et al. (2022) suggest that after the drainage event, Slessor$_{23}$ refilled in approximately 4 years, and that the entire drain/fill cycle of Slessor$_{23}$ took 5.6 years to complete, and as well, predict that another large-scale drainage event could occur in the near future.

1.5 Thesis Layout

This thesis addresses two research gaps in glaciology. The first gap is a lack of model validation techniques available to Antarctic subglacial hydrology and ice dynamics modelers in the absence of observed data. The second gap is the absence of an in-depth modeling project of subglacial hydrology and ice dynamics for Slessor Glacier, East Antarctica.

Validating model outputs is an important part of any hydrology modeling project, yet, in Antarctica there are few means of model validation available to modelers. This issue is significantly amplified should a modeler not have access to observed data (e.g., specularity content[3]) to compare their outputs to. In this thesis, an additional means of model validation is presented, assessing the consistency of model outputs between a subglacial hydrology model and an ice dynamics model. This is a novel practice in the field of glaciological modeling in Antarctica, and the results presented in this thesis serve as a basis to highlight the effectiveness of this method. In the process, the subglacial drainage network and basal friction coefficient of, mainly Slessor Glacier, but also BIS are investigated and quantified. This is an important project outcome as this area could become a key contributor to global sea-level rise in the future.

Chapter 2 will begin with a complete description of the GlaDS two-dimensional subglacial hydrology model (Werder et al., 2013). A breakdown of how the channel network is constructed along with relevant nomenclature is given, followed by a description of both the distributed and efficient drainage systems and their associated boundary conditions. The weak formulation and numerical solution are discussed and all relevant information for the subglacial hydrology model runs are given. The second part of chapter 2 will begin with a breakdown of the ice dynamics model, ISSM (Larour et al., 2012). This includes stating Glen's flow law and the three friction laws used in this project, as well a description of the mechanical (or stress balance) model, and the shelfy stream approximation (SSA) to the full Stokes equation. Next, the inverse method is presented along with a description of all relevant equations, parameters and coefficients. The methods used to invert high-resolution surface elevation data to investigate possible basal channel locations on the floating Filchner Ice Shelf are presented, and chapter 2 ends with a description of the study area. This includes the process of creating the catchment using a drainage basin delineation, followed by how the catchment is used to create meshes for each of the subglacial hydrology and ice dynamics models, which are each applied with their respective physics and mathematics.

Chapter 3 will first present the results of the sensitivity test and the inversion simulations. Outputs are presented from the GlaDS model, including water sheet thickness or volume, effective pressure, channel discharge, and channel cross-sectional area. The effects of varying sheet and channel conductivity, as well as water input and basal velocity will also be considered. Next, the results from 13 inversion simulations are presented. Results from the inversion simulation for ice rigidity over the floating ice shelf are presented first, followed by 12 inversion simulations calculating the basal drag coefficient from three

---

[3]Specularity data is derived from geophysical radar data and used to represent regions of distributed subglacial water accumulation (Schroeder et al., 2015; Dow et al., 2020).

different friction laws as prescribed by Weertman (1957), Budd et al. (1979) and Schoof (2005), where the latter two are forced by effective pressure outputs from GlaDS. Chapter 3 ends with a discussion of general trends across the model runs for both models used in this project.

Chapter 4 will be a discussion of the results presented in chapter 3 as well as a comparison of those results with ice shelf melt rates, ice shelf basal channels, and other work performed in the study area. This chapter begins with a recap on the outputs from the GlaDS and ISSM models, highlighting the importance of performing sensitivity tests and the usefulness of applying three different friction laws. The second part of chapter 4 compares and contrasts outputs from the two models used in this project, and in this section a discussion is given on how to decide which parameterizations are most appropriate, and how model outputs from the inversion simulation strengthen this decision. The appropriateness of the parameterizations are then investigated further by comparing GlaDS outputs to ice shelf data. Chapter 4 ends by comparing model results to previous modeling and observational work, and a breakdown of a tractable workflow for using ice dynamics modeling to validate subglacial hydrology models is presented.

Chapter 5 will conclude this thesis. A summary of the results in chapter 3 and conclusions drawn from them in chapter 4 will be given, highlighting the important takeaways from this project. Chapter 5 will end with a discussion regarding the limitations of the techniques used in this project, followed by suggested directions that future work should take.

Chapter 2

Methodology

2.1 The GlaDS Subglacial Hydrology Model

The two-dimensional Glacier Drainage System model (GlaDS) (Werder et al., 2013) is used to perform all the subglacial hydrology modeling for this project. The motivation behind choosing this model is two-fold:

1. the GlaDS model captures both the distributed and efficient subglacial drainage modes necessary to fully represent the subglacial hydrology of Antarctic glaciers, and

2. the GlaDS subglacial hydrology model has been extensively tested and applied in multiple glaciological contexts (e.g., Werder et al., 2013; Werder, 2016; Dow et al., 2018a,b; Wei et al., 2020; Dow et al., 2020; Indrigo et al., 2021).

The numerical framework of this model is a finite element method, and the model setup uses a two-dimensional, unstructured, triangular mesh comprised of elements, nodes, and edges, where variables modeled by parameterizations of several processes are stored at the nodes.

The channelized drainage system is based on the description given by Röthlisberger (1972), which can form on any edge of the mesh. The distributed drainage system is represented by a continuous water sheet with a varying thickness over the mesh elements, and water exchange is allowed between the two systems. A detailed breakdown of the GlaDS model following Werder et al. (2013), along with some updates as discussed by Dow et al. (2018b), will now be given.

2.1.1 The Channel Network

Before describing the physical and mathematical basis of the sheet and channel models, it is useful to define how the channel network is built, and then applied to the appropriate

mathematical object for numerical computation - a two-dimensional, unstructured, triangular mesh. The channel network, Γ, is comprised of channel segments (mesh edges), Γ_j, that partition the domain, Ω, into smaller subdomains (mesh elements), Ω_i. The vertices of Ω (mesh nodes) are denoted Λ, and it is at a vertex, Λ_k, where channel segments intersect. These intersection points are where channels exchange water, and it is along the edges where water is allowed to exchange with the adjacent subdomain's sheet. Surrounding the network is a boundary, $\partial\Omega$. A visualization of this is shown in figure 2.1.
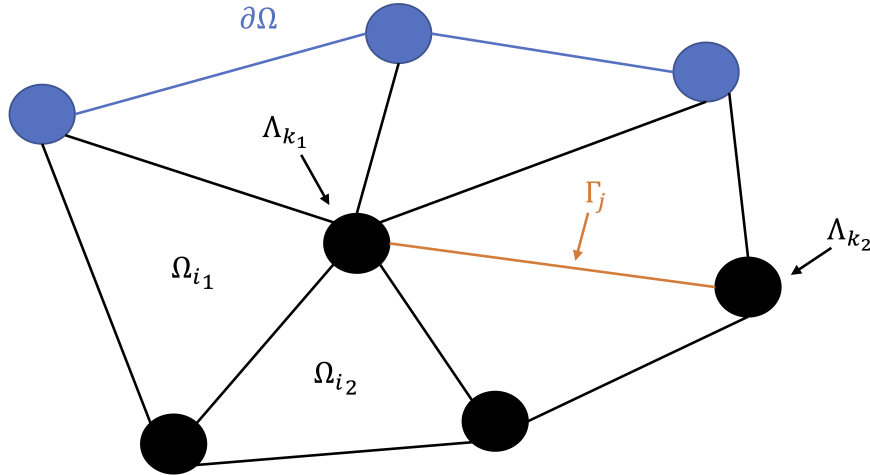
Figure 2.1: A portion of the channel network Γ connected to the domain boundary, $\partial\Omega$ (blue). The orange line, Γ_j, represents a typical edge that partitions the domain, Ω, into subdomains Ω_i, and the nodes, Λ_k, represent points where edges meet. Channels can only form on edges, and the sheet is constrained to subdomains. Adapted from Werder et al. (2013) and Brinkerhoff et al. (2021).

2.1.2 The Distributed System (Sheet Model)

The distributed system is captured by the sheet model first described by Hewitt (2011) which represents the system of linked cavity drainage as a continuum. Conservation of water is governed by

$$\frac{\partial h}{\partial t} + \nabla \cdot \mathbf{q} = m, \tag{2.1}$$

where h is the thickness of the water sheet, $\mathbf{q}$ is the sheet discharge, and m is a source term capturing both surface input and basal melt, and both saturation and incompressibility of the fluid are assumed. Equation (2.1) is a requirement of the distributed system, however $\partial h/\partial t$ and $\mathbf{q}$ are computed externally by other means.

The discharge of the sheet is given by the empirical relation

$$\mathbf{q} = -k_s h^\alpha |\nabla\phi|^{\beta-2}\nabla\phi, \tag{2.2}$$

where k_s is the conductivity of the sheet, $\nabla \phi$ is the gradient of hydraulic potential, and exponents $\alpha = 5/4$ and $\beta = 3/2$ are flow law exponents[1]. A discussion of motivation behind using an empirical law such as 2.2 was given in section 1.2, and equation (2.2) is analogous to equation (1.10). The evolution of the sheet is given by

$$\frac{\partial h}{\partial t} = \mathcal{O} - \mathcal{C} + \text{sheet}_{VF}, \tag{2.3}$$

where t is time, $\mathcal{O}$ and $\mathcal{C}$ parameterize the rates of cavity opening and closing respectively, and the final term on the right hand side, sheet_{VF}, represents a contribution to the sheet from viscous dissipation of potential energy and freeze-on (a negative pressure-melt term) as highlighted by Dow et al. (2018b) (see section 2.1.4 for explicit statement of sheet_{VF}).

The rate of cavity opening, $\mathcal{O}(h)$, has two states determined by whether or not the thickness of the distributed sheet, h, is less than the average bedrock height, h_r:

$$\mathcal{O} = \begin{cases} \frac{u_b(h_r - h)}{\ell_r}, & h < h_r \\ 0, & \text{otherwise}, \end{cases} \tag{2.4}$$

where u_b is the basal sliding speed and ℓ_r is the typical horizontal cavity spacing. This means that the rate of cavity opening is non-zero *only* when $h < h_r$. Cavity closure is controlled by viscous ice deformation, and is given by

$$\mathcal{C}(h, N) = \tilde{A}h|N|^{n-1}N, \tag{2.5}$$

where $\tilde{A}$ is a rheological property of ice, N is the effective pressure, and n is Glen's flow law exponent.

This model description of the sheet allows for a limited amount of water storage, but at a timescale that is too slow to capture storage phenomena observed in the proglacial system (Werder et al., 2013). To account for this, equation (2.1) is modified to include storage within an englacial aquifer:

$$\frac{\partial h}{\partial t} + \frac{\partial h_e}{\partial t} + \nabla \cdot \mathbf{q} = m, \tag{2.6}$$

where

$$h_e(p_w) = \frac{e_v p_w}{\rho_w g}, \tag{2.7}$$

is the volume of water stored per unit area of the bed, and e_v is the englacial void ratio.

2.1.3 The Efficient Drainage System (Channel Model)

Channel growth in this model follows what was prescribed by Röthlisberger (1972) in his idealized model of channel formation where flow is assumed to be saturated in either

---

[1]Constants α and β correspond to the empirical Darcy-Weisbach law where $\alpha = \beta = 1$ corresponds to laminar flow and $\alpha = 5/4, \beta = 3/2$ correspond to turbulent flow. Fountain and Walder (1998) provide a short discussion on geomorphological evidence for turbulent flow in cavities beneath glaciers

circular (englacial) or semi-circular (basal) channels, and these channels are referred to as R-channels. As water flows from high to low potential, the speed of the water in the elements increases and water also flows along the edges. This process causes viscous heat dissipation to melt the semi-circular R-channels, which lower the water pressure and pull more water from the distributed system. This is how the channelized drainage system forms in the GlaDS model, and a description of how the model captures this process will now be given.

The growth of an R-channel is governed by mass conservation:

$$\frac{\partial S}{\partial t} + \frac{\partial Q}{\partial s} = \frac{\Xi - \Pi}{\rho_w L} + m_c, \tag{2.8}$$

where S is the channel cross-sectional area, s is a coordinate aligned with the direction of flow within the channel, Q is the channel discharge, Ξ is the viscous dissipation of potential energy, Π is rate of change of the pressure-melt point per unit length of the channel, ρ_w is the density of water, L is the latent heat of fusion, and m_c is a source term that accounts for water entering the channel from the adjacent sheet. R-channels close due to ice creep, like the sheet, but open due to melting which has two main drivers. The first driver of melt is the viscous dissipation of potential energy, Ξ, given by

$$\Xi = \left| Q \frac{\partial \phi}{\partial s} \right| + \left| \ell_c q_c \frac{\partial \phi}{\partial s} \right|, \tag{2.9}$$

where Q is the channel discharge and

$$q_c = -k_s h^{\frac{5}{4}} \left| \frac{\partial \phi}{\partial s} \right|^{-\frac{1}{2}} \frac{\partial \phi}{\partial s} \tag{2.10}$$

is an approximation of discharge from the sheet with flow direction aligned with the channel. The second term on the right side of (2.9) represents a contribution from water flowing in the sheet below the channel at a width of ℓ_c, and this approximation is necessary because edges are one-dimensional lines, but channels are not - they have a width that reaches over the elements and so they must incorporate some of that water in the element.

The second driver is the changing pressure melting point of ice, given by

$$\Pi = -c_t c_w \rho_w (Q + f \ell_c q_c) \frac{\partial p_w}{\partial s}, \tag{2.11}$$

where c_t is the Clapeyron slope, c_w is the specific heat capacity of water, and f is a switch that does not allow the channel size to become negative:

$$f = \begin{cases} 1 & \text{, if } S > 0 \text{ or } q_c \frac{\partial p_w}{\partial s} > 0 \\ 0 & \text{, otherwise.} \end{cases} \tag{2.12}$$

Discharge in the channel network has a similar relation to the gradient of hydraulic potential as in the sheet model, and is captured by the Darcy-Weisbach turbulent flow parameterization,

$$Q = -k_c S^{\alpha_c} \left| \frac{\partial \phi}{\partial s} \right|^{\beta_c - 2} \frac{\partial \phi}{\partial s}, \tag{2.13}$$

where $\alpha_c = 5/4$ and $\beta_c = 3/2$ as per the Darcy-Weisbach relation for turbulent flow, and k_c is the channel conductivity. Werder et al. (2013) provides a relationship between the channel conductivity and the the Darcy-Weisbach friction factor, f_r:

$$k_c^2 = \frac{8}{\rho_w f_r \left(\frac{2}{\pi}\right)^{\frac{1}{2}} (\pi + 2)}. \tag{2.14}$$

The R-channel cross-sectional area, S, evolves over time, and this process is captured by

$$\frac{\partial S}{\partial t} = \frac{\Xi - \Pi}{\rho_i L} - \tilde{A}_c S |N|^{n-1} N, \tag{2.15}$$

where ρ_i is the density of ice, L is the latent heat of fusion, and $\tilde{A}_c$ is a rheological property of ice. In (2.15), the opening rate of the R-channel is the first term on the right, $(\Xi - \Pi)/\rho_i L$, and the closing rate is controlled by the second term, $\tilde{A}_c S |N|^{n-1} N$, i.e., ice creep.

An important point about ice in the GlaDS model is that it is assumed to be temperate (i.e. at the pressure melting point). This has implications for how the model captures changes in water volume, which is done by appropriately changing the amount of freezing or melting at a rate of $-\Pi/\rho_i L$.

2.1.4 Summary of Model Equations

At this point it is useful to summarize the model equations before discussing how they are numerically approximated. Now that (2.9) and (2.11) have been explicitly defined, (2.3) can be defined fully as

$$\frac{\partial h}{\partial t} = \frac{u_b (h_r - h)}{\ell_r} - \tilde{A} h |N|^{n-1} N + \frac{\Xi_s - \Pi_s}{\rho_i L}. \tag{2.16}$$

The notation of Ξ_s and Π_s is adopted from Dow et al. (2018b), and they have the similar formulas to (2.9) and (2.11) respectively, but with sheet discharge, q, and the gradient of hydraulic potential, $\nabla\phi$, as opposed to Q and $\partial\phi/\partial s$:

$$\Xi_s = q\nabla\phi \tag{2.17}$$

$$\Pi_s = -c_t c_w \rho_w q \frac{\partial p_w}{\partial s}. \tag{2.18}$$

Equation (2.16) is different than what was proposed originally by Werder et al. (2013) due to the addition of the third term on the right side of (2.16).

Equations (2.6), (2.7), and (2.16) can be combined to get

$$\mathcal{O} - \mathcal{C} + \frac{\Xi_s - \Pi_s}{\rho_i L} + \frac{e_v}{\rho_w g} \frac{\partial\phi}{\partial t} + \nabla \cdot \mathbf{q} - m = 0, \tag{2.19}$$

where the fourth term on the left of (2.19) comes from evaluating $\partial h_e/\partial t$. Equations (2.19) and (2.16) are the two sheet equations that hold over each mesh element/subdomain Ω_i, and $\mathbf{q}(h, \nabla\phi)$, $\mathcal{O}(h)$, and $\mathcal{C}(h, N)$ are given by (2.2), (2.4), and (2.5) respectively.

Similarly for the channel system, equations (2.8), (2.13), and (2.15) are combined to get

$$\frac{\partial Q}{\partial s} + \frac{\Xi - \Pi}{L}\left(\frac{1}{\rho_i} - \frac{1}{\rho_w}\right) - \tilde{A}_c S|N|^{n-1}N - m_c = 0. \tag{2.20}$$

Equation (2.20) along with (2.15) are the equations that hold over channel edges Γ_j that separate each subdomain Ω_i. Here, $\Xi\left(S, h, \frac{\partial\phi}{\partial s}\right)$, $\Pi\left(S, h, \frac{\partial\phi}{\partial s}\right)$, and $Q\left(S, \frac{\partial\phi}{\partial s}\right)$ are given by (2.9), (2.11), and (2.13) respectively.

At this point, it is also useful to note that water is conserved at each node in the network. This means that all channels connecting to any node must have their discharge sum to zero, i.e.,

$$\sum_j Q_j^k = 0, \tag{2.21}$$

where Q_j^k represents some channel j draining into node k, and the sum over j represents all channels flowing into vertex k. The sum in (2.21) may not equal zero in the case of a moulin draining into node k, however, this does not occur in Antarctica because there is insufficient surface melt for moulins to form, and so it is assumed that (2.21) holds over all nodes.

For each adjacent sheet, the source term m_c must balance flow. Thus,

$$m_c = \mathbf{q}\cdot\mathbf{n}|_{\partial\Omega_{i_1}} + \mathbf{q}\cdot\mathbf{n}|_{\partial\Omega_{i_2}}, \tag{2.22}$$

where $\mathbf{n}$ is the normal vector to the channel edge, and (2.22) must hold for each channel.

2.1.5 Model Boundary Conditions

Boundary conditions are applied to ϕ on the domain boundary, denoted $\partial\Omega$. The boundary conditions are either Dirichlet or Neumann conditions, where the former is typically a prescribed pressure applied to the domain outlet, $\partial\Omega_D$, and the latter is prescribed to the remainder of the model boundary, $\partial\Omega_N$, where there is typically zero flux. Together, the Dirichlet and Neumann sections of the boundary form the entire boundary: $\partial\Omega_D \cup \partial\Omega_N = \partial\Omega$.

The Dirichlet conditions are applied to the grounding line, and they take the form

$$\begin{aligned}\phi_D &= \min_{\partial\Omega_D} f_w(\phi_0 - \phi_m) + \phi_m \\ &= \min_{\partial\Omega_D} \phi_0 \\ &= \min_{\partial\Omega_D} \rho_i gH + \rho_w gB \quad \text{on} \quad \partial\Omega_D,\end{aligned} \tag{2.23}$$

for $f_w \approx 1$. Thus, the Dirichlet condition imposed on the grounding line is the minimum of ϕ_0, the overburden potential. This choice of boundary condition removes the possibility of unstable channel growth due to node-to-node circulation at the grounding line. The

Neumann boundary condition is applied to the rest of the boundary, and it allows for zero water flux:

$$\frac{\partial \phi}{\partial n} = \Psi_N \quad \text{on} \quad \partial \Omega_D, \tag{2.24}$$

corresponding to the specific discharge

$$q_N = -k_s h^{\frac{5}{4}} |\nabla \phi|^{-\frac{1}{2}} \Psi_N. \tag{2.25}$$

There are no flux conditions for channels as the model does not permit them to grow across $\partial \Omega_N$.

2.1.6 Weak Formulation

The model partial differential equations (PDEs) for ϕ are solved via weak forms. For the sheet model, this is done by multiplying (2.19) by a test function θ for all subdomains Ω_i, and then integrating by parts:

$$\theta(\mathcal{O} - \mathcal{C} - m) + \frac{\theta(\Xi_S - \Pi_s)}{\rho_i L} + \frac{\theta e_v}{\rho_w g} \frac{\partial \phi}{\partial t} + \theta \nabla \cdot \mathbf{q} = 0 \tag{2.26}$$

$$\int_{\Omega_i} \left[\frac{\theta e_v}{\rho_w g} \frac{\partial \phi}{\partial t} - \nabla \theta \cdot \mathbf{q} + \theta(\mathcal{O} - \mathcal{C} - m) + \frac{\theta(\Xi_s - \Pi_s)}{\rho_i L} \, d\Omega \right] + \int_{\partial \Omega_i} \theta \mathbf{q} \cdot \mathbf{n}|_{\partial \Omega_i} \, d\Gamma = 0. \tag{2.27}$$

Here, $\mathbf{n}$ is the outward normal vector to subdomain Ω_i.

Similarly, for the channel model, a test function is multiplied by (2.20) followed by integration by parts:

$$\theta \frac{\partial Q}{\partial s} + \theta \left[\frac{\Xi - \Pi}{L} \left(\frac{1}{\rho_i} + \frac{1}{\rho_w} \right) - \tilde{A}_c S |N|^{n-1} - m_c \right] = 0$$

$$\int_{\Gamma_j} \left[-\frac{\partial \theta}{\partial s} Q + \theta \left(\frac{\Xi - \Pi}{L} \left(\frac{1}{\rho_i} + \frac{1}{\rho_w} \right) - \tilde{A}_c S |N|^{n-1} N - m_c \right) d\Gamma \right] + [\theta Q_j]_-^+ = 0. \tag{2.28}$$

Here, $[\theta Q_j]_-^+$ means evaluating θQ_j at both endpoints of channel Γ_j. What is left to do is sum (2.26) and (2.28) over all Ω_i and Γ_j to generate an integral over all of Ω. This results in

$$\sum_{i=1}^{n_\Omega} \int_{\Omega_i} \left[\frac{\theta e_v}{\rho_w g} \frac{\partial \phi}{\partial t} - \nabla \theta \cdot \mathbf{q} + \theta(\mathcal{O} - \mathcal{C} - m) + \frac{\theta(\Xi_s - \Pi_s)}{\rho_i L} \, d\Omega \right] \tag{2.29}$$

$$+ \sum_{j=1}^{n_\Gamma} \int_{\Gamma_j} \theta \left[\mathbf{q} \cdot \mathbf{n}|_{\partial \Omega_{i_1}} + \mathbf{q} \cdot \mathbf{n}|_{\partial \Omega_{i_2}} - m_c \right] \, d\Gamma$$

$$+ \int_{\partial \Omega} \theta \mathbf{q} \cdot \mathbf{n} \, d\Gamma$$

$$+ \sum_{j=1}^{n_\Gamma} \int_{\Gamma_j} \left[-\frac{\partial \theta}{\partial s} Q + \theta \left(\frac{\Xi - \Pi}{L} \left(\frac{1}{\rho_i} - \frac{1}{\rho_w} \right) - \tilde{A}_c S |N|^{n-1} N \right) \right] \, d\Gamma$$

$$+ \sum_{k=1}^{n_\Lambda} \sum_{j=1}^{n_\Gamma} \theta Q_j^k = 0.$$

34

Here, N_Ω and N_Λ are the number of subdomains and nodes, and N_Γ is the number of edges in $\Omega \setminus \partial\Omega$. The second term in (2.29) reads

$$\sum_{j=1}^{N_\Omega} \int_{\Gamma_j} \theta \left(\mathbf{q} \cdot \mathbf{n}|_{\partial\Omega_{i_1}} + \mathbf{q} \cdot \mathbf{n}|_{\partial\Omega_{i_2}} - \mathbf{q} \cdot \mathbf{n}|_{\partial\Omega_{i_1}} - \mathbf{q} \cdot \mathbf{n}|_{\partial\Omega_{i_2}}\right) \, d\Gamma = 0, \tag{2.30}$$

as a consequence of (2.22), and so this term can be omitted from (2.29). Conservation at the nodes (equation (2.21)) means that the final term in (2.29) disappears as the sum will equal zero.

Lastly, homogeneous boundary conditions are imposed on θ such that $\theta = 0$ on $\partial\Omega_D$, and the Neumann boundary corresponds to the specific discharge (2.25), and so the third term in (2.29) is

$$\int_{\partial\Omega} \theta \mathbf{q} \cdot \mathbf{n} \, d\Gamma = \int_{\partial\Omega_N} \theta q_N \, d\Gamma. \tag{2.31}$$

This means that the final form of the weak form is

$$\sum_i \int_{\Omega_i} \left[\frac{\theta e_v}{\rho_w g} \frac{\partial \phi}{\partial t} - \nabla\theta \cdot \mathbf{q} + \theta(\mathcal{O} - \mathcal{C} - m) + \frac{\theta(\Xi_s - \Pi_s)}{\rho_i L} \, d\Omega \right] \tag{2.32}$$
$$+ \sum_j \int_{\Gamma_j} \left[-\frac{\partial \theta}{\partial s} Q + \theta \left(\frac{\Xi - \Pi}{L} \left(\frac{1}{\rho_i} - \frac{1}{\rho_w} \right) - \tilde{A}_c S |N|^{n-1} \right) \right] \, d\Gamma$$
$$+ \int_{\partial\Omega_N} \theta q_N \, d\Gamma = 0.$$

There does need to be a statement made regarding the exchange of water between the sheet model and channel model. Recall that the second term in (2.29) vanished. Since it was this term that was responsible for the water exchange between the sheet and channel models, this exchange is now implied implicitly. This is done by exchanging water at the necessary rate to uphold the assumption of water pressure remaining between the sheet and channels.

2.1.7 Overview of Model and Numerical Solution

Sheet discharge, rate of cavity opening, and rate of cavity closure are given by (2.2), (2.4) and (2.5) respectively:

$$\mathbf{q}(h, \nabla\phi) = -k_s h^{\frac{5}{4}} |\nabla\phi|^{-\frac{1}{2}} \nabla\phi,$$
$$\mathcal{O}(h) = \begin{cases} \frac{u_n(h_r - h)}{\ell_r} & , h < h_r \\ 0 & , \text{otherwise}, \end{cases}$$
$$\mathcal{C}(h, N) = \tilde{A} h |N|^{n-1} N.$$

The evolution equation for the sheet is given by (2.16):

$$\frac{\partial h}{\partial t} = \frac{u_b(h_r - h)}{\ell_r} - \tilde{A} h |N|^{n-1} N + \frac{\Xi_s - \Pi_s}{\rho_i L}.$$

35

Channel discharge, viscous dissipation of potential energy and changing pressure melting point of ice are given by (2.13), (2.9) and (2.11) respectively:

$$Q\left(S, \frac{\partial \phi}{\partial t}\right) = -k_c S^{\frac{5}{4}} \left|\frac{\partial \phi}{\partial t}\right|^{-\frac{1}{2}} \frac{\partial \phi}{\partial t},$$

$$\Xi\left(S, h, \frac{\partial \phi}{\partial s}\right) = \left|Q\frac{\partial \phi}{\partial s}\right| + \left|\ell_c q_c \frac{\partial \phi}{\partial s}\right|,$$

$$\Pi\left(S, h, \frac{\partial \phi}{\partial s}\right) = -c_t c_w \rho_w (Q + f\ell_c q_c)\frac{\partial}{\partial s}(\phi - \phi_m).$$

The evolution of the channel cross sectional area is given by (2.15):

$$\frac{\partial S}{\partial t} = \frac{\Xi - \Pi}{\rho_i L} - \tilde{A}_c S |N|^{n-1} N.$$

The weak form of the model solution is given by (2.32):

$$\sum_i \int_{\Omega_i} \left[\frac{\theta e_v}{\rho_w g}\frac{\partial \phi}{\partial t} - \nabla\theta \cdot \mathbf{q} + \theta(\mathcal{O} - \mathcal{C} - m) + \frac{\theta(\Xi_s - \Pi_s)}{\rho_i L} \, d\Omega\right]$$
$$+ \sum_j \int_{\Gamma_j} \left[-\frac{\partial\theta}{\partial s}Q + \theta\left(\frac{\Xi - \Pi}{L}\left(\frac{1}{\rho_i} - \frac{1}{\rho_w}\right) - \tilde{A}_c S |N|^{n-1} N\right)\right] \, d\Gamma$$
$$+ \int_{\partial\Omega_N} \theta q_N \, d\Gamma = 0.$$

A description of the numerical solution will now be given. A finite element method is used to solve (2.32), a parabolic equation for ϕ. The irregular triangular mesh partitions the domain, Ω, into triangles whose edges form the channel network Γ. First order elements, i.e., triangular elements that contain corner nodes only, discretize ϕ and h, and constant values defined at the mesh edges disctreize S. In the second summation of (2.32), integrals are evaluated over one-dimensional edges, which would typically mean their contribution vanishes. However, in the GlaDS model the contribution from these integrals is essential, and to this end their treatment becomes analogous to boundary conditions, but instead of prescribing boundary conditions solely on $\partial\Omega$, it occurs on all edges. This is implemented in the finite element method by using piecewise linear finite elements.

The two-dimensional finite element method used in GlaDS defines all finite element operators as sparse matrices as opposed to the standard for loop approach which is too slow when implemented in Matlab. This approach turns the finite element method assembly into a series of sparse matrix multiplications. In the GlaDS workflow, the function FEgrid.m defines the global operators for the finite element method. These include operators that compute integrals, derivatives, and averages between nodes, boundary edges and network edges. The code follows a method of lines to discretize space, leading to a coupled set of ordinary differential equations, which can be solved in several different ways. In this

project, the fully implicit `ode15s` solver within Matlab is used to perform time stepping and solve the stiff differential equation with a mass matrix formed using the finite element setup described above. The `ode15s` solver is used to avoid issues that come up when using explicit solvers for stiff systems of ordinary differential equations, e.g., integration failing or taking too long to complete.

2.1.8 Values for Independent Variables

The GlaDS model is being used for a sensitivity test, meaning many of the independent variables will be changing across model runs while others stay the same. Values for sheet and channel conductivity are uniform across the domain, and so their values are either raised or lowered, while water input and basal velocity can be either spatially variable or constant. Table (2.1) displays all values which do not change across model runs.

Table 2.1: Table of GlaDS model parameters that are not altered in the sensitivity test.

Variable	Symbol	Value	Units
Acceleration due to gravity	g	9.81	$m\ s^{-2}$
Latent heat	L	3.34×10^5	$J\ kg^{-1}$
Density of ice	ρ_i	910	$kg\ m^{-3}$
Density of water	ρ_w	1000	$kg\ m^{-3}$
Pressure melt coefficient	c_t	7.5×10^{-8}	$K\ Pa^{-1}$
Heat capacity of water	c_w	4.22×10^3	$J\ kg^{-1}\ K^{-1}$
Glen's n	n	3	Numerical constant
Ice flow constant - cavities	$\tilde{A}$	5×10^{-25}	$Pa^{-n}\ s^{-1}$
Ice flow constant - channels	$\tilde{A}_c$	5×10^{-25}	$Pa^{-n}\ s^{-1}$
Sheet width below channel	ℓ_c	2	m
Cavity spacing	ℓ_r	2	m
Bedrock bump height	h_r	0.1	m
Englacial void ratio	e_v	10^{-5}	Numerical constant
Bed elevation	B	BedMachine Data	m
Ice thickness	H	BedMachine Data	m

For the sheet and channel conductivities (k_s and k_c, respectively), the values used are

$$k_s \in \left[10^{-3}\ ,\ 10^{-4}\right]\ \mathrm{m}^{7/4}\mathrm{kg}^{-1/2} \tag{2.33}$$

$$k_c \in \left[10^{-1}\ ,\ 5 \times 10^{-2}\ ,\ 10^{-3}\right]\ \mathrm{m}^{7/4}\mathrm{kg}^{-1/2}. \tag{2.34}$$

The two variables that switch between synthetic and spatially variable are u_b, the basal velocity, and water input. The spatially variable data come from an Antarctic-wide approximation of basal velocity and water input following methods proposed by Seroussi et al.

(2020) (figure 2.2), and when constant, the basal velocity is set to a rate of 50 m/year and the water input is set up such that the initially input is 1 mm/year for the steady state runs, and for the transient runs, that value is increased up to 5 mm/year over the course of either one, two or three years.

(a)

(b)
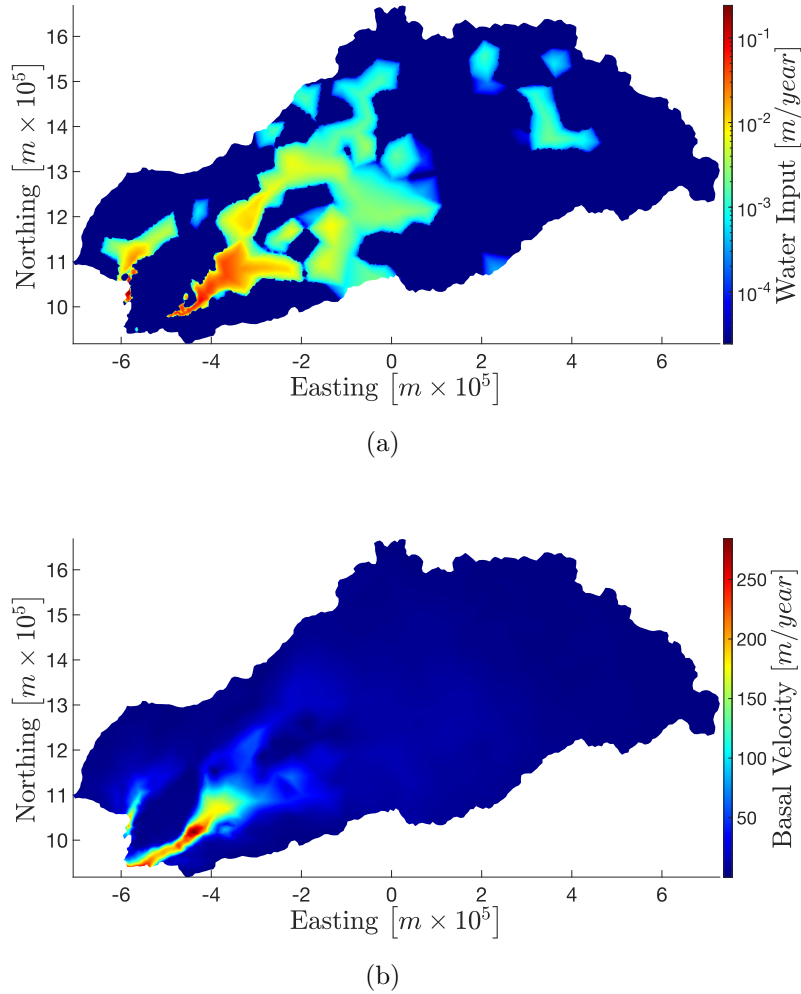
Figure 2.2: Spatially variable ISMIP6 data for (a) the water input (log scale), and (b) the basal velocity.

2.1.9 Performing GlaDS Model Runs

Before projecting into the future by performing a transient GlaDS model run, it is essential to spin up the models to steady state (SS). The SS run is an approximation of the subglacial hydrological system beneath Slessor Glacier prior to the transient run, and is an effective means to ensure consistency between the initial conditions of each transient run.

Each GlaDS transient run will differ from one another by varying either sheet conductivity, channel conductivity, basal velocity or water input. This is done to test the impact

of each parameter on the development of the subglacial hydrological system. Prior to each transient model run, a $40,000$ day SS run is performed, where SS is defined by a sufficiently small change in water sheet thickness for the majority of the nodes between the final two time steps of the SS model run. Ideally, SS would be achieved when the change in water sheet thickness for every node in the domain is $\leq 10^{-6}$ m. However, due to steep changes in basal topography in some localized areas of the study area, this was often not possible without an unrealistic amount of basal topography smoothing. To remedy this issue, the condition of every node hosting a change in water sheet thickness $\leq 10^{-6}$ m was relaxed to keep the topography more realistic, and to this end SS was accepted in the localized areas of steep topography when the change in water sheet thickness between the final two time steps was $\leq 10^{-4}$ m. For several SS runs, this requirement was not necessary, e.g., when channel conductivity is set to 10^{-1} $m^{7/4}kg^{-1/2}$ and sheet conductivity is 10^{-3} $m^{7/4}kg^{-1/2}$, SS is achieved with 99.35% of nodes hosting a change of $\leq 10^{-8}$ m.

It is worth noting that changing the variables k_s and k_c between the steady state and transient runs will result in errors, and so a steady state run for every combination of k_s and k_c is required. When the SS run completed, the $20,000$ day transient run can begin, where model runs will typically reach SS after $20,000$ days, but this is not a requirement. The only parameters that are allowed to change between the SS and transient runs are the water input and basal velocity. Prior to each transient run, water input and basal velocity must be specified, and either of the two can be constant (i.e. the linear ramp up scheme for water input) or spatially variable.

All combinations of basal velocity, water input, k_s, and k_c lead to a total of 48 runs for the sensitivity test (table 2.2). For both the SS and transient runs, values are output at 30 day intervals. This value is sufficient for this modeling project as the outputs at the end of the model are what will be compared to the outputs from the ice dynamics model, and thus a time step < 30 days is deemed unnecessary as it would needlessly increase computation time.

Table 2.2: Table of all combinations of parameters altered in the sensitivity test. Linear ramp up schemes start at an input of 1 mm/year and increase to 5 mm/year over the selected amount of years. SV stands for spatially variable.

$k_s \left[m^{7/4}kg^{-1/2}\right]$	$k_c \left[m^{3/4}kg^{-1/2}\right]$	Velocity	Water Input
10^{-3}, 10^{-4}	5×10^{-2}, 10^{-3}, 10^{-1}	50 m/year	Linear ramp up over 1 year
10^{-3}, 10^{-4}	5×10^{-2}, 10^{-3}, 10^{-1}	SV	Linear ramp up over 1 year
10^{-3}, 10^{-4}	5×10^{-2}, 10^{-3}, 10^{-1}	50 m/year	Linear ramp up over 2 years
10^{-3}, 10^{-4}	5×10^{-2}, 10^{-3}, 10^{-1}	SV	Linear ramp up over 2 years
10^{-3}, 10^{-4}	5×10^{-2}, 10^{-3}, 10^{-1}	50 m/year	Linear ramp up over 3 years
10^{-3}, 10^{-4}	5×10^{-2}, 10^{-3}, 10^{-1}	SV	Linear ramp up over 3 years
10^{-3}, 10^{-4}	5×10^{-2}, 10^{-3}, 10^{-1}	50 m/year	SV
10^{-3}, 10^{-4}	5×10^{-2}, 10^{-3}, 10^{-1}	SV	SV

The GlaDS model runs in the sensitivity test that use spatially variable data generated following Seroussi et al. (2020) for both basal velocity and water input will be considered the most realistic as a water input that is the same across the entire base of a glacier is unrealistic; these will be referred to as "base runs". To analyze the effect of changing either channel or sheet conductivity, only the base runs will be considered. Similarly, two base runs with high and low sheet conductivity will be compared to model runs that use either a constant water input following the linear ramp up scheme from section 2.1.8, or a constant basal velocity of 50 m/year to analyze the effects of these parameters on model outputs. A summary of these runs is presented in chapter 3, table 3.1.

2.2   The Ice Dynamics Model

Inverse simulations are performed using NASA's Ice-sheet and Sea-level System Model (ISSM) (Larour et al., 2012) and the M1QN3 inversion software (Gilbert and Lemaréchal, 1989). The inverse method will use MEaSUREs (Mouginot et al., 2019) surface velocity data to infer two parameters - the basal friction coefficient (sometimes called basal drag coefficient) and ice rigidity (sometimes called ice hardness/softness).

Ice rigidity is governed by Glen's flow law (Glen and Perutz, 1955),

$$\mu = \frac{\tilde{B}}{2\left(\dot{\varepsilon}_e^{1-\frac{1}{n}}\right)}, \tag{2.35}$$

where μ is the effective ice viscosity, $\tilde{B}$ is the ice rigidity, n is Glen's flow law exponent (sometimes called Glen's n) which is typically equal to 3,

$$\dot{\varepsilon}_e = \sqrt{\frac{1}{2}\sum_{i,j}\dot{\varepsilon}_{ij}^2} = \frac{1}{\sqrt{2}}\|\dot{\varepsilon}\|_F \tag{2.36}$$

is the effective strain rate, $\|\cdot\|_F$ is the Frobenius norm, and $\dot{\varepsilon}$ is the strain rate tensor. It is also possible to relate $\tilde{B}$ to the rheological property of ice, $\tilde{A}$, i.e., the flow rate factor in equation (2.5) through the Arrhenius equation

$$\tilde{B} = \left[\tilde{A}\exp\left(-\frac{Q_A}{RT^*}\right)\right]^{-\frac{1}{n}}, \tag{2.37}$$

where T is the temperature, Q_A is the activation energy required for ice creep, R is the universal gas constant, $T^* = T - \beta_t p$ is the absolute temperature corrected for the changing melting point due to pressure, β_t is the rate of change of the melting point due to pressure, p.

For basal friction, three friction laws are are considered, the first of which is the Weertman friction law (Weertman, 1957). The Weertman *sliding law* (i.e., the law is presented in terms of basal shear stress, has the form

$$u_s = C_w \tau_b^m, \tag{2.38}$$

where τ_b is the basal shear stress, C_w is the spatially variable Weertman friction coefficient and m is a positive friction law exponent. In ISSM, equation (2.38) is rewritten as a *friction law* (i.e., the equation is written in terms of sliding velocity, u_s):

$$\tau_b = C_w^2 |u_s|^{\frac{1}{m}-1} u_b. \tag{2.39}$$

There have been several different choices for m in the Weertman friction law, (e.g., a short discussion of what has been used in the literature is provided by Brondex et al., 2017), and so three values are selected to be tested here: $m = 1$, a linear relationship, along with $m = 2$ and $m = 3$. Joughin et al. (2010) conducted an inverse methods modeling study at Pine Island Glacier, West Antarctica, and found that $m = 3$ is appropriate for areas with hard beds, whereas $m \to 0$ is more appropriate where glacial till is present. In this study, $m = 3$ is adopted as the base value, however, other values of m are tested to ensure consistency between the three.

The second friction law considered in this study will be the Budd friction law (Budd et al., 1979). In ISSM, this law is presented in terms of basal shear stress:

$$\tau_b = C_B^2 N^r |u_s|^{s-1} u_s, \tag{2.40}$$

where C_B is the spatially variable Budd friction coefficient, N is effective pressure, and $r = q/p$ and $s = 1/p$ are friction law exponents. In recent modeling, $q = p = 1$ is the typical choice (Brondex et al., 2017), and is what this study adopts. The main difference between the Budd friction law and equation (2.39) is that there is a strong dependence on effective pressure introduced.

Sliding laws like equations (2.39) and (2.40) erroneously imply that basal drag can increase to arbitrarily high values. This contradicts the bound presented by Iken (1981) that suggests the quantity τ_b/N is restricted by the maximum up-slope angle aligned with the mean flow direction, β:

$$\frac{\tau_b}{N} \leq \tan(\beta). \tag{2.41}$$

Iken (1981) assumed a non-physical stair-shaped bed when deriving the bound, and Schoof (2005) points out that this could be the reason it was largely ignored in glaciology for so long. The logic behind equation (2.41) is easy to grasp; when flowing glacier ice meets a bed obstacle, compressive stress is high on the upstream side of the bedrock bump, and due to the hydrostatic control of mean normal stress, the high compressive stress is balanced by low compressive stress on the downstream side of the bed obstacle. Once compressive stress at the downstream side of the bed obstacle is sufficiently low, a cavity may open prohibiting further lowering of compressive stress, which in turn bounds the increase of compressive stress on the upstream side of the bed obstacle. This process is exactly what equation (2.41) represents, i.e., basal drag generation is limited by cavitation on the downstream side of bed obstacles.

This led Schoof (2005) to analytically generalize equation (2.41) to irregular beds which are far more representative of reality, and he derived a new friction law, which in ISSM reads

$$\tau_b = -\frac{C_S^2 |u_s|^{m-1} u_s}{\left(1 + \left(\frac{C_S^2}{C_{\max} N}\right)^{\frac{1}{m}} u_s\right)^m}, \tag{2.42}$$

where C_S is the spatially variable Schoof friction coefficient, m is an exponent typically equal to $1/3$, and $C_{\max}$ is Iken's bound, the left side of equation (2.41), which is typically between 0.17 and 0.84. This friction law reduces to a Weertman type friction law when effective pressures are high, and a Coulomb-type friction law ($\tau_b \sim C_{\max}\mathrm{N}$) when effective pressures are sufficiently low, i.e., water pressure is high enough that water-filled cavities can remain open despite the inward pressure due to ice creep (Schoof, 2005).

2.2.1 Mechanical Model

Inversions in ISSM are calculated using the shelfy stream approximation (SSA) to the full Stokes equation. An overview of the governing equations for SSA will now be given, following (Larour et al., 2012). Newton's third law gives rise to the conservation of momentum for an ice mass:

$$\rho\frac{D\vec{v}}{Dt} = \nabla \cdot \vec{\sigma} + \rho\vec{b}, \tag{2.43}$$

where ρ is the density of ice, $\vec{v}$ is the velocity, $\vec{\sigma}$ is the cauchy stress tensor and $\vec{b}$ is the body force. Acceleration ($D\vec{v}/Dt$) is deemed negligible and Stokes flow is assumed, and the only considered body force is gravity, which reduces (2.43) to

$$\nabla \cdot \vec{\sigma} + \rho\vec{g} = \vec{0}. \tag{2.44}$$

The relation (2.44) balances stress, and the incompressibility of flow is given by

$$\mathrm{Tr}\,(\dot{\varepsilon}) = 0, \tag{2.45}$$

where $\mathrm{Tr}\,(\dot{\varepsilon})$ is the trace operator acting on the strain rate tensor, $\dot{\varepsilon}$. The constitutive equation describing the deformation of ice is given by

$$\vec{\sigma}' = 2\mu\dot{\varepsilon}, \tag{2.46}$$

where μ is the effective viscosity, $\vec{\sigma}' = \vec{\sigma} + p\vec{I}$ is the deviatric stress tensor, and p and $\vec{I}$ are the ice pressure and and identity matrix, respectively. The relation (2.46) only involves the deviatoric stress tensor because ice is treated as being purely viscous and incompressible. Ice is treated as a non-Newtonian fluid because the effective viscosity is assumed to be nonlinear, and follows the generalized Glen's flow law (equations (2.35) and (2.36)). The constitutive equation (2.46) and (2.35) are combined to express (2.44) in terms of velocity

and pressure:

$$\frac{\partial}{\partial x}\left(2\mu\frac{\partial u}{\partial x}\right) + \frac{\partial}{\partial y}\left(\mu\frac{\partial u}{\partial y} + \mu\frac{\partial v}{\partial x}\right) + \frac{\partial}{\partial z}\left(\mu\frac{\partial u}{\partial z} + \frac{\partial w}{\partial x}\right) - \frac{\partial p}{\partial x} = 0 \qquad (2.47)$$

$$\frac{\partial}{\partial x}\left(\mu\frac{\partial u}{\partial y} + \mu\frac{\partial v}{\partial x}\right) + \frac{\partial}{\partial y}\left(2\mu\frac{\partial v}{\partial y}\right) + \frac{\partial}{\partial z}\left(\mu\frac{\partial v}{\partial z} + \mu\frac{\partial w}{\partial y}\right) - \frac{\partial p}{\partial y} = 0 \qquad (2.48)$$

$$\frac{\partial}{\partial x}\left(\mu\frac{\partial u}{\partial z} + \mu\frac{\partial w}{\partial x}\right) + \frac{\partial}{\partial y}\left(\mu\frac{\partial v}{\partial z} + \mu\frac{\partial w}{\partial y}\right) + \frac{\partial}{\partial z}\left(2\mu\frac{\partial w}{\partial z}\right) - \frac{\partial p}{\partial z} - \rho g = 0 \qquad (2.49)$$

$$\frac{\partial u}{\partial x} + \frac{\partial v}{\partial y} + \frac{\partial w}{\partial z} = 0. \qquad (2.50)$$

Here, u, v and w are the x, y and z components of velocity, respectively. Up to now, the equations have described the full-Stokes model, which computes four equations, (2.47), (2.48), (2.49) and (2.50) to calculate four unknowns, u, v, w and p, which is computationally demanding.

The next step towards deriving the SSA model is to derive the higher-order model, which reduces the full-Stokes model to three equations and three unknowns. The steps to derive the higher-order model will be omitted from this thesis, but are given by Larour et al. (2012). It is worth noting that the higher-order model assumes that horizontal gradients of vertical velocities are negligible, and that bridging effects[2] are negligible. Once the higher-order model is derived, a final assumption is made, that is, vertical shear is negligible. This final assumption reduces the system to just two equations with two unknowns, and this is the SSA. The assumption that vertical shear stress is negligible allows equations (2.47) and (2.48) to become

$$\frac{\partial}{\partial x}\left(4H\bar{\mu}\frac{\partial u}{\partial x} + 2H\bar{\mu}\frac{\partial v}{\partial y}\right) + \frac{\partial}{\partial y}\left(H\bar{\mu}\frac{\partial u}{\partial y} + H\bar{\mu}\frac{\partial v}{\partial x}\right) = \rho g H\frac{\partial s}{\partial x} \qquad (2.51)$$

$$\frac{\partial}{\partial y}\left(4H\bar{\mu}\frac{\partial v}{\partial y} + 2H\bar{\mu}\frac{\partial u}{\partial x}\right) + \frac{\partial}{\partial x}\left(H\bar{\mu}\frac{\partial u}{\partial y} + H\bar{\mu}\frac{\partial v}{\partial x}\right) = \rho g H\frac{\partial s}{\partial y}, \qquad (2.52)$$

where $\bar{\mu}$ is the depth-averaged ice viscosity, H is the ice thickness, and s is the surface elevation.

In ISSM, however, basal drag is introduced into this system, and it is written in the compact form,

$$\nabla \cdot (2\bar{\mu}H\dot{\varepsilon}_{\text{SSA1}}) - \alpha^2 v_x = \rho_i g H\frac{\partial s}{\partial x} \qquad (2.53)$$

$$\nabla \cdot (2\bar{\mu}H\dot{\varepsilon}_{\text{SSA2}}) - \alpha^2 v_y = \rho_i g H\frac{\partial s}{\partial y}, \qquad (2.54)$$

---

[2]Sometimes glaciers can act like bridges in that the normal stress on the bottom of the "bridge" is less than the weight of the overlaying ice, while at the ends of the bridge (i.e., abutment) the normal stress is greater than the weight of the overlaying ice.

where

$$\dot{\varepsilon}_{\text{SSA1}} = \begin{bmatrix} 2\frac{\partial v_x}{\partial x} + \frac{\partial v_y}{\partial y} \\[2ex] \frac{1}{2}\left(\frac{\partial v_x}{\partial y} + \frac{\partial v_y}{\partial x}\right) \end{bmatrix} \tag{2.55}$$

and

$$\dot{\varepsilon}_{\text{SSA2}} = \begin{bmatrix} \frac{1}{2}\left(\frac{\partial v_x}{\partial y} + \frac{\partial v_y}{\partial x}\right) \\[2ex] \frac{\partial v_x}{\partial x} + 2\frac{\partial v_y}{\partial y} \end{bmatrix}. \tag{2.56}$$

Here, α is the basal friction coefficient. One can note that in the ISSM version of the SSA equations, flow is accounted for on a floating ice shelf ($\alpha = 0$) as well as an ice stream ($\alpha > 0$).

Lastly, the following boundary conditions are imposed for the SSA approximation:

$$\dot{\varepsilon}_{\text{SSA1}} \cdot \vec{n} = 0 \quad \text{and} \quad \dot{\varepsilon}_{\text{SSA2}} \cdot \vec{n} = 0 \quad \text{on} \quad \Gamma_s, \tag{2.57}$$

$$2\bar{\mu}H\dot{\varepsilon}_{\text{SSA1}} \cdot \vec{n} = \left(\frac{1}{2}\rho_i g H^2 - \frac{1}{2}\rho_w g B^2\right) n_x \quad \text{and} \tag{2.58}$$

$$2\bar{\mu}H\dot{\varepsilon}_{\text{SSA2}} \cdot \vec{n} = \left(\frac{1}{2}\rho_i g H^2 - \frac{1}{2}\rho_w g B^2\right) n_y \quad \text{on} \quad \Gamma_w, \tag{2.59}$$

where, Γ_s is the surface of the ice sheet, Γ_w is the ice/water interface, $\vec{n}$ is the outward normal vector and z is a vertical coordinate pointing outward from sea-level.

2.2.2 The Inversion Method

Before discussing the inversion model, it is useful to define a couple of items. An adjoint equation is an equation of the form

$$\vec{x}_1 = L^T \vec{x}_2, \tag{2.60}$$

where L is a matrix operator, L^T is the adjoint of L that satisfies

$$\left\langle L^T \vec{x}_2, \vec{x}_1 \right\rangle = \left\langle \vec{x}_2, L\vec{x}_1 \right\rangle, \tag{2.61}$$

$\vec{x}_1$ and $\vec{x}_2$ are vectors, and $\langle \cdot, \cdot \rangle$ is an inner product. An adjoint model is comprised of adjoint equations (as described above) that map a sensitivity gradient vector,

$$\nabla_x J(t_1) = L^T \nabla_x J(t_2) \tag{2.62}$$

from time t_2 to an earlier time t_1. Here, J is a scalar function and ∇_x is a gradient operating over the model state vector x.

In ISSM, the inverse method is a *variational method* that consists of minimizing a cost function, $\mathcal{J}$, that measures the misfit between an observed quantity, and a modeled quantity (a thorough discussion of variational methods is given by Nardi et al., 2009). The variational method is useful because it alters the control parameter (e.g., basal friction)

to match modeled quantities (e.g., those calculated by the SSA model in section 2.2.1) to observed quantities. The final product is the altered control parameter that corresponds to the observations. The general flow of a variational is given in figure 2.3, which shows the basic iterative process which stops for some given convergence criterion.
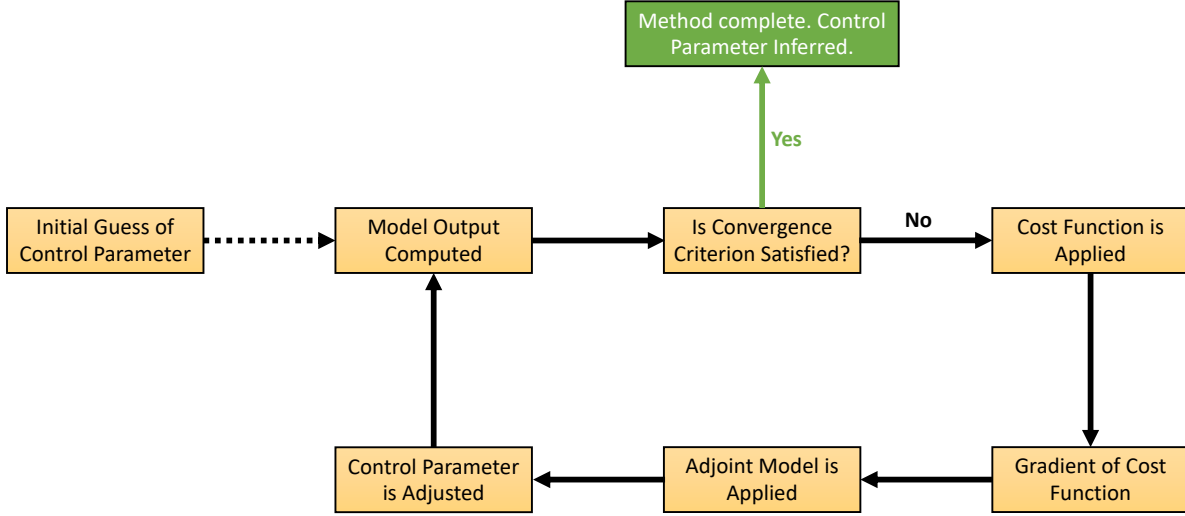
Figure 2.3: Flow chart of the iterative process of a variational inverse method. Adapted from Nardi et al. (2009).

There are several choices for minimization algorithms within ISSM, however, for this project the M1QN3 minimization algorithm is used (Gilbert and Lemaréchal, 1989).

For all inversions, two standard misfit cost functions are used, along with a regularization term that penalizes non-physical wiggles in the solution. The two misfit functions are the surface absolute velocity misfit,

$$\mathcal{J}_{101} = \gamma_{101} \int_S \frac{1}{2} \left(\left(u_x - u_x^{\mathrm{OBS}} \right) + \left(u_y - u_y^{\mathrm{OBS}} \right) \right) \ dS, \tag{2.63}$$

and the logarithmic velocity misfit,

$$\mathcal{J}_{103} = \gamma_{103} \int_S \left(\log \left(\frac{\|u_b\| + \epsilon}{\|u_s^{\mathrm{OBS}}\| + \epsilon} \right) \right)^2 \ dS. \tag{2.64}$$

Here, u_x is the x component of the modeled glacier velocity, u_y is the y component of the modeled glacier velocity, u_x^{OBS} is the x component of the observed glacier velocity, u_y^{OBS} is the y component of the observed glacier velocity, u_s is the modeled velocity vector, u_a^{OBS} is the observed velocity vector, ϵ is a minimum velocity to avoid division by zero, and γ_{101}, γ_{103} are weights that control the contributions of cost functions $\mathcal{J}_{101}$ and $\mathcal{J}_{103}$

respectively. The reason both cost functions (2.63) and (2.64) are used together is to ensure that the inversion accounts for the nonlinearity of ice velocity, i.e., both the fast- and slow-moving sections of ice. Cost function (2.63) is efficient at capturing areas of fast-flowing velocity and cost function (2.64) measures the natural log of the misfit, therefore efficiently capturing slow-moving areas (Larour et al., 2012; Morlighem et al., 2013).

Cost functions (2.63) and (2.64) are sufficient to run an inversion that will match the observations, however, non-physical, large gradients appear in the solution field of the control parameter as a result of the ill-posedness. This happens because all the algorithm is doing is lowering the mismatch between the modeled and observed velocities by altering the control parameter, it does not take into account what might be physical or non-physical, and so the large gradients allow the mismatch to be lowered. To account for this, a Tikhonov regularization term is introduced to the cost function that penalizes large gradients in the solution field of the control parameter. For ice rigidity inversions, the regularization term has the form

$$\mathcal{J}_{502} = \gamma_{502} \int_B \frac{1}{2} \left\| \nabla \tilde{B} \right\|^2 \, dB, \tag{2.65}$$

which includes the Tikhonov regularization coefficient, γ_{502}. Similarly for friction inversions, the regularization term is

$$\mathcal{J}_{501} = \gamma_{501} \int_B \frac{1}{2} \left\| \nabla k \right\|^2 \, dB, \tag{2.66}$$

where γ_{501} is the Tikhonov regularization coefficient, and $k = C_w, C_B$ or C_S are the spatially variable friction coefficient for the selected friction law.

Using the Tikhonov regularization term does come with a caveat that requires special treatment. While the regularization decreases the non-physical gradients in the solution, it does so at the cost of increasing misfit between the modeled and observed velocity fields. To treat this, one can lower or raise the Tikhonov regularization coefficient (γ_{501} and γ_{502}), which will in turn lower misfit or decrease the non-physical gradients respectively. Therefore, the ideal Tikhonov regularization coefficient is the optimal trade-off between fitting the observed velocity, and decreaseing non-physical gradients. To find this optimal parameter, one option is the L-curve analysis (Hansen, 2001). The L-curve analysis is performed by calculating ($\mathcal{J}_{101} + \mathcal{J}_{103}$) and $\mathcal{J}_{502}$ for several (10 in this project) different values of the Tikhonov regularization coefficient. Once this is completed, a log-log plot is created and the optimal Tikhonov regularization coefficient is chosen by selecting the value that forms the "corner" of the curve.

The procedure for determining the appropriate values of the non-regularization cost function coefficients, γ_{101} and γ_{103}, is to start with $\gamma_{101} = \gamma_{103} = 1$, run an inversion simulation, and then tune γ_{101} such that the contribution of $\mathcal{J}_{101}$ to the total cost function (e.g., equation 2.67) for an ice rigidity inversion) is of equal magnitude to that from $\mathcal{J}_{103}$. Selecting the appropriate value for the Tikhonov regularization coefficient is not so straightforward, and an L-curve analysis must be performed.

Putting this all together yields complete cost functions for ice rigidity,

$$\mathcal{J}_{\tilde{B}} = \mathcal{J}_{101} + \mathcal{J}_{103} + \mathcal{J}_{502}, \tag{2.67}$$

and basal drag,

$$\mathcal{J}_k = \mathcal{J}_{101} + \mathcal{J}_{103} + \mathcal{J}_{501}. \tag{2.68}$$

With the cost functions and their coefficients specified, the inverse method is ready to compute. The first parameter inverted for is the ice rigidity field over the floating ice shelf only and, for the grounded part of the domain, the ice rigidity field is approximated following the method suggested by using the Budd and Jacka temperature-dependent flow rate parameterization (Budd and Jacka, 1989). The inversion for friction coefficients are computed after the ice rigidity, as the ice rigidity field is to be used as an initial paramtere for the friction inversion.

2.2.3 Performing ISSM Model Runs

Several parameters are necessary to run the inversion simulations in ISSM. Bed and surface topography, ice thickness and mask data are taken from BedMachine (Morlighem et al., 2020). Near surface temperature and surface mass balance data are taken from the RACMO2.3 data sets (Van Wessem et al., 2014; Van Wessem and Laffin, 2020), and geothermal heat flux data is from Stål et al. (2021).

ISSM has a built in function, `SetMarineIceSheetBC` that automatically sets appropriate boundary conditions to the domain outline for inversion and stress balance simulations. Neumann boundary conditions are applied on the ice front to allow flux, and Dirichlet boundary conditions are applied elsewhere to constrain velocity.

For each inversion, there are several parameters that must be initialized prior to the model run.

Table 2.3: Initial parameters necessary to initialize each inverse method. Effective pressures driving the Budd and Friction law inversions are computed from base runs in the sensitivity test.

Control Parameter	Glen's n	m	r	s	N	$C_{\max}$
$\tilde{B}$	3	-	-	-	-	-
C_w	-	$1, 2, 3$	-	-	-	-
C_b	-	-	1	1	Computed Externally	-
C_s	-	$1/3$	-	-	Computed Externally	0.8

Iken's bound is set to 0.8 as the inverse method was showing a high misfit between observed and modeled velocities at the Theron Mountains when low values within the acceptable range of Iken's bound were used (more details about this bound are provided by Schoof, 2005).

Inversion results will be displayed differently than those from hydrology due to the fact that inverse methods do not project into the future, but rather infer quantities based on velocity data at a given time in the past. The difference between the stress balance simulation and observed velocities are presented to see how well the inverse method handled areas that are prone to numerical errors, such as areas hosting steep topographic depressions and/or areas of fast observed ice flow. Though, it is important to note that this is not a measure of how accurately the model predicts the ice rigidity or friction coefficient fields, but rather how well the inverse method can handle calculating these fields in problematic areas. In chapter 4, the outputs from the hydrology and inversion model are compared, with an examination of whether or not the outputs from the inversion simulations are physical and/or realistic.

2.3   The Study Area

The study area covers the primary drainage basin for Slessor Glacier, East Antarctica. Basal, surface, mask, $x-$ and $y-$extent data are taken from the Bedmachine Antarctica data set (Morlighem et al., 2020) at a resolution of 500 m in the WGS84/Antarctic Stereographic coordinate system. In the region containing Slessor Glacier, the basal topography ranges from approximately -4000 m to 2000 m, and the surface data ranges from 0 m to approximately 3500 m (figure 2.4).
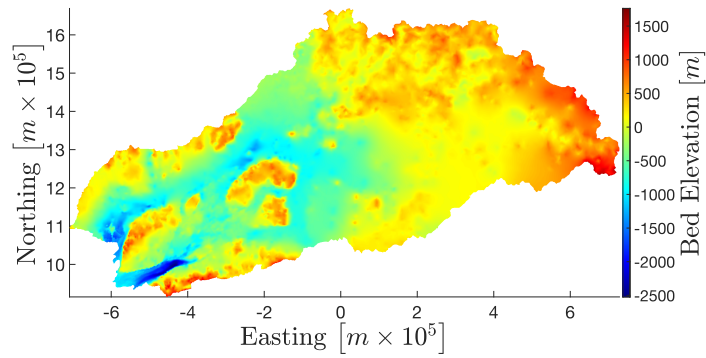
(a)
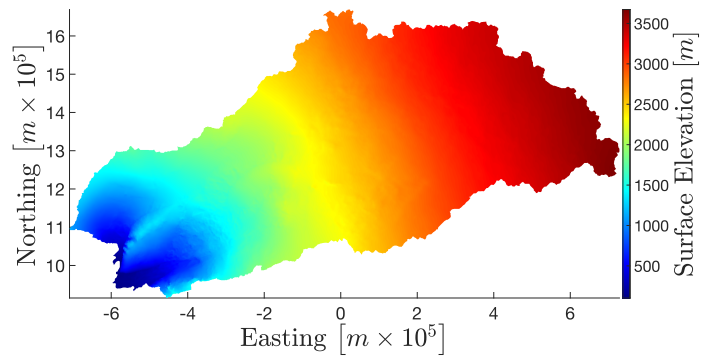
(b)
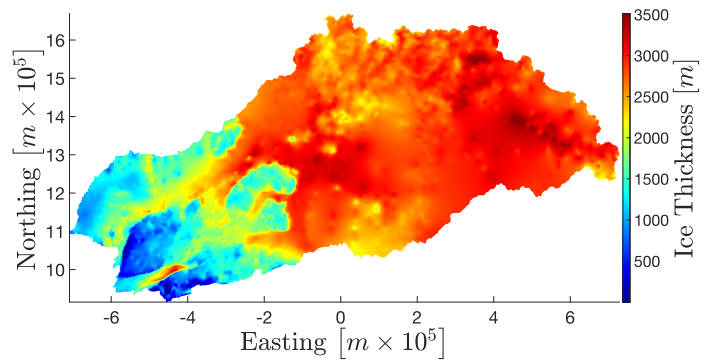
(c)

Figure 2.4: Topographies at the Slessor Glacier study area. (a) Bed elevation, (b) surface elevation and (c) ice thickness. For subplots (a) and (b), the elevations are in meters with respect to the height above sea level.

49

There are several basal topographic locations that are useful to highlight for reference in the remainder of this thesis (figure 2.5). For the three tributaries of Slessor Glacier (figure 1.17), the nomenclature from Rippin et al. (2006) will be adopted, where STN, STC and STS refer to Slessor tributary north, Slessor tributary central and Slessor tributary south, respectively. The two main drainage pathways are Slessor Glacier, the Bailey Ice Stream (BIS), and there is a deep trough just upstream from the grounding line of Slessor Glacier that will be referred to as the Deep Downstream Trough (DDT). The extent of the DDT is from approximately -5 to -4×10^5 m easting, and -9.5 to 10×10^5 m northing. Lastly, there are three areas of locally high topography downstream of the domain, and these will be referred to by their common names, Touchdown Hills, Theron Mountains and the Shackleton Range.
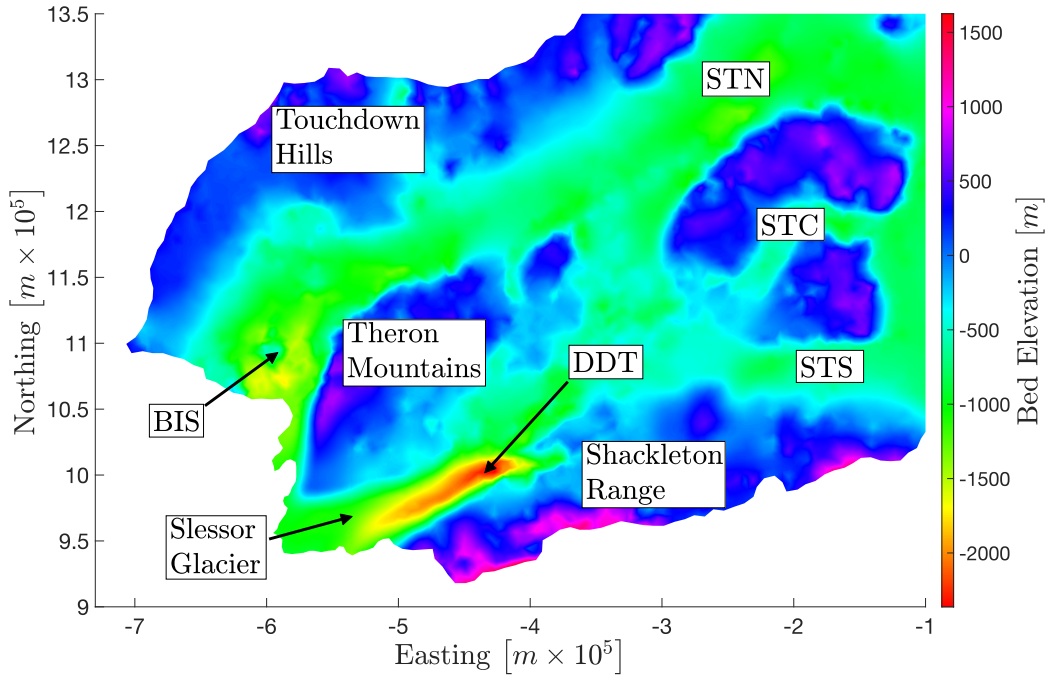
Figure 2.5: Slessor Glacier bed topography with key area labels overlain. Bed elevation is in meters with respect to the height above sea level.

Some of the bed and surface topography data must be smoothed to avoid numerical error that will cause the model run to fail, and so smoothing is performed at these locations only, to retain as much of the original topography as possible (figure 2.6). All topography smoothing was done using the `smooth2a` Matlab function (Reeves, 2022). Moreover, there are areas in the Shackleton Range, Theron Mountains, and Touchdown hills that contain exposed bedrock, and to account for this, a minimum ice thickness of 100 m is imposed on any area of ice where the thickness is ≤ 100 m.
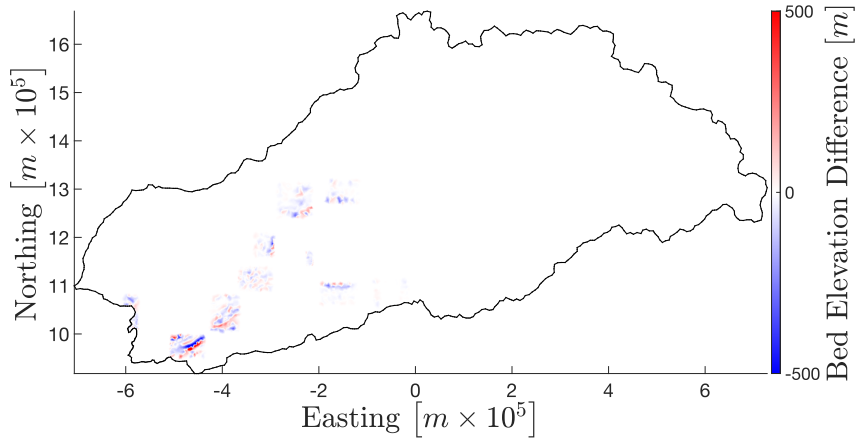
(a)
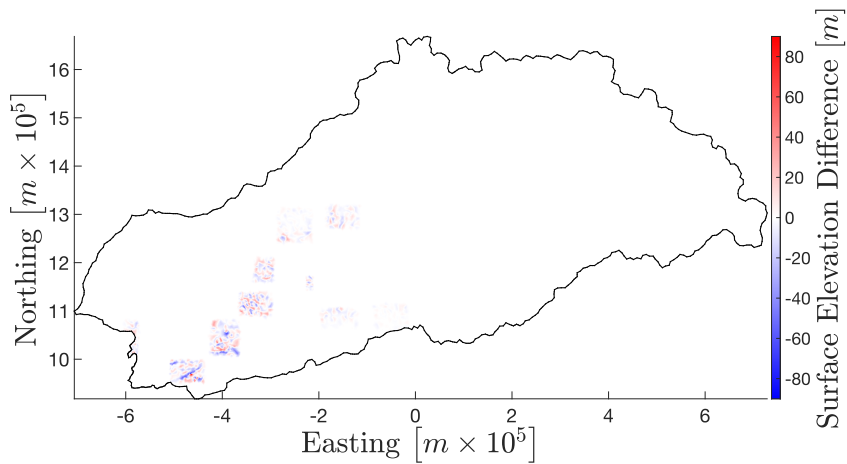
(b)

Figure 2.6: (a) Difference between BedMachine and smoothed basal topography. (b) Difference between BedMachine and smoothed surface topography. Outline of catchment in black.

2.3.1 Mesh Creation Procedure

To create the two meshes necessary for GlaDS and ISSM the first step is to extract the subglacial drainage basins in this area. Hydropotential is defined as

$$\phi = p_w + \phi_m, \tag{2.69}$$

where p_w is water pressure and ϕ_m is the elevation potential, both measured in pascals. Elevation potential is calculated by

$$\phi_m = \rho_w gB, \tag{2.70}$$

where ρ_w is the density of water, g is the acceleration due to gravity, and B is the bed elevation. A simplification is made in order to calculate p_w in equation (2.69) as basal water pressure is unknown, and this is done by defining ϕ by ice geometry only and introducing a flotation fraction,

$$f_w = \frac{p_w}{p_i}, \tag{2.71}$$

where p_i is the pressure exerted by the ice. This allows p_w to be written as

$$p_w = p_w \frac{p_i}{p_i} = f_w p_i = f_w \rho_i gH, \tag{2.72}$$

where ρ_i is the density of ice in and H is the thickness of ice. Approximating $f_w = 1$ yields

$$\phi = \rho_w gB + \rho_i gH, \tag{2.73}$$

and this equation applied everywhere in the domain. This creates a hydraulic potential model (similar to a digital elevation model) which is used to calculate flux routing with the `TopoToolbox` software in Matlab (Schwanghart and Scherler, 2014). Topographic depressions are filled to enable continuous flow towards the edges of the domain, and then a flow direction object is created which is used to create a map of subglacial drainage basins (figure 2.7).
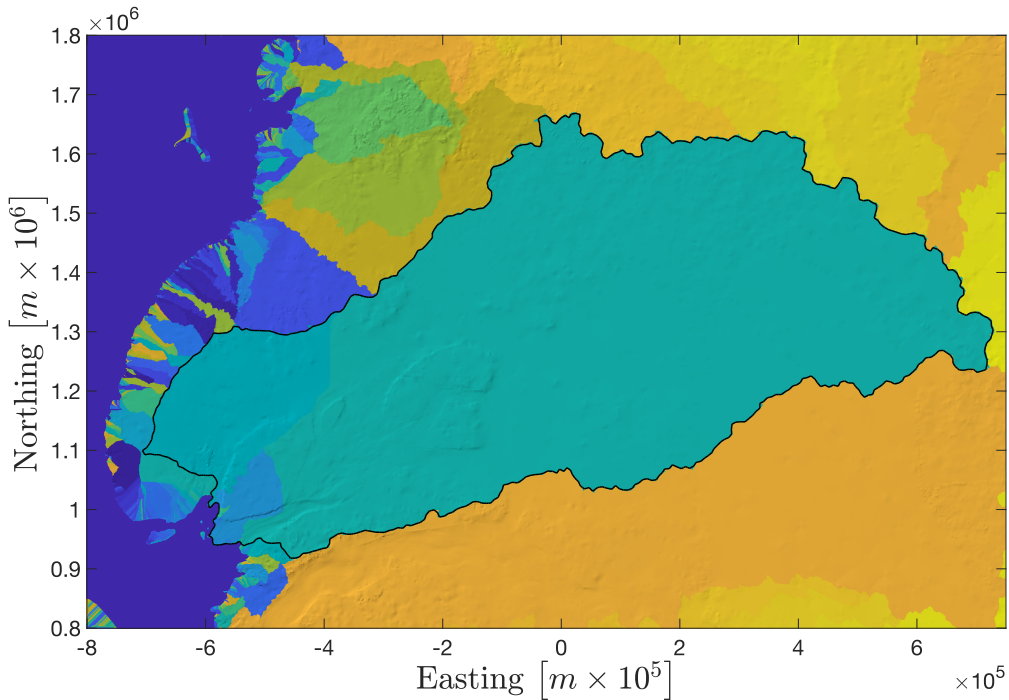
Figure 2.7: Drainage basin delineation at Slessor Glacier study area with hillside shading representing basal topographic depressions. Drainage basins are separated by colour.

To create the catchment for Slessor Glacier, the necessary drainage basins (figure 2.7) are selected manually, and an outline surrounding all of the drainage basins creates the outline for the entire catchment. This outline is then input to the mesh creating software Triangle (Shewchuk, 2002).

The GlaDS Mesh

The output from Triangle is an unstructured, triangular, refined mesh containing $20,233$ nodes, $59,951$ edges and $39,719$ triangular elements (figure 2.8). The number of nodes is constrained to approximately $20,000$ due to limitations introduced by processing in Matlab, and beyond this number, model efficiency goes down (Dow et al., 2018a,b). The mesh has been refined at several locations, with the largest area of refinement near the grounding line where ice velocity is the highest, and where there is a large topographic depression at the base of the glacier. Upglacier, there are five additional areas containing subglacial lake locations as specified by Smith et al. (2009). Across the entire domain the mean edge length between two nodes is 5.78×10^3 m, and the mean area of a triangular element is 1.43×10^7 m^2. In the refined areas, the mean edge length between two nodes is 2.22×10^3 m, and the mean area of a triangular element is 1.94×10^6 m^2.
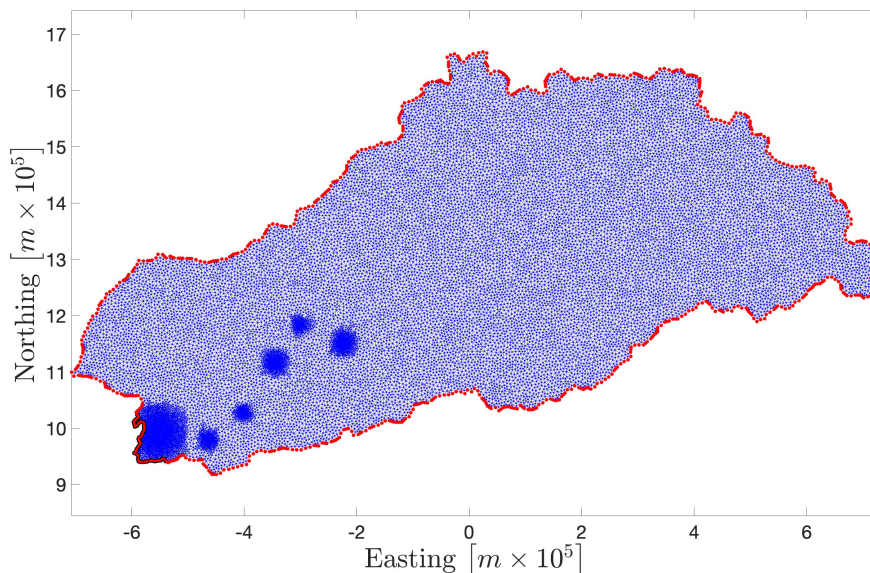
Figure 2.8: Refined, unstrucutred, triangular mesh of Slessor domain to be used for GlaDS Subglacial hydrology simulations. Red dots represent boundary nodes. Mesh is refined near outlet and at several predicted subglacial lake locations. Red nodes outlined with black represent nodes on the grounding line.

The ISSM Mesh

The domain for the ISSM model runs is different from what was used for the GlaDS model as the floating ice shelf was included for ice rigidity inversions, and in ISSM, the

mesh is not constrained to $\sim 20,000$ nodes. For this project, $\sim 70,000$ nodes was ideal for a tradeoff between computation time and spatial resolution. The unstructured, triangular mesh is created using the Bidimensional Anisotropic Mesh Generator (BAMG) (Hecht, 1998), and is refined according to the observed velocity field from MeASUREs (Mouginot et al., 2019) (figure 2.9). There are $72,201$ nodes, $213,066$ edges and $140,866$ triangular element, with a minimum edge length of 1.6×10^3 m, which corresponds to an area of approximately 1×10^6 m^2, and the largest triangles have edge lengths of $\sim 10^4$ m and areas of $\sim 10^7$ m^2.
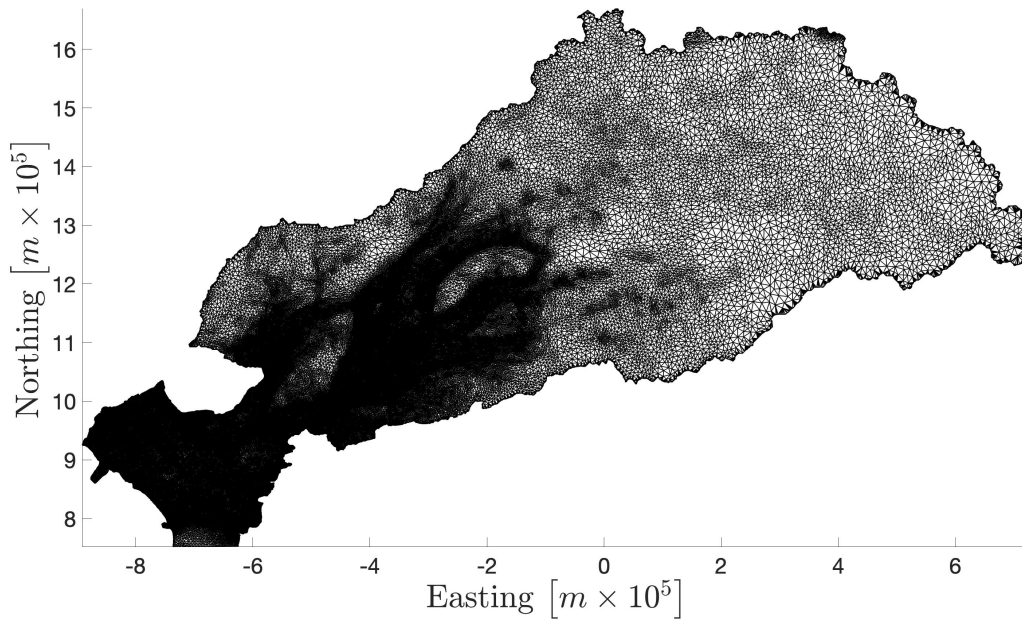
Figure 2.9: Refined, unstrucutred, triangular mesh of Slessor domain for ISSM inversion and stress balance simulations.

Finally, the MeASUREs observed ice velocities in Antarctica are interpolated onto the mesh in figure 2.9, to be used as the observable for the inverse methods (figure 2.10).
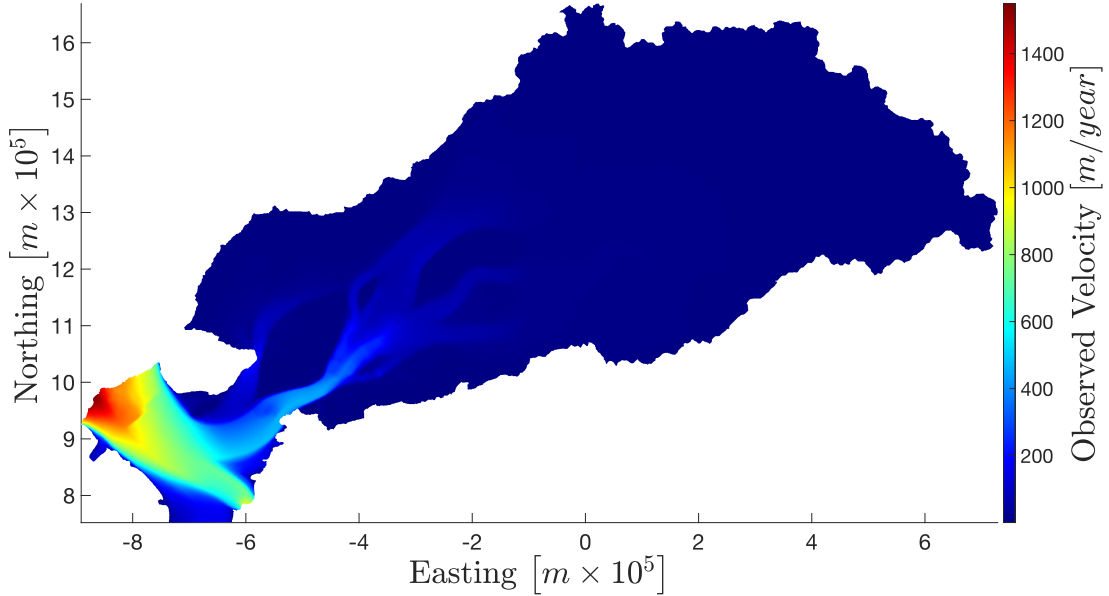
Figure 2.10: Observed MeASUREs velocity field to be used as observable for inverse methods applied to Slessor Glacier study area.

2.3.2 Ice Shelf Basal Topography and Melt Rates

R-channels near the Slessor Glacier drainage outlet at the end of transient GlaDS model runs can be compared to features on the bottom of the floating Filchner Ice Shelf to determine locations of basal channels (Dow et al., 2018c; Indrigo et al., 2021). Surface elevation data is sourced from the Reference Elevation Model of Antarctica (REMA) (Howat et al., 2019) by amalgamating 15 tiles of 8 m-resolution data that cover the Filcher Ice Shelf in the WGS84/Polar Stereographic coordinate system reference to. However, these data are interpolated to a resolution of 25 m due to computational restrictions.

Basal topography of the floating Filchner Ice Shelf is approximated by assuming hydrostatic equilibrium and following the method proposed by van den Broeke et al. (2008):

$$B = h_{\mathrm{asl}} - H_i = h_{\mathrm{asl}} \left(1 - \frac{\rho_{sw}}{(\rho_{sw} - \rho_i)} \right) \tag{2.74}$$

where H_i is ice thickness, h_{asl} is the elevation of the floating ice shelf above sea level, $\rho_{sw} = 1023.6$ kg m^{-3} is the density of sea water, ρ_i is the density of glacier ice, and B is the basal elevation of the ice shelf. Equation 2.74 has neglected the contribution of firn, and while some areas near the grounding line contain blue ice (figure 2.11), there could be firn of varying thickness present over much of the Filchner Ice Shelf. This introduces a source of error into the calculation.
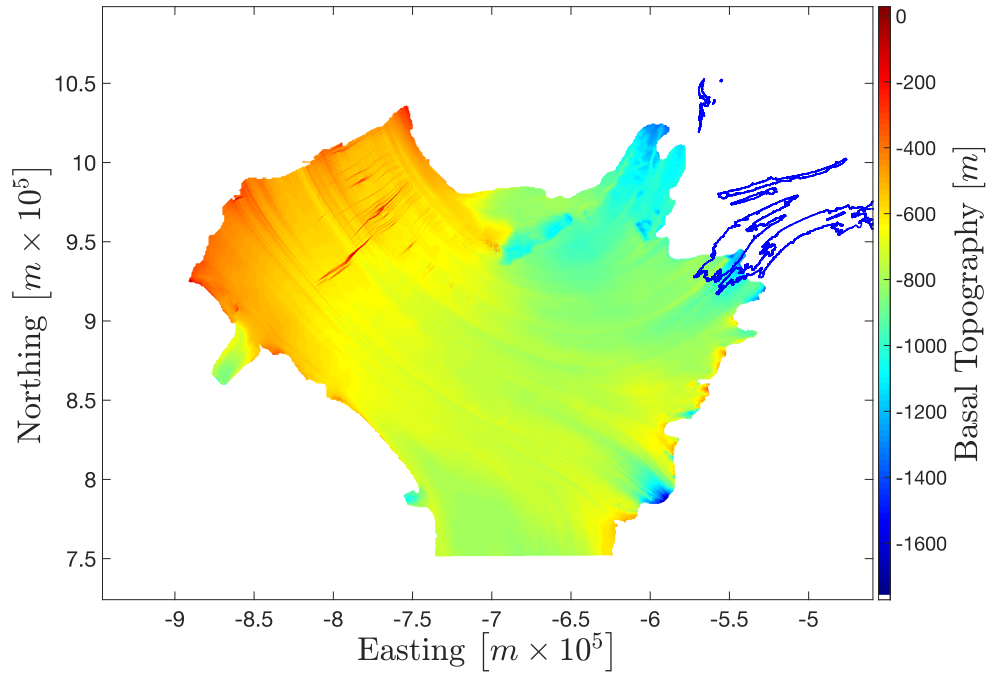
Figure 2.11: Filchner Ice Shelf basal elevation calculated from hydrostatic inversion. Blue polygons represent zones of blue ice from Hui et al. (2014). Ice shelf elevation is with respect to the height above sea level.

It is also useful to compare GlaDS subglacial channel locations and discharge rates at the Slessor Glacier and BIS drainage outlet to sub ice shelf melt rates to see how rates of discharge at the grounding line correspond to rates of ice shelf melt. To do so, ocean-driven basal melt rates at a resolution of 500 m from Adusumilli et al. (2020) are extracted for the Slessor Glacier/BIS outlet and Filchner Ice Shelf.

Chapter 3

Results

Model simulations were computed in order to compare and contrast outputs from the two-dimensional GlaDS subglacial hydrology model to those from ISSM ice dynamics model, as well as understand subglacial hydrology and ice dynamics processes in the Slessor Glacier study area. Comparing outputs from these two models can determine appropriate parameterizations for the GlaDS model. A suite of 48 transient hydrology model runs were computed with GlaDS to form a sensitivity test, and ISSM was used to infer ice rigidity over a floating ice shelf and the basal friction coefficient beneath grounded ice for three different friction laws. The GlaDS model was run independently of the ice dynamics model, and inversions using the Budd and Schoof friction laws were driven using effective pressure outputs from GlaDS. The remainder of this chapter will be a presentation of sensitivity test results, followed by the inverse method results, and lastly, a brief discussion of general results from each model.

3.1   Sensitivity Test Results

The nomenclature and details of each GlaDS model run presented in this chapter are given below in table 3.1.

The results from the base runs, i.e., those that use both spatially variable basal velocity and water input will be presented first, followed by the runs that use a constant water input or basal velocity. The base runs are likely to represent reality more accurately, and so their results will simply be presented as they are, and to assess the impact of using constant water input or basal velocity, the results from those model outputs will be presented as a comparison to the base runs. Channel conductivity did not have a significant effect on the results of comparing base runs to those that used either a constant water input or basal velocity, and so the relevant model runs (wiH, wiL, bvH, and bvL in table 3.1) with $k_c = 5 \times 10^{-2}$ m$^{7/4}$kg$^{-1/2}$ are compared to brHM and brLM to show the effects of using either a constant water input or basal velocity. The remainder of model runs performed in the sensitivity test will be used to analyze channel discharge and ice shelf melt rates near the grounding line in chapter 4.

Table 3.1: Table of names and parameters used in the sensitivity test. Base runs have names of the form brXY, where br stands for base run and X is H for the highest value of sheet conductivity and L for the lowest, similarly, Y is H for the highest value of channel conductivity, M for the middle value and L for the lowest value. Model runs using a constant water input have names of the form wiX, where X is H for a high sheet conductivity and L for a low sheet conductivity, and model runs with a constant basal velocity follow the same naming scheme as model runs with a constant water input. SV stands for spatially variable, and linear ramp-up refers to the scheme described in section 2.1.8.

Model Run Name	$k_s \left[\mathrm{m}^{7/4}\mathrm{kg}^{-1/2}\right]$	$k_c \left[\mathrm{m}^{7/4}\mathrm{kg}^{-1/2}\right]$	Water Input	Basal Velocity
brHM	10^{-3}	5×10^{-2}	SV	SV
brHL	10^{-3}	10^{-3}	SV	SV
brHH	10^{-3}	10^{-1}	SV	SV
brLM	10^{-4}	5×10^{-2}	SV	SV
brLL	10^{-4}	10^{-3}	SV	SV
brLH	10^{-4}	10^{-1}	SV	SV
wiH	10^{-3}	5×10^{-2}	linear ramp-up	SV
wiL	10^{-4}	5×10^{-2}	linear ramp-up	SV
bvH	10^{-3}	5×10^{-2}	SV	50 m/year
bvL	10^{-4}	5×10^{-2}	SV	50 m/year

3.1.1   Varying Sheet and Channel Conductivity

Model outputs for the base runs show that in all runs, water is present beneath ice at the three tributaries, the outlets of BIS and Slessor Glacier, and deep water is present at the DDT area. Subglacial water will be presented graphically as the one-dimensional water sheet thickness in meters as it is calculated in the GlaDS model, but will be discussed as a volume calculated by multiplying the one-dimensional water sheet thickness [m] at each node by the area associated with those nodes [m^2].
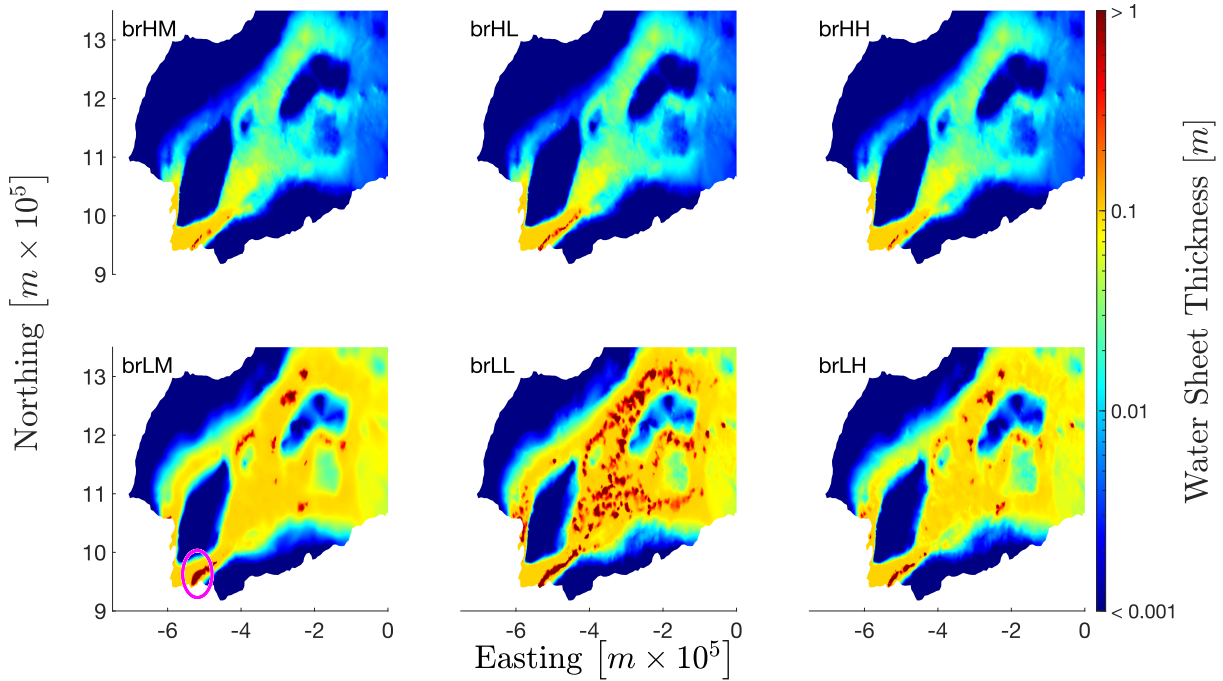
Figure 3.1: Log plot of water thickness [m] at the end of base runs with spatially variable water input and basal velocity. Inset titles in each subfigure correspond to parameterizations as in table 3.1. Magenta circle in subfigure brLM shows deep water in DDT area. The colour bar is capped to highlight where water is deep and shallow.

The maximum volume of water at the end of each base run ranged from 70.7×10^6 m^3 for brHH, up to 1.1×10^9 m^3 for brLL. The mean and sum total volume of water is calculated across all nodes to investigate how much water was present when the model finished after $20,000$ days. The lowest total water volume across the entire domain was 3.1×10^9 m^3 which corresponded to a mean volume of 1.5×10^5 m^3 for brHH, and the largest volume of water across the domain was 4.4×10^{10} m^3 with a mean volume of 2.2×10^6 m^3 for brLL. A summary of water volume statistics can be found at table 3.2.

Water sheet thickness is assessed at the DDT area by examining nodes near the grounding line with a bed elevation less than -1500 m above sea level. The mean volume in the DDT area ranges from being approximately $4 - 11$ times greater than that of the entire domain at the end of each base run, and stores approximately $5 - 13\%$ of the total water. At the end of each base run, the majority of the domain was in SS except for localized areas where the change in water sheet thickness between the final two time steps was to the order of 10^{-3} m, mainly near the DDT area, but excepting brLL where nodes measuring a difference of $> 10^{-3}$ m were widespread across the entire domain.

Table 3.2: Statistics for water volume at end of base runs. Run names have the same parameters as those in table 3.1.

Run	Maximum Volume of All Nodes $[m^3 \times 10^6]$	Total Volume Across Entire Domain $[m^3 \times 10^9]$	Mean Volume Across Entire Domain $[m^3 \times 10^6]$
brHM	75.5	3.1	0.2
brHL	78.4	3.4	0.2
brHH	70.7	3.1	0.2
brLM	157.5	20.1	1.0
brLL	1135.2	44.0	2.2
brLH	321.8	19.4	1.0

Table 3.3: Statistics for water volume at the DDT area at the end of the base runs. Run names have the same parameters as those in table 3.1.

Run	Maximum Volume at DDT Area $[m^3 \times 10^6]$	Mean Volume at DDT Area $[m^3 \times 10^6]$	Total Volume at DDT Area $[m^3 \times 10^9]$	% of Total Volume at DDT Area
brHM	75.5	1.5	0.4	11.62
brHL	78.4	1.9	0.5	13.23
brHH	70.7	1.5	0.3	11.20
brLM	73.6	6.9	1.6	8.10
brLL	151.3	8.8	2.1	4.70
brLH	136.0	5.3	1.3	6.44

Effective pressure is low for the majority of the domain at the end of each base run, however, at the Touchdown Hills, Theron Mountains, and Shackleton Range, high effective pressures persist as subglacial water pressure stays low in these areas, though the extent of this trend is lessened for base runs with a lower sheet conductivity. Mean effective pressures are higher for base runs brHM, brHL and brHH which use a higher sheet conductivity, with the highest mean effective pressure being 3.0 MPa for both brHM and brHH. Base runs brLM, brLL and brLH had lower mean effective pressures, with the lowest being 1.2 MPa for brLL. Negative effective pressures are present at the end of several of the base runs, typically within the DDT, but also up-glacier for brLL, where both the channel and sheet conductivity are at the lowest tested values. Effective pressure in the DDT area is lower

on average, and equal to ~ 0.5 MPa for brHM, brHL and brHH, and ~ 0.3 MPa for brLM, brLL and brLH, which is consistent with the high volume of water in this area.

The flotation fraction, p_w/p_i, for all of the base runs tends to be ≥ 0.80. The lowest mean flotation fraction was 0.79 for brHH, and the highest mean flotation fraction was 0.88 for both brLM and brLL (figure 3.2). Multiple runs had areas where the flotation fraction was greater than 1, which corresponds to negative effective pressure. In the DDT area, all mean flotation fractions are greater than 0.95, and each base run with a sheet conductivity of 10^{-4} $m^{7/4}kg^{-1/2}$ had flotation fractions greater than 1. Summaries of pressure statistics are given in tables 3.4 and 3.5
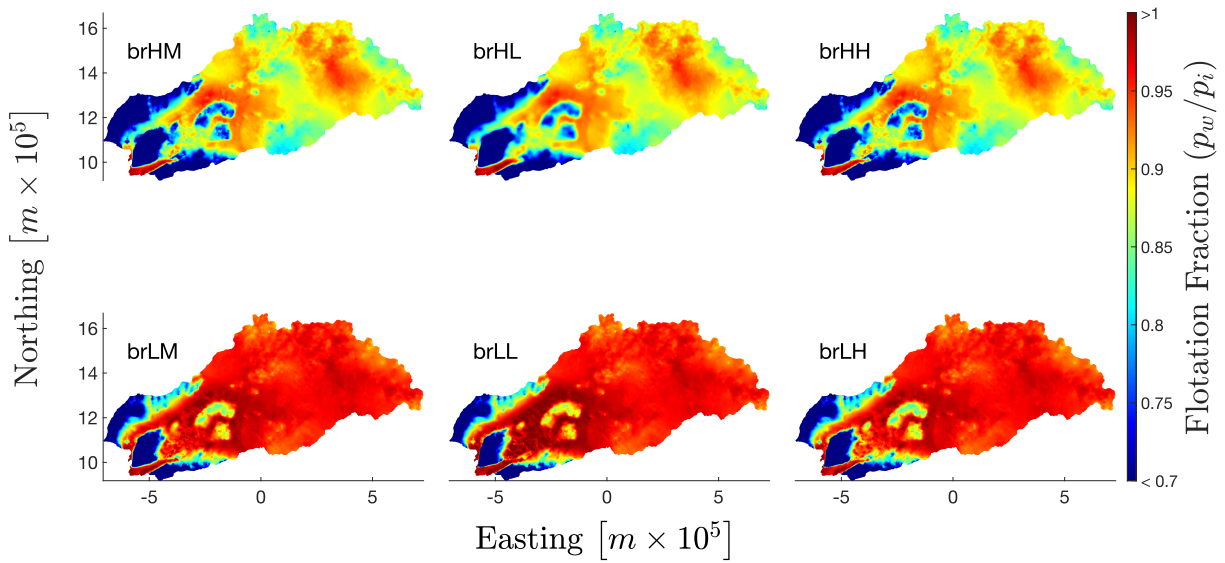
Figure 3.2: Flotation fraction at the end of base runs with spatially variable water input and basal velocity. Colour bar is capped to highlight areas of low flotation fraction/high effective pressure. Run names have the same parameters as those in figure 3.1.

Table 3.4: Statistics for subglacial water pressure at the end of base runs. Run names have the same parameters as those in table 3.1.

Run	Minimum effective pressure $[Pa \times 10^3]$	Mean effective pressure $[Pa \times 10^6]$	Mean flotation fraction	Maximum flotation fraction
brHM	19.6	2.9	0.79	1.00
brHL	-63.6	2.9	0.80	1.00
brHH	19.6	3.0	0.79	1.00
brLM	-219.2	1.3	0.88	1.01
brLL	-3577.8	1.2	0.88	1.04
brLH	-102.7	1.4	0.87	1.01

Table 3.5: Statistics for water in the DDT at the end of the base runs. Run names have the same parameters as those in table 3.1

Run	Minimum effective pressure $[Pa \times 10^3]$	Mean effective pressure $[Pa \times 10^6]$	Mean flotation fraction	Maximum flotation fraction
brHM	80.8	0.6	0.95	0.99
brHL	-63.6	0.5	0.96	0.99
brHH	72.4	0.6	0.95	1.00
brLM	-108.0	0.4	0.97	1.01
brLL	-160.6	0.2	0.98	1.01
brLH	-96.5	0.4	0.97	1.01

Channel discharge is presented here as the discharge of channels flowing out of the nodes, and nodes discharging less than $Q_0 = 0.1$ m^{3}s^{-1} are not considered as hosting significant channel discharge. At the end of each base run, the maximum discharge is found in the DDT area, excepting brLH, where the largest discharge occurs at the BIS outlet. Channel discharge was localized to the Slessor Glacier outlet and the DDT area for the base runs with a sheet conductivity of 10^{-3} m$^{7/4}$kg$^{-1/2}$, but reaches further up-glacier to each of the three tributaries for base runs with a sheet conductivity of 10^{-4} m$^{7/4}$kg$^{-1/2}$, with the exception of brLL where discharge $> Q_0$ did not persist beyond the DDT area. Maximum discharge at the end of each base run increases when either channel conductivity is increased or sheet conductivity is decreased, and decreases when the opposite is applied. This resulted in brLH having the highest maximum channel discharge of 40.47 m^{3}s^{-1}, and

brHL having the lowest maximum channel discharge of 7.30 m³s⁻¹, where both values are calculated at the final time step. These trends are also consistent with the number of nodes discharging $Q > Q_0$, where there were 47 nodes at the end of brHL, and 1000 at the end of brLH. A summary of channel discharge statistics is presented in table 3.6.
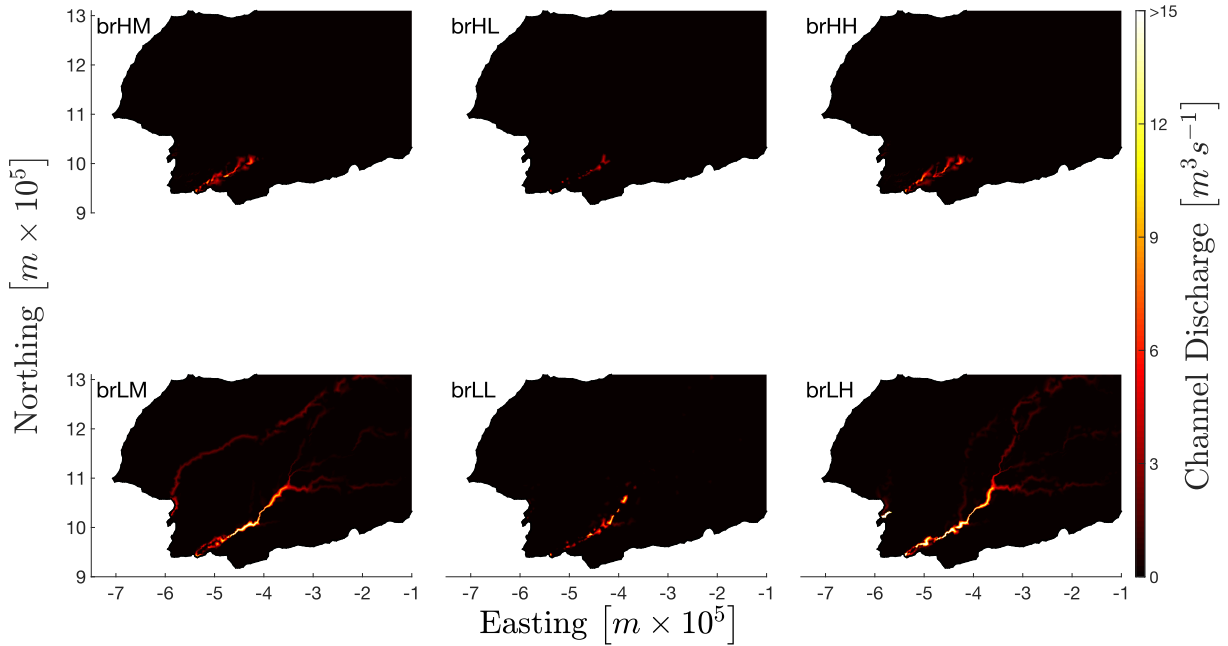
Figure 3.3: Channel discharge [m³s⁻¹] at the end of base runs with spatially variable water input and basal velocity. Colour bar is capped to highlight where channel discharge is higher. Run names have the same parameters as those specified in table 3.1

Table 3.6: Statistics for channel discharge at the end of the base runs. Run names have the same parameters as those in table 3.1. $Q_0 = 0.1$ m³s⁻¹.

Run	Number of nodes with $Q \geq Q_0$	Maximum discharge [m³s⁻¹]	Mean discharge [m³s⁻¹]
brHM	274	12.3	1.9
brHL	47	7.3	2.3
brHH	335	11.3	1.6
brLM	780	18.9	1.9
brLL	176	15.6	2.6
brLH	1000	40.7	2.2

A channel network forms in all models runs from the grounding line to the end of the DDT area, but extends further up-glacier to the three tributaries when sheet conductivity is set to 10^{-4} $\text{m}^{7/4}\text{kg}^{-1/2}$ (figure 3.4).
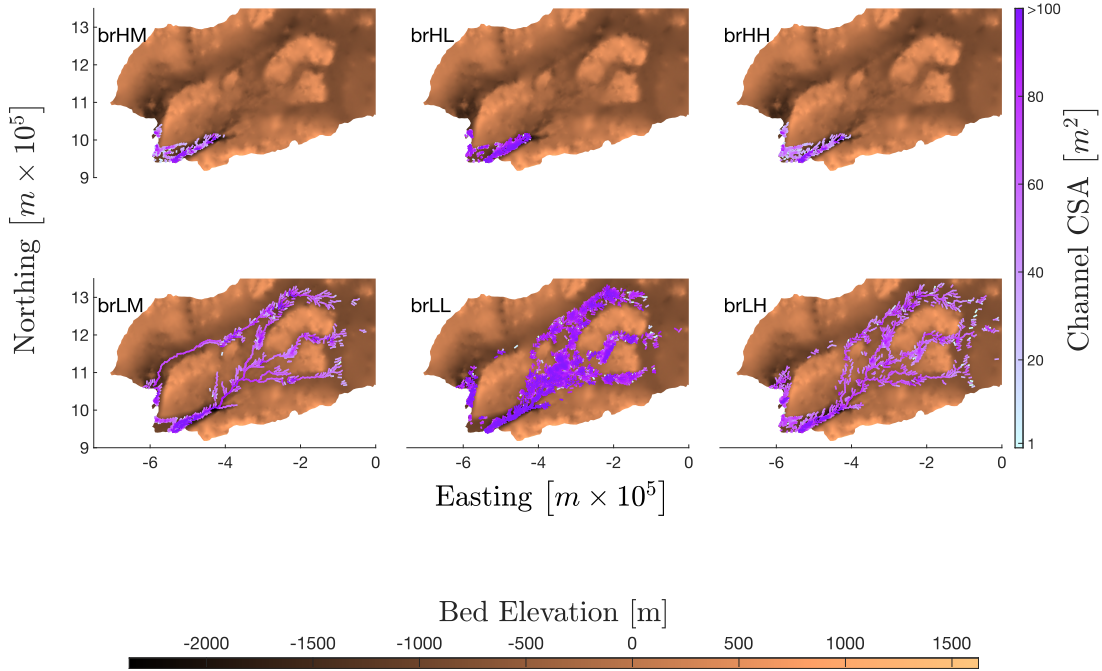
Figure 3.4: Channel CSA [m²] at the end of base runs with spatially variable water input and basal velocity. Colour bar is capped to show where small channels form. Run names have the same parameters as those specified in table 3.1. Bed elevation is in meters with respect to height above sea level.

To ensure model stability, channel cross-sectional area (CSA) is allowed to grow no bigger than 500 m², which corresponds to a radius of approximately 18 m for a semicircular channel at the base of the glacier. All model runs had multiple channels form that were maximal at this value, especially near the grounding line and DDT area. The number of channels, mean channel CSA, median channel CSA, and total length of channels are calculated for each run, however, channels with a cross sectional area less than 0.015 m², or a radius smaller than $\sim$ 10 cm are not considered (table 3.7). It is worth noting that the smaller mean and median channel CSAs do not imply a less extensive channel network, but actually the opposite. They have smaller values due to the large increase of relatively smaller channels forming.

Table 3.7: Statistics for channel CSA at the end of base runs. Run names have same parameters as those in table 3.1.

Run	Number of edges with channels	Mean channel CSA $[m^2]$	Median channel CSA $[m^2]$	Total length of channels $[m \times 10^5]$
brHM	405	62.6	10.3	11.6
brHL	531	30.5	0.1	16.6
brHH	452	56.2	8.2	13.0
brLM	1378	18.1	1.3	60.2
brLL	3212	12.9	0.1	140.1
brLH	1696	28.1	1.1	73.1

Channels mainly form in the GlaDS model where surface gradients are steepest, and this is reflected by the abundance of channels that form near the DDT area, where there is both a decrease in bed and surface elevation. The largest difference between the number and extent of channels is observed when sheet conductivity is altered, as opposed to channel conductivity, and so the channel system is more sensitive to sheet conductivity. This makes sense as increasing the sheet conductivity will cause the water sheet to conduct water more efficiently, and so fewer channels form. This is why in brHM, brHL and brHH, channels are localized to the DDT area, and in base runs brLM, brLL and brLH, channels persist up to the tributaries. Moreover, decreasing the sheet conductivity also caused the channel system to become more arborescent.

The channel system is less sensitive to channel conductivity, but there are some key features observed when channel conductivity is altered. Decreasing channel conductivity caused the channel network to shift slightly downstream, e.g., for brHH, the channels start forming approximately 18km further upstream than those in base run brHL, which has the lowest channel conductivity (figure 3.4, subfigures brHH and brLM). Decreasing channel conductivity also increases the arborescence of the channel network, which Werder et al. (2013) conjecture is due to the lower effective pressures reducing the effect of creep closure and allowing more channels to persist.

Water pressure does not reach overburden in the base runs at the Shackleton Range, Theron Mountains and Touchdown hills as a consequence of several different factors. The BIS and Slessor Glacier outlets are downstream of a very large catchment, which creates a bottleneck effect and all the water ends up draining here, and moreover, surface slopes in this area are steep (e.g., surface elevation changes from ~ 1500 m to ~ 150 m over 70 km between the Shackleton Range and the DDT area), which both lead to large rates of channelization (figure 3.5, subgfigure brHM). This in turn leads to the negligible amount of melt from the ISMIP6 data set in the Touchdown Hills, Theron Mountains and Shackleton Range areas (figure 3.5, subfigure brHH) draining into the efficient system at either the

DDT area or BIS outlet, and so water pressure cannot reach overburden. Steep changes in bed topography can also be difficult for the model to represent well, and the Shackleton Range and Theron Mountains have peak elevations of ~ 1200 m and ~ 900 m that quickly drop down to -2300 m and -1526 m in the DDT are and BIS outlet respectively. The ice thickness in this area is often set to the minimum imposed value of ice thickness, 100 m, and in reality, these areas contain exposed bedrock which is not contributing to the subglacial hydrological network.
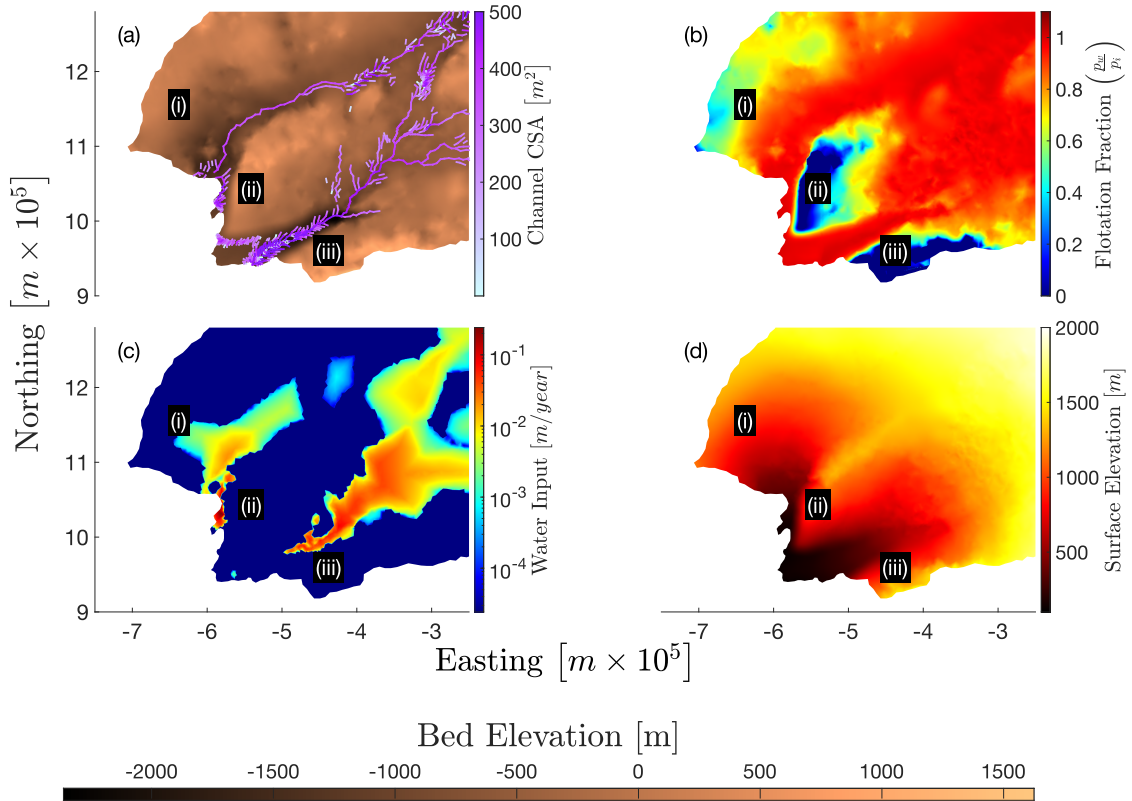
Figure 3.5: Several parameters related to the low flotation fraction at the Touchdown Hills (i), Theron Mountains (ii) and Shackleton Range (iii): (a) bed elevation with overlain channel CSA, (b) flotation fraction, (c) log plot of melt data and (d) surface elevation. Surface and bed elevation are in meters with respect to height above sea level.

3.1.2 Varying Water Input and Basal Velocity

Model runs with either a constant water input or basal velocity (wiH, wiL, bvH and bvL) will be compared to brHM and brLM to assess the impact of these parameters when they are constant versus when they are spatially variable. All parameter values for wiH, wiL, bvH and bvL can be found in table 3.1.
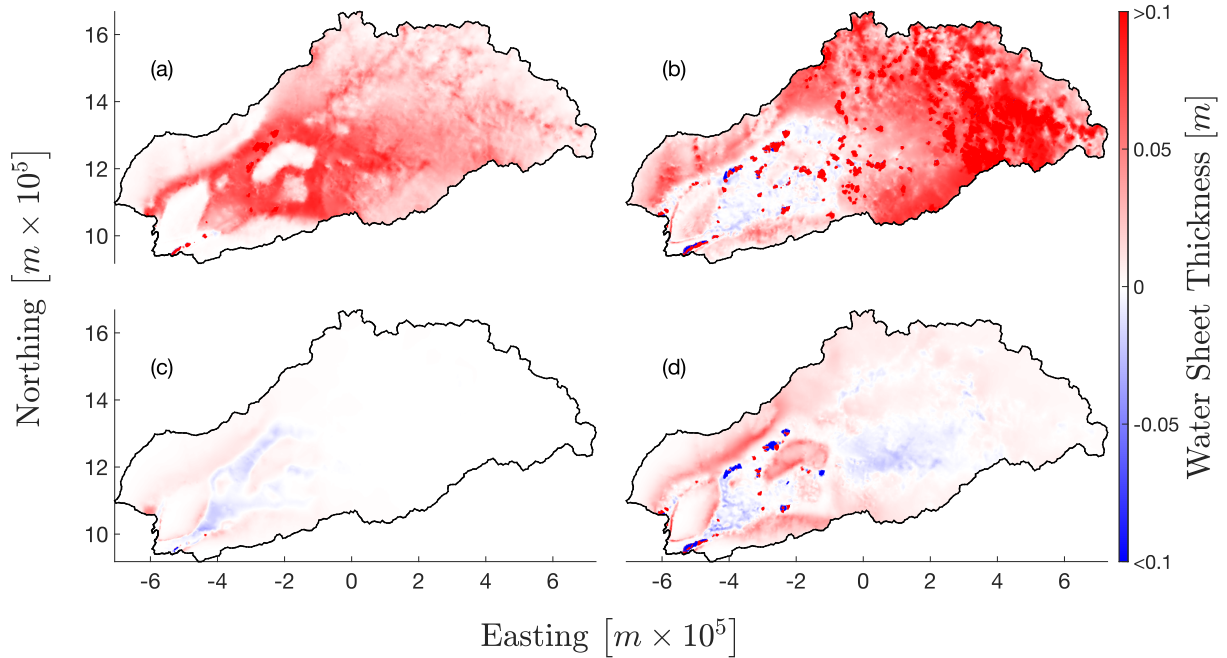
Figure 3.6: Water sheet thickness difference plots between synthetic and spatially variable water input or basal velocity at end of model runs: (a) wiH - brHM, (b) wiL - brLM, (c) bvH - brHM and (d) bvL - brLM. Colour bar capped to ±0.1 m to highlight areas where differences are small.

The results for subglacial water for the constant water input and basal velocity runs will be presented as volumes, however, the differences between the two will be presented as the difference in the one dimensional water sheet thickness.

Water volume was in general more significantly affected by the constant water input than it was the constant basal velocity. Across all nodes at the end of model run wiH, there was a maximum volume of 144.6×10^6 m^3, a total volume of 20.7×10^9 m^3, and a mean volume of 1.0×10^6 m^3. For the end of model run wiL, these statistics were 686.8×10^6 m^3, 71.3×10^9 m^3 and 3.5×10^6 m^3, respectively. There is less water in the base runs than constant water input runs over the majority of the domain, but at the grounding line and in the DDT area, there are several areas where there is more water in the base runs, and for brLM, this trend extends up-glacier to the tributaries, ending at approximately -1×10^5 m easting (figure 3.6). Across all nodes, the difference plots have a maximum and minimum water sheet thickness of ±0.1 m as the majority of values in the difference are small, however, it is worth noting that there are areas where there are larger differences in each comparison. The largest difference between brHM and wiH was 8.71 m, and the largest difference between brLM and wiL was 21.86 m, and for both runs, areas of large difference are localized. Model run wiL did not reach steady state, and between the final two time steps there were many areas where the difference between water sheet thickness between the nodes was to the order of 10^{-2} m.

67

There was not an appreciable difference in water thickness between the base runs and the constant basal velocity runs (figure 3.6, subplots (c) and (d)). The maximum, cumulative and mean volume at the end of bvH were 73.0×10^6 m^3, 3.7×10^9 m^3 and 0.2×10^6 m^3, respectively, and for bvL, these values were 277.0×10^6 m^3, 23.7×10^9 m^3 and 1.2×10^6 m^3, respectively. These values are similar to the results from brHM and brLM (table 3.2). The maximum difference between brHM and bvH was 0.6 m, and the maximum difference between brLM and bvL was 11.9 m. There is a high degree of spatial variability between where the base runs have higher water sheet thickness, and where the fixed velocity runs have a higher water sheet thickness. Dow et al. (2020) highlight that this is due to an influence on water drainage imposed by the topography. Water thickness in the base runs is higher downstream where there is lower basal topography and, because the basal velocity is also high in these areas (figure 2.2), the cavity opening rate increases which leads to more water being forced into the areas of high flux, which in turn lowers the water sheet thickness and the water pressure as water is removed too fast to pressurize. In the fixed basal velocity runs, the upland regions and areas of locally high topography have a higher cavity opening rate due to the uniform basal velocity, but they are not as well-connected with the efficient drainage system near the grounding line. This results in water pooling in these areas where there is very little water in the base run (e.g., to the order of 10^{-3} m).
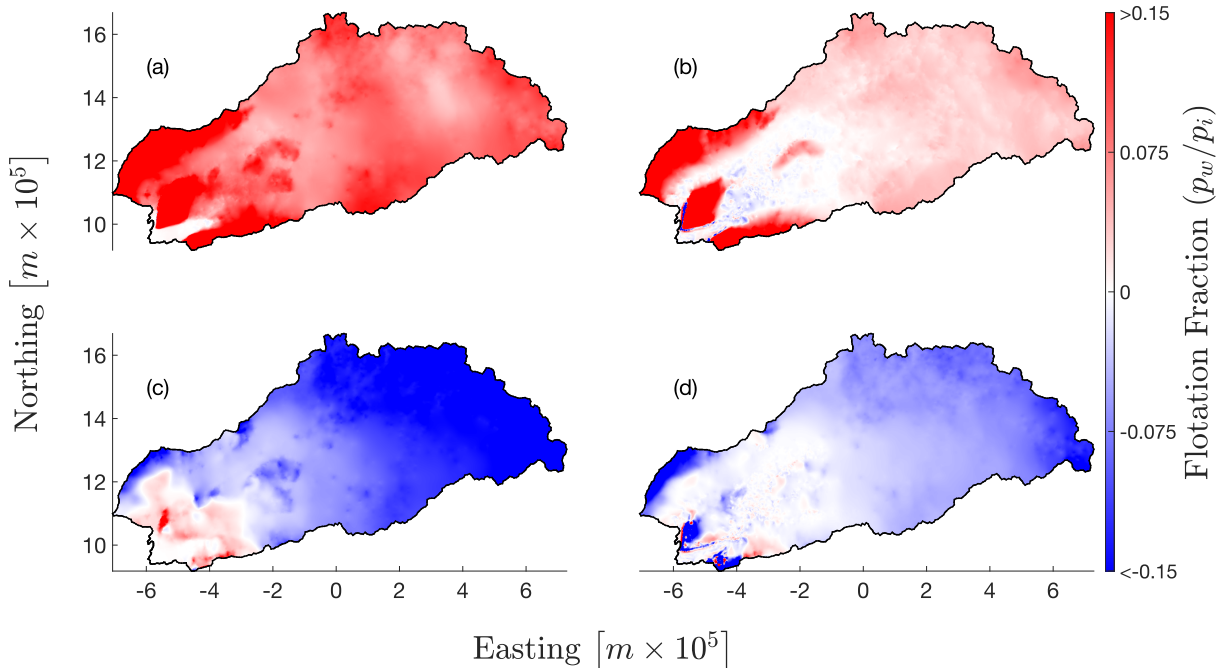
Figure 3.7: Flotation fraction difference plots between synthetic and spatially variable water input or basal velocity at the end of model runs: (a) wiH - brHM, (b) wiL - brLM, (c) bvH - brHM and (d) bvL - brLM. Colour bar limits are set to ± 0.15 to highlight where differences are small.

The trends in subglacial water pressure for the constant water input runs are consistent

with water sheet thickness. The mean effective pressure, flotation fraction and percent of the domain with flotation fraction above 0.80 for wiH was 1.0 MPa, 0.92, and 92% respectively, and for wiL, these statistics were 0.6 MPa, 0.95 and 96%, respectively. The pressure is higher in model runs wiH and wiL for the majority of the domain, but near the grounding line and DDT area, the pressure is slightly higher in the base runs (figure 3.7). The difference in water thickness and water pressure between the constant water input runs and the base runs is due mainly to the difference between a water input of 5 mm/year and the water input from the spatially variable data. Up-glacier, and at areas of locally high basal elevation, the spatially variable water input is ≈ 0, whereas in the constant water input runs, there is now a water input that is significantly higher, often by an order of magnitude (figure 2.2).

Water pressure is lower in the constant basal velocity runs for nearly the entire domain, except for the area surrounding the outlets, where water pressure is lower in the base runs (figure 3.7, subfigures (c) and (d)). The variation in pressure for the majority of the domain is a consequence of the difference in velocity between the spatially variable data set, and a fixed rate of 50 m/year. Up-glacier, basal velocity in the base runs is low, and often times near zero, which reduces the rate of cavity opening (equation 2.4). Alternatively, when a basal velocity of 50 m/year is applied up-glacier, where velocity is near zero for the base runs, cavities open which depressurize the system. Near the grounding line, the opposite is true; basal velocities are higher than 50 m/year (often by one or two orders of magnitude) and water becomes more pressurized due to the comparatively lower rate of cavity opening in the fixed basal velocity runs than the base runs. Interestingly, the water pressure is higher in brLM than bvL in the Theron Mountains and Shackleton Range areas, but lower in brHM than it is for bvH in the same areas, despite no significant difference in water sheet thickness (figure 3.6, subfigures (c) and (d)). This implies that the sheet conductivity, a poorly constrained parameter, is playing a significant role in pressurizing areas of locally high basal elevation surrounding the overdeepenings at the BIS and Slessor Glacier outlets.
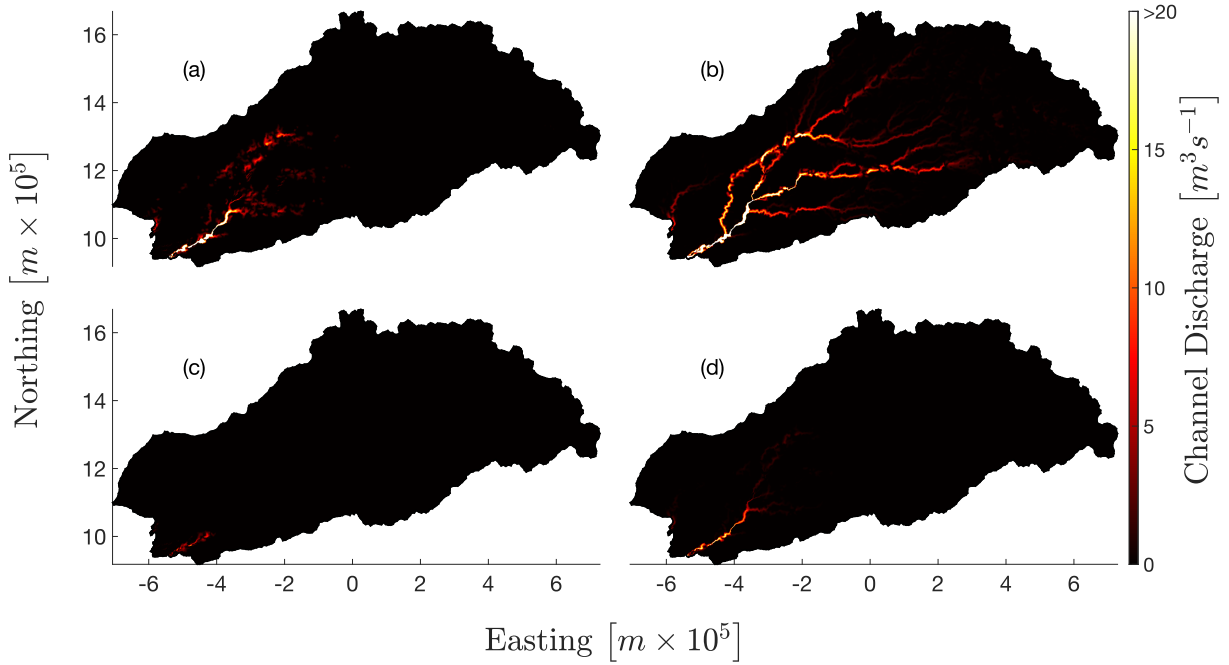
Figure 3.8: Channel discharge at end of model runs with constant water input and basal velocity: (a) wiH, (b) bvH, (c) wiL and (d) bvL. Colour bar limits are set to ± 20 m^{3}s^{-1} to show low discharge in (iii).

The large flux of water passing through the DDT area and BIS towards the grounding line creates an efficient system of R-channels for wiH and wiL, and this is why there is more water and higher effective pressure in this area for the base runs (figure 3.9). At the end of model run wiH, there are 1093 nodes with a discharge $Q > Q_0$, and a maximum discharge of 74.45 m^{3}s^{-1}, and for model run wiL, these numbers are 4138 and 96.43 m^{3}s^{-1}, respectively. Using the constant water input had a similar impact on the spatial extent of channel discharge as lowering the sheet conductivity. In base runs with a sheet conductivity of 10^{-3} m$^{7/4}$kg$^{-1/2}$, channel discharge was localized to the DDT area, but when a constant water input is used, channel discharge extends to the tributaries. Similarly, for the base runs with a sheet conductivity of 10^{-4} m$^{7/4}$kg$^{-1/2}$, channel discharge reached the tributaries, but with a constant water input, channel discharge reaches further up-glacier, to approximately 4×10^5 m easting (figure 3.8). Channel CSA follows the same pattern as channel discharge in terms of spatial extent when using the constant water input. At the end of wiH, there are 1633 channels with CSA greater than 0.015 m^2, a mean channel CSA of 44.4 m^2, a median channel CSA of 6.9 m^2, and a total length of channels of 64.1×10^5 m and for wiL, these statistics are 8914, 15.8 m^2, 0.9 m^2, and 477.8×10^5 m respectively.

There is not a significant difference in channel discharge and CSA between the base runs and model runs bvH and bvL. At the end of the model runs, the number of nodes with discharge $Q > Q_0$ and maximum discharge for bvH were 295 and 12.39 m^{3}s respectively,

70

and for bvL, these statistics were 837 and 22.61 m^{3}s^{-1} respectively. At the end of bvH, there were 459 channels, a mean channel CSA of 60.9 m^2, a median channel CSA of 8.2 m^2, and a total length of channels of 12.6 $\times 10^5$ m. For bvL, these statistics are 1508, 30.0 m^2, 1.6 m^2, and 60.1 m $\times 10^5$.
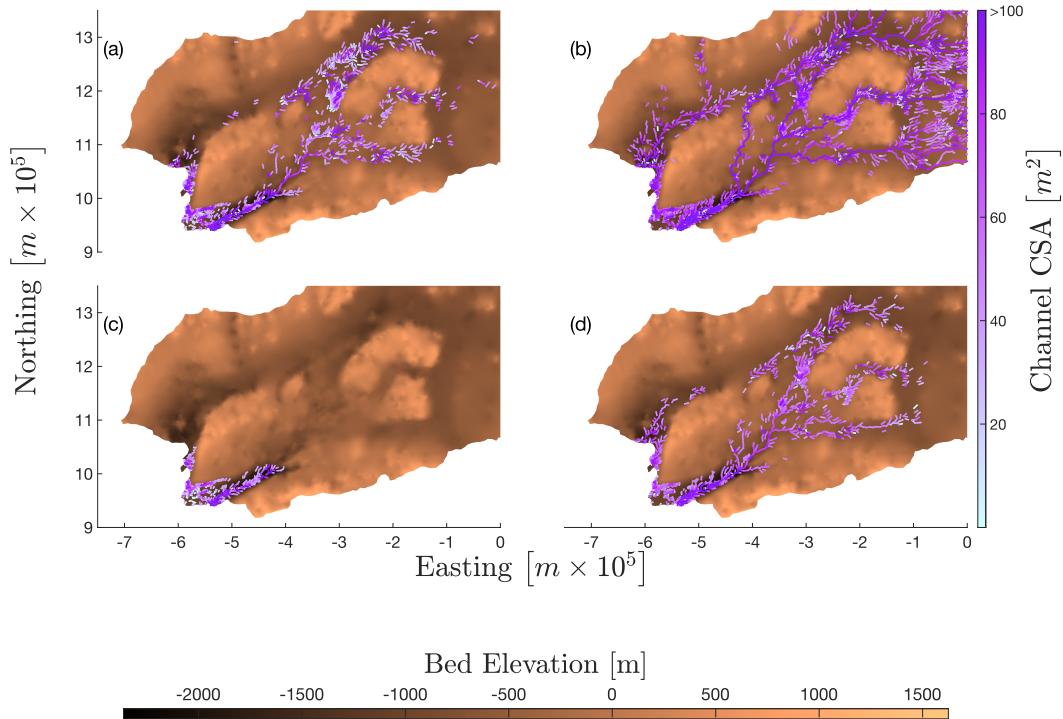
Figure 3.9: Channel CSA at the end of model runs with constant water input and basal velocity: (i) wiH, (ii) wiL, (iii) bvH and (iv) bvL. Colour bar is capped at 100 m^2 to show range of channels with smaller channel CSA. Actual maximum channel CSA is 500 m^2. Bed elevation is in meters with respect to height above sea level.

3.2 Ice Dynamics Results

3.2.1 Ice Rigidity

One ice rigidity inversion and 13 friction inversions were calculated using the M1QN3 inversion software within ISSM, as well as stress balance simulations for each inversion. Inverting for ice rigidity over the floating ice shelf was completed first, followed by the subsequent friction inversions. Cost function coefficients γ_{101} and γ_{103} for the first two terms of the total cost function (2.67) for the ice rigidity inversion were set to

$$\gamma_{101} = 70 \tag{3.1}$$

and

$$\gamma_{103} = 1, \tag{3.2}$$

and an appropriate value for the Tikhonov regularization parameter was inferred from an L-curve analysis (figure 3.10), which was

$$\gamma_{502} = 4 \times 10^{-20}. \tag{3.3}$$
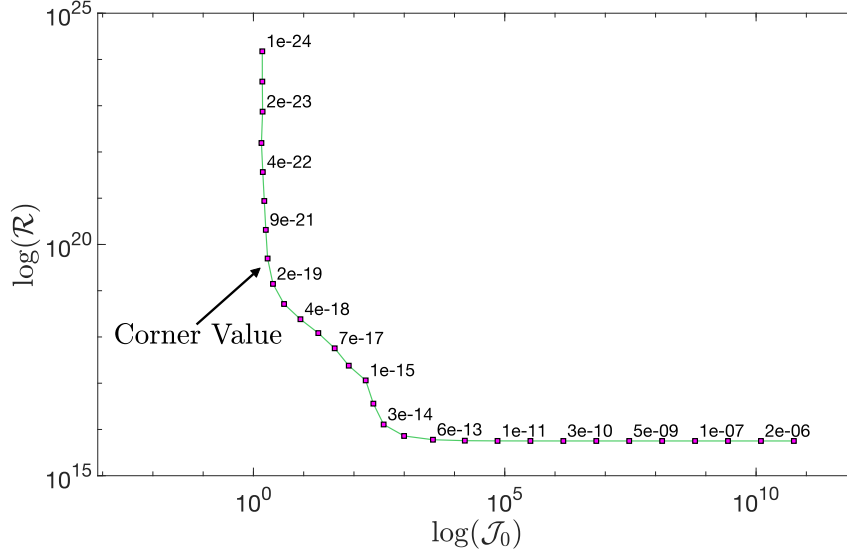
Figure 3.10: L-curve analysis results for 30 Tikhonov regularization coefficients when inverting for ice rigidity at the floating ice shelf. The values of the coefficients label the corresponding magenta marker.

The inversion infers the most rigid ice at the centre of the floating ice shelf, where the maximum rigidity is 6.23×10^8 $s^{1/3}Pa^{-1}$ which tapers off to lower rigidity at the margins (figure 3.11).
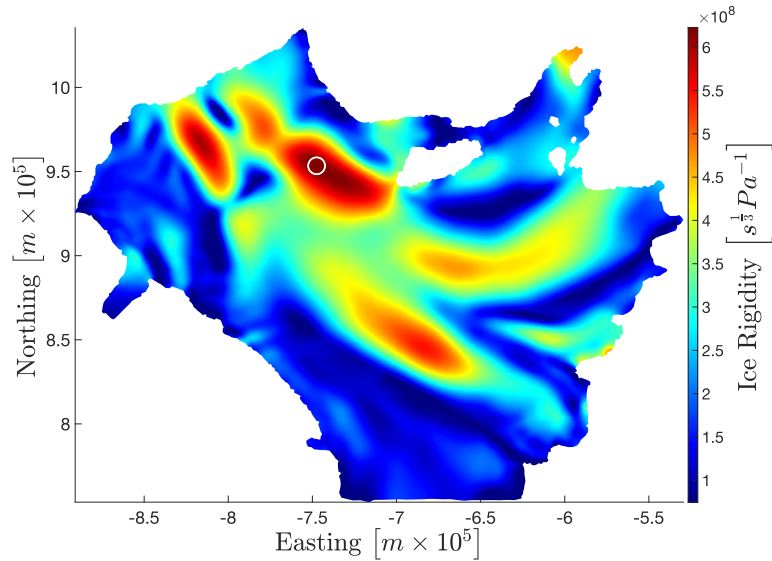
Figure 3.11: Modeled ice rigidity over floating ice shelf from inversion simulation in ISSM. White circle marks maximum calculated ice rigidity.

Misfit is calculated as the difference between the velocity field calculated from the stress-balance simulation and the observed velocities from the MeASUREs satellite observations (Mouginot et al., 2019). The mean misfit calculated for the ice shelf rigidity is 8.20 m/year, 99.8% of the nodes have an associated misfit less than 50 m/year, and the maximum misfit is 119.10 m/year (figure 3.12).
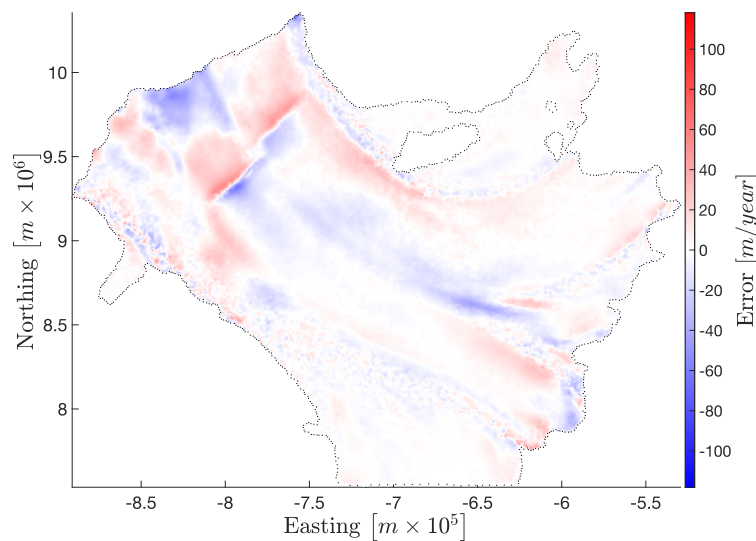
Figure 3.12: Error measured as difference between observed and modeled velocity for ice rigidity inversion over the floating ice shelf. Red corresponds to areas of larger observed velocity, and blue corresponds to areas of higher modeled velocity. Black dots show the domain boundary.

Ice rigidity is approximated for grounded ice using a relation based on surface temperature (Budd and Jacka, 1989). The modeled ice rigidity for the floating ice shelf together with the approximation over the grounded ice (figure 3.13) are used as a prior when inverting for the basal friction coefficient.
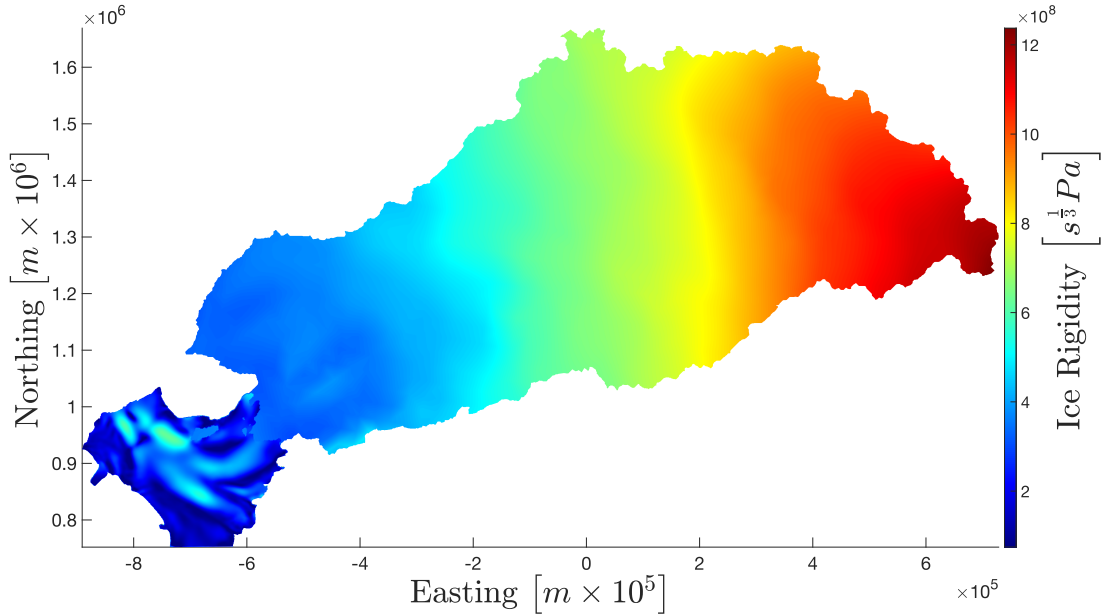
Figure 3.13: Ice rigidity field over the entire domain to be used as a prior for friction inversions.

3.2.2 Basal Friction

The procedure for selecting cost function coefficients γ_{101} and γ_{103} was described in section 2.2.2, and L-curve analyses are performed to select γ_{501} for the basal friction coefficient inversion simulations (figure 3.14).
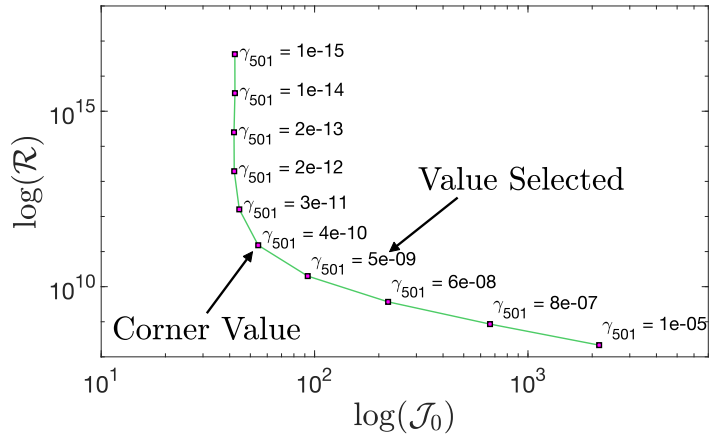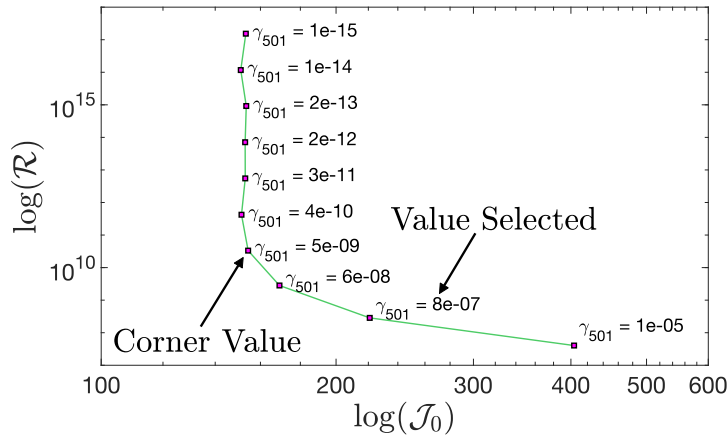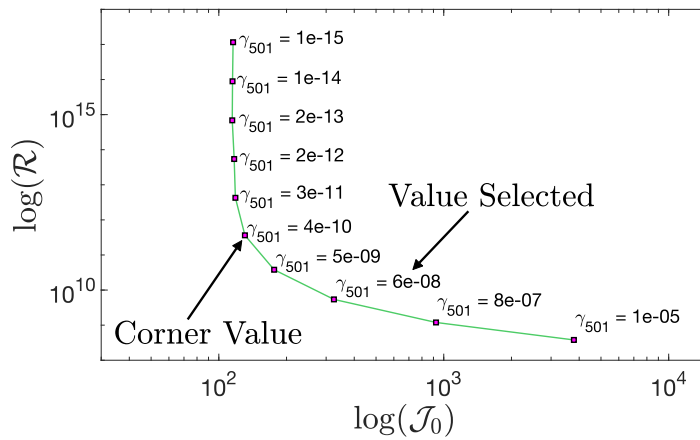
Figure 3.14: L-curve analyses results for 10 Tikhonov regularization coefficients when inverting for friction coefficients. (a) - Weertman friction law, (b) - Budd friction law and (c) - Schoof friction law. Effective pressure from brHL is the prior for (b) and (c).

The Weertman friction law (equation (2.38)) does not include effective pressure and only one L-curve analysis is required, but since the Budd and Schoof friction laws (equations (2.40) and (2.42), respectively) do depend on effective pressure, one L-curve analysis is required for each base run. Thus, a total of 13 L-curve analyses and inversion simulations were performed.

For each of the three inversions, the ideal Tikhonov regularization coefficients were those suggested by the corner of each plot, however, gradients still persisted in the solutions with these values, and to remedy this issue, higher Tikhonov regularization coefficients were selected. This could introduce an unwanted level of misfit to the stress balance solution, however, in this case there was no significant change by increasing the Tikhonov regularization terms by 1-2 orders of magnitude (figure 3.15). The values used for each of the cost function coefficients are summarized in table 3.8.
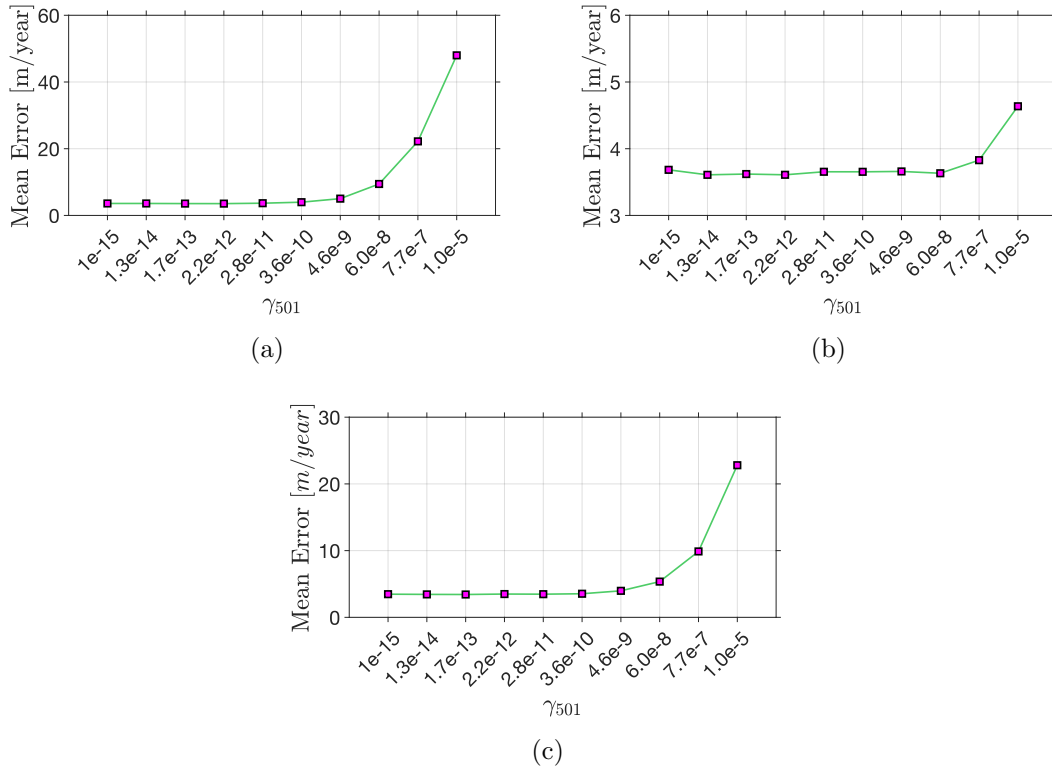
Figure 3.15: Mean error $[m/year]$ measured as absolute value of misfit between observed and simulated surface velocities for each tested Tikhonov regularization coefficient in the L-curve analyses: (a) Weertman friction law, (b) Budd friction law, (c) Schoof friction law.

Table 3.8: List of cost function coefficients used for basal friction coefficient inversion simulations. Effective pressure used as a prior for Budd and Schoof friction law inversions are denoted by the corresponding base run, taken from the final time step.

Friction Law	N	γ_{101}	γ_{103}	γ_{501}
Weertman	-	5×10^3	1	5×10^{-9}
Budd	brHM	10^4	1	8×10^{-7}
Budd	brHL	10^4	1	8×10^{-7}
Budd	brHH	10^4	1	8×10^{-7}
Budd	brLM	8×10^4	1	8×10^{-7}
Budd	brLL	8×10^4	1	8×10^{-7}
Budd	brLH	8×10^4	1	8×10^{-7}
Schoof	brHM	10^4	1	6×10^{-7}
Schoof	brHL	10^4	1	6×10^{-7}
Schoof	brHH	10^4	1	6×10^{-7}
Schoof	brLM	10^4	1	6×10^{-7}
Schoof	brLL	10^4	1	6×10^{-7}
Schoof	brLH	10^4	1	6×10^{-7}

Thirteen basal friction coefficient inversion simulations were performed, and the results suggest a lower friction coefficient in areas of fast observed flow (figures 3.16 and 3.17).
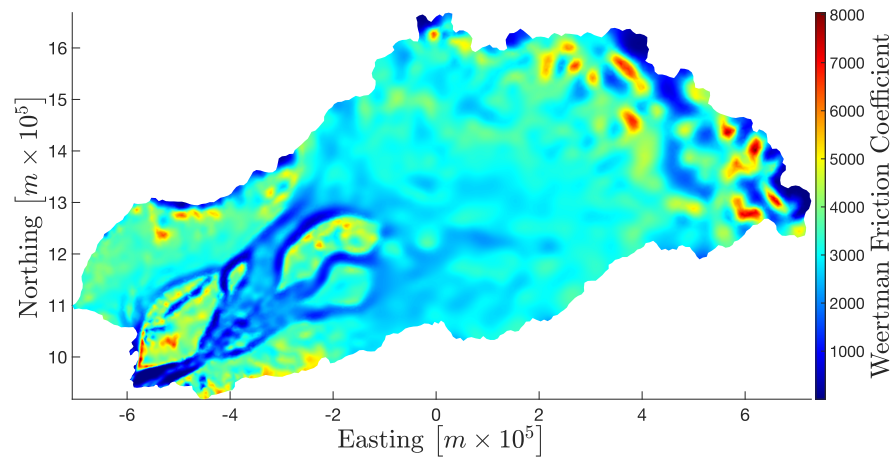
Figure 3.16: Inversion results for basal friction coefficient using the Weertman friction law. Domain is restricted to grounded ice.
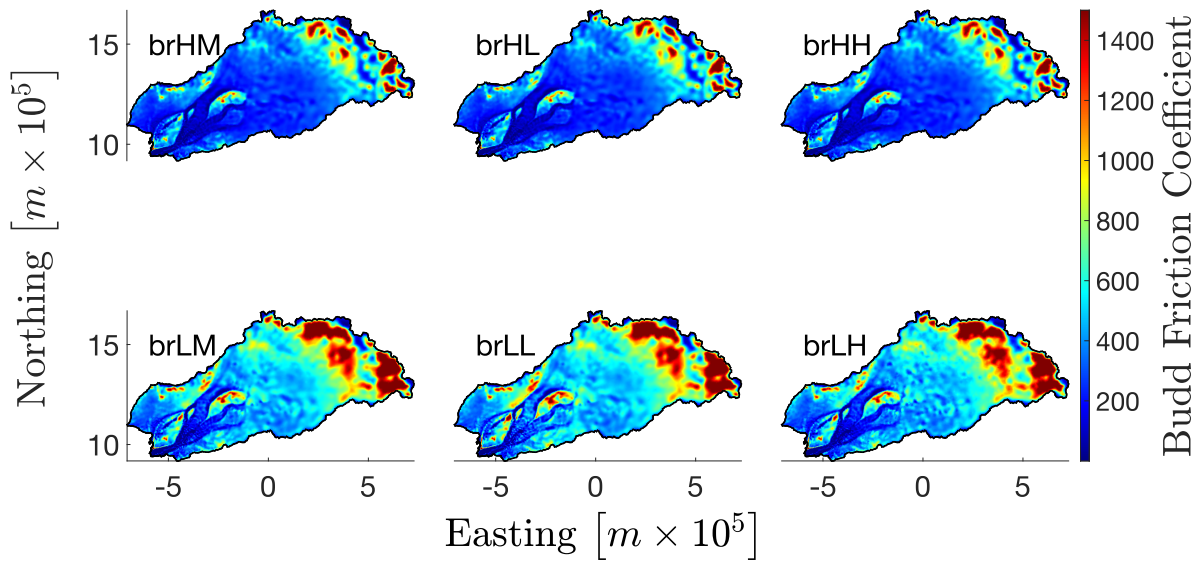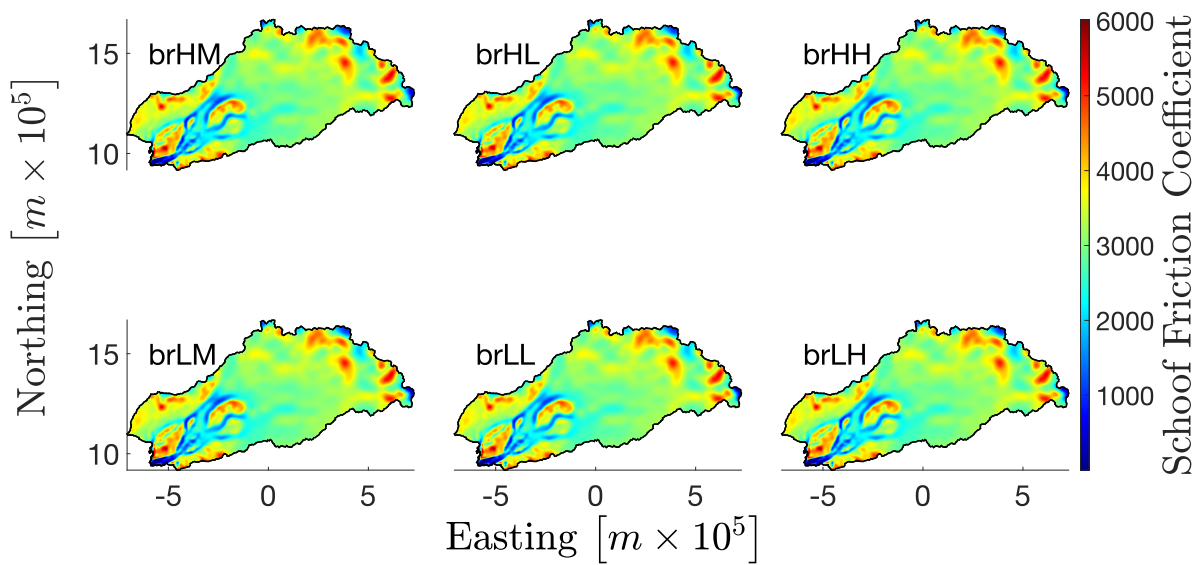
Figure 3.17: Inversion results for basal friction coefficient: (a) Budd friction law, (b) Schoof friction law. Inset labels describe which effective pressure output was used. Domain is restricted to grounded ice.

The range of values of each friction coefficient are not the same due to how each law is parameterized, however, areas of high and low friction coefficient can still be compared. In each inversion simulation, the friction coefficient is high at the Touchdown Hills, Theron Mountains, and Shackleton Range. These areas all have high basal elevation (in the range of approximately $500 - 1500$ m), and observed velocity in these areas is low. The inferred friction coefficient is low from the grounding line and DDT area, up to the three tributaries, as well as beneath BIS. This is what would be expected as these are all areas of locally low basal topography and fast observed ice flow. Beyond the tributaries the friction coefficient increases, which is to be expected as ice flow speed decreases inland, and ice gets much thicker.

There is a high degree of variability between where the modeled velocity was higher or lower than the observed velocity (figure 3.19). However, the maximum misfit in each case was an overestimation of the friction coefficient from the inversion simulation. The maximum absolute value of the misfit for the Weertman, Budd and Schoof friction law inversions are 117.6 m/year, 115.6 m/year, and 116.0 m/year, respectively. The percentage of the nodes that record a misfit less than 50 m/year for the Weertman, Budd and Schoof friction law inversion are 99.6%, 99.8% and 99.6%, respectively.

There are two areas in particular that were prone to a larger misfit in each inversion simulation. At the base of the Theron Mountains, there is an area where the bed elevation steeply changes from approximately 250 m to -750 m, right before the grounding line (figure 3.18, green circle). The second area is on the floating ice shelf where there are two fractures of locally low ice thickness (figure 3.18, blue circle).
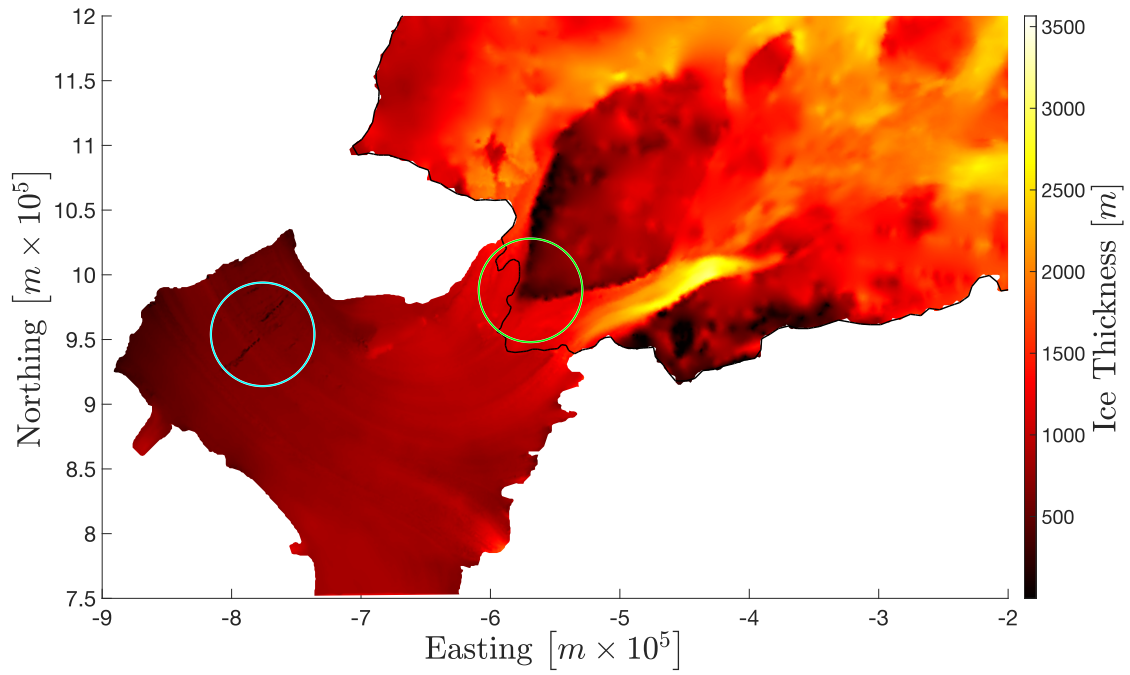
Figure 3.18: Ice thickness $[m]$ with areas that are prone to high misfit encircled. Area at base of Theron Mountains is surrounded by a green circle, fractures on the floating ice shelf are surrounded by a blue circle. Grounded ice is surrounded by a black line.
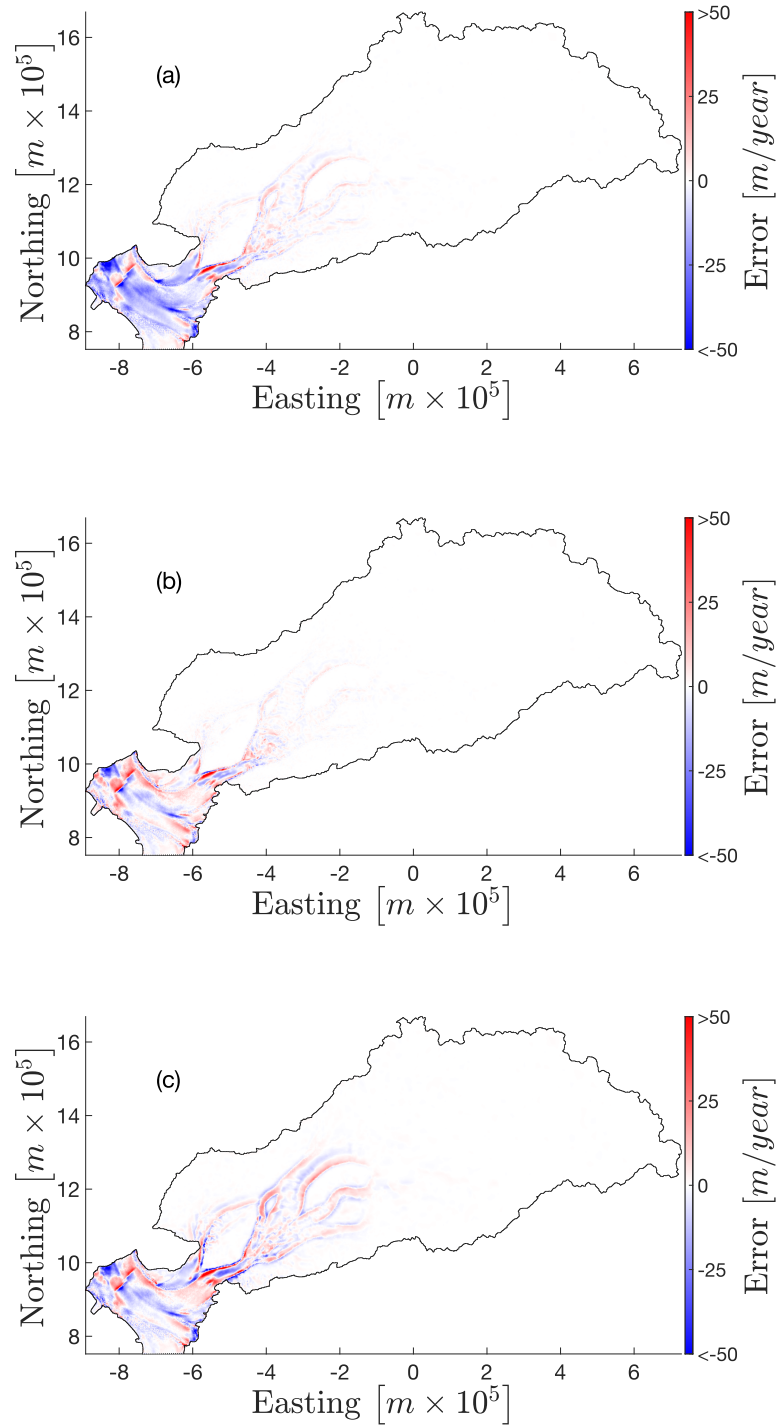
Figure 3.19: Misfit [m/year] between modeled velocity and observed velocity: (a) Weert-man friction law, (b) Budd friction law with effective pressure from brHL, (c) Schoof friction law with effective pressure from brHL. Misfit is capped at ±50 m/year to increase visibility of error. Blue represents higher modeled velocity.

The effect of changing the parameter m in the Weertman friction law was also tested by performing two additional friction inversions to see if the results are consistent with $m = 3$. The two additional values that are tested are $m = 1$ and $m = 2$, and these inversion simulations will be referred to as CW1 and CW2. The coefficients for the cost functions were selected following the same process as for the case of $m = 3$, and both inversions predict a low friction coefficient where there is fast observed ice flow (figure 3.20).
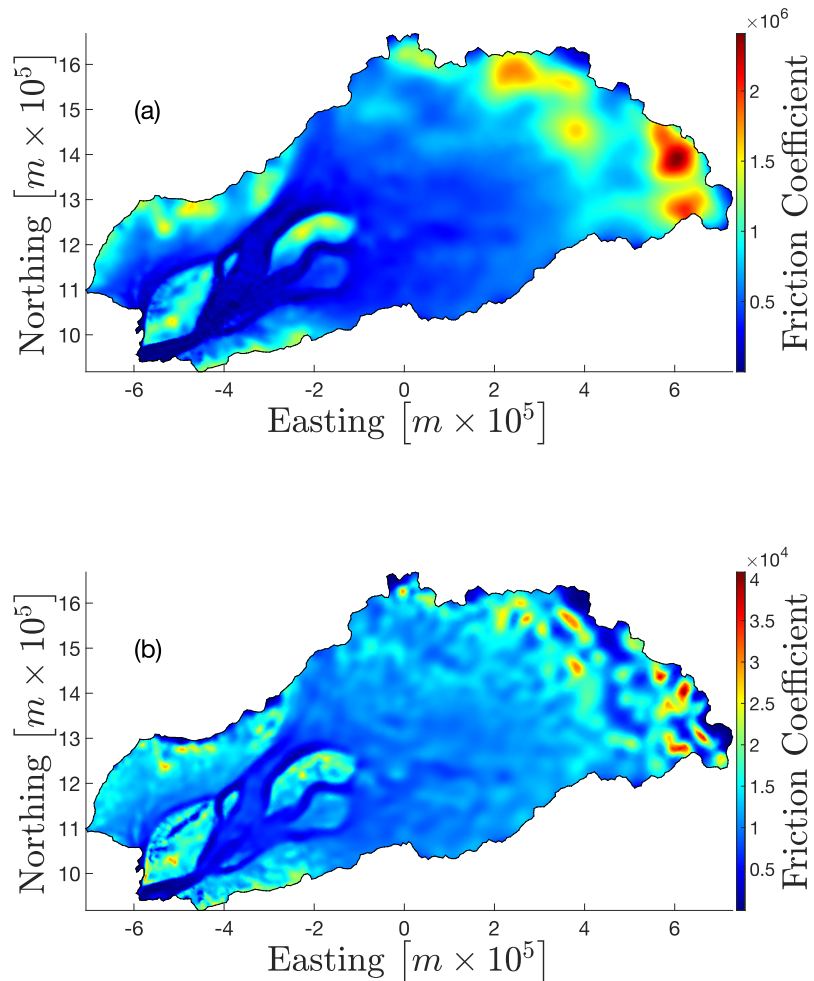
Figure 3.20: Inferred friction coefficients beneath grounded ice for the Weertman friction law when $m = 1$ (a) and $m = 2$ (b).

All values of m tested for the Weertman friction law successfully predicted low basal friction beneath areas of high observed ice flow speed. The error measured as the difference between observed and modeled velocity for CW1 and CW2 was consistent with what is presented in figure 3.19, and values can be seen in table 3.9.

Table 3.9: Statistics for friction inversion simulations. Overestimation refers to where the model is producing a velocity higher than what is observed. Percentage of nodes with a misfit less than 50 m/year and mean misfit are calculated for the absolute value of the misfit.

Friction Law	Nodes with overestimated velocity (%)	Magnitude of maximum misfit $[m/year]$	Nodes with misfit less than 50 m/year (%)	Mean misfit $[m/year]$
Weertman ($m = 3$)	56.5	117.6	99.6	5.0
Budd	46.3	115.6	99.8	3.5
Schoof	51.0	116.0	99.6	5.4
Weertman ($m = 1$)	52.2	116.3	99.8	4.0
Weertman ($m = 2$)	58.2	118.9	99.2	6.4

3.3   General Trends from the Models

The two-dimensional GlaDS subglacial hydrology model shows an active subglacial network at the base of Slessor Glacier, and that there is likely to be an area containing deep water in a deep trough near the outlet (DDT in figure 2.5). To investigate the effect of model parameters on the outputs, a sensitivity test was performed that is broken down into two components: (1) testing the sensitivity of the model to sheet and channel conductivity, and (2), testing the sensitivity of the model to water input and basal velocity.

In the first component of the sensitivity test, six base runs are compared that each use the same spatially variable water input and basal velocity data from the spatially variable data. This part of the test showed that a hydrological system forms beneath Slessor Glacier in all cases, but the outputs vary greatly depending on the choice of sheet conductivity, a poorly constrained parameter. The model predicted that there is likely to be deep water near the outlet of Slessor Glacier, and shallow water beneath the tributaries leading down to the BIS and Slessor Glacier outlets. The majority of the subglacial hydrological system is pressurized to nearly overburden, except for three areas of high basal elevation and very thin ice that surround the BIS and Slessor Glacier drainage outlets. A channel network forms at the Slessor Glacier outlet, in the DDT area and at the BIS outlet in all model runs. The spatial extent of the channel network and channel discharge extends further ugpglacier to the tributaries when a lower sheet conductivity is used.

The second part of the sensitivity test used the base runs from the first part as a benchmark to investigate the effects of using less realistic, constant water input and basal

velocity. On average, a constant water input caused more water to be present in the subglacial hydrological network, lower effective pressures, higher channel discharge, and a more spatially expansive channel network. Using the synthetic basal velocity did not make a significant difference to water input, channel discharge, or channel CSA, however, because of the impact basal velocity has on channel opening rate, there were major differences in effective pressure.

Inverse simulations performed with ISSM show that the basal friction coefficient is lower beneath areas of fast observed ice flow in the Slessor Glacier region. The L-curve analysis suggests the optimal trade-off between matching the observed velocity and removing large gradients in the friction coefficient solution; however, it was often the case that large gradients persisted, and the Tikhonov regularization coefficient had to be raised, which did not significantly impact the misfit between the observed and modeled velocities. An area containing a steep decrease in elevation and another area containing a fracture on the floating ice shelf were prone to a higher degree of mismatch between the modeled velocity and the observed for each friction inversion simulation. The results between the Weertman, Budd and Schoof friction law were consistent, and the inversion model effectively matched the modeled velocity to the observed in for each inversion. The choice of m in the Weertman friction law did not significantly impact where low basal friction is predicted.

Chapter 4

Discussion

Sensitivity tests are a common practice in subglacial hydrology modeling, including a model intercomparison project to test how different models compare with one another (De Fleurian et al., 2018). It is important to test the effects that parameters such as sheet conductivity, channel conductivity, water input and basal velocity have on model outputs as the practice of subglacial hydrology modeling has outpaced data collection, and these parameters remain poorly constrained. Moreover, it is likely that the previously mentioned four parameters are spatially and/or temporally variable, and assigning them constant values for model runs risks misrepresenting the likely future behaviour of glaciers and ice sheets. In this project, the issue of spatial variability of water input and basal velocity is mitigated by using the spatially variable data set calculated following methods laid out by Seroussi et al. (2020), however, sheet and channel conductivity remain constant across the entire domain, and temporal variation remains unaddressed.

Inverse methods are an effective way to estimate ice rigidity and basal friction, two parameters that are necessary to initialize any model that is going to predict the future evolution of a glacier. However, the ill-posedness and issue of lumping several glaciological processes into one coefficient introduces a large amount of uncertainty, and in that sense special care has to be taken when using them. Moreover, ambiguity is introduced by using a regularization term that penalizes strong gradients in the solution of the inversion method, and small-scale spatial features can be lost. Three friction laws as described by Weertman (1957), Budd et al. (1979) and Schoof (2005) are tested to remove any potential bias that using just one law may introduce, and for the Weertman friction law, an exponent parameter is varied to investigate its impact on the solution.

The motivation behind this project was three-fold:

1. To assess the most appropriate parameterizations of the GlaDS subglacial hydrology model by comparing subglacial hydrology and ice dynamics model outputs,

2. to provide a tractable subglacial hydrology modeling workflow that involves inverting for basal friction as a means to validate subglacial hydrology models,

3. to study subglacial hydrology and ice dynamics in the Slessor Glacier study area.

The remainder of this section will first discuss limitations of the model outputs. This will be followed by a comparison between the subglacial hydrology model and ice dynamics model outputs, and then another comparison between the subglacial hydrology model outputs and ice shelf melt data and basal channel locations. Finally, this chapter will finish with the description of a tractable workflow that subglacial hydrology modelers can use to validate their results with ice dynamics models, and the limitations of this proposed method are also considered.

4.1 Limitations of the Models

A prominent issue with the GlaDS model was that the domain would not pressurize across all the base runs at areas of locally high topography near the grounding line, i.e., the Touchdown Hills, Theron Mountains and Shackleton Range. This problem was slightly less present when sheet conductivity was lowered, but persisted in all base runs. The areas that would not pressurize all contain thin ice, little to no predicted melt, steep gradients in bed and surface elevation and surrounded valleys containing efficient drainage systems where all the water from the catchment is draining. Areas such as these are difficult for the GlaDS model to handle due to steep gradients in topography and, to remedy these issues, it is likely that a non-physical amount of artificial ice thickness and topography smoothing must be imposed; to run a subglacial hydrology model similar to GlaDS, Hager et al. (2021) impose a maximum bed elevation of 1200 m, a minimum ice thickness of 550 m, and run the ice dynamics portion of their model for 15 years to smooth gradients in ice thickness over Mt. Takahe where bed elevation reaches ~ 3000 m and ice thickness is often 0.

To this end, it is desirable that a subglacial hydrology model has means to directly deal with topography of this nature to prevent a high degree of alteration to the real observed data. In reality, however, parts of the Shackleton Range and Theron Mountains have exposed bedrock, and so there is no subglacial water here to pressurize (figure 4.1).
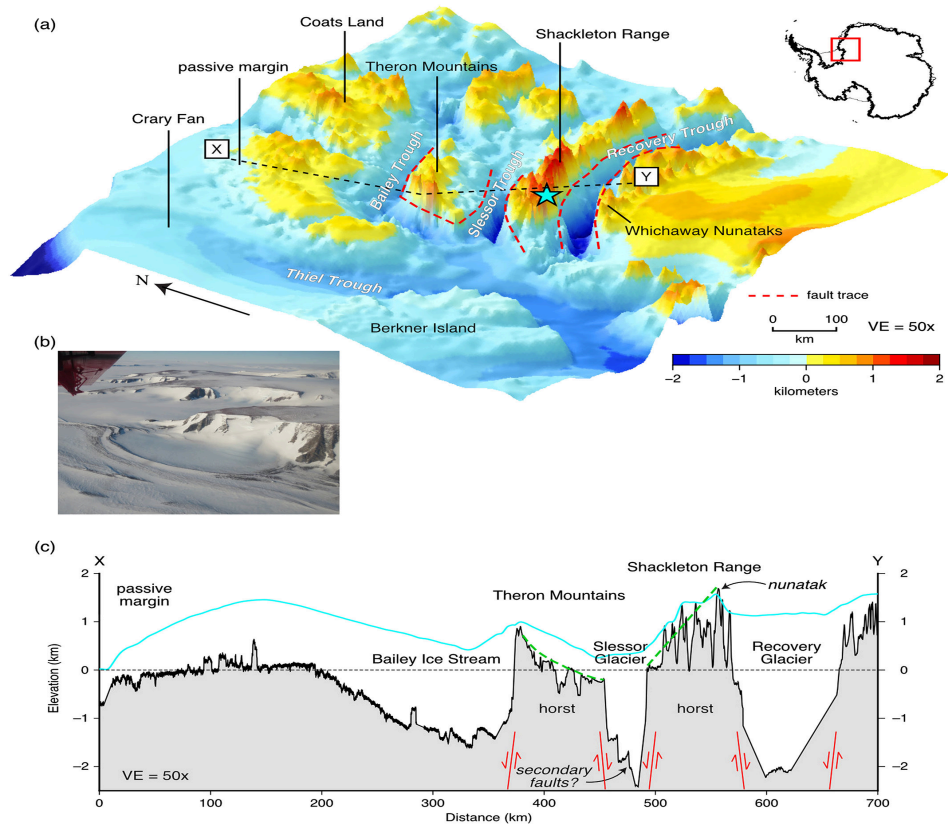
Figure 4.1: (a) 3D visualization of Slessor Glacier and surrounding area. (b) Photograph of area in the Shackleton Range marked by blue star in subfigure (a). (c) x, y cross sectional view of the Slessor Glacier area with bed surface marked by black line and ice surface marked by blue line. From Paxman et al. (2017).

A limitation of the ice dynamics model is that, by itself, it provides no means of inferring which friction law performed better, and which is more appropriate to the area. The misfit is a representation of the numerical model, not the physics of the glacier, and differences in results are a consequence of parameter choice and whether or not the ice dynamics model converges. The modeling setup used for the ice dynamics model in this project allows one to remove bias from using just one friction law, but does not yield any appreciable result for which law is more suitable for the study area. Moreover, each friction law incorporates all error from ice flow miscalculation as well, and while this is slightly mitigated by comparing the modeled basal friction coefficient results to effective pressure, this is just one component of many that exist in the subglacial hydrological system.

4.2 Parameter Selection and Model Outputs

The GlaDS subglacial hydrology model outputs show that deep water and low effective pressure closely match high observed surface velocity (figure 4.2), and these features are

important to be correlated with one another as they are closely linked (Fountain and Walder, 1998). The most prominent areas of high pressure and water depth are the Slessor Glacier outlet, DDT area and the BIS outlet, though when sheet conductivity is lowered and/or water input is increased, the spatial extent of these features moves further upglacier to the three tributaries beneath Slessor Glacier. The high water content and pressure gives rise to an arborescent system of R-channels that drain the water from the catchment out of the Slessor Glacier and BIS outlets, and like water pressure and depth, the spatial extent of the channelized drainage system moves further upglacier when sheet conductivity is lowered.
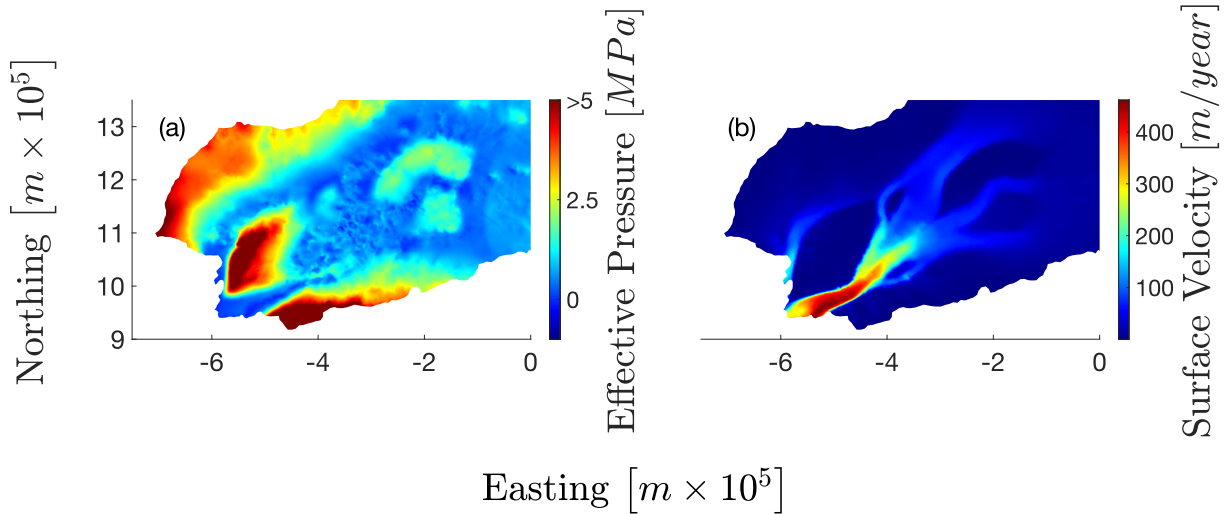
Figure 4.2: (a) Effective pressure at the end of brLM and (b) MeASUREs surface velocity (Mouginot et al., 2019). Colour bar for effective pressure is capped to highlight similarities with surface velocity.

The first part of the sensitivity test demonstrated that sheet and channel conductivity play a role in determining where water depth and pressure are high, and the spatial extent and arborescence of the channel system. The second part of the sensitivity test highlighted that water input has a profound effect on the spatial extent and values of all measured outputs, and that basal velocity plays a role in subglacial water pressure.

The current knowledge of Antarctic subglacial hydrology suggests that drainage is close to SS, and for this reason, the effective pressure beneath the majority of the domain should be near zero (Dow et al., 2020). Across the base runs, there was a clear trend of lower effective pressure (higher flotation fraction) across the entire domain for base runs with the lowest tested value of sheet conductivity, 10^{-4} m$^{7/4}$kg$^{-1/2}$ (figure 3.2, table 3.4). Therefore, in the Slessor Glacier study area, it is more likely that a the lower tested value of sheet conductivity is more appropriate. Interestingly, the base runs with the lower sheet conductivity simulate channel discharge persisting 500 km from the grounding line, a distance significantly further inland than what has been produced by other modeling studies (e.g., Dow et al., 2020; Wei et al., 2020; Hager et al., 2021). The results of the

sensitivity test do not provide a clear answer on which channel conductivity value is most appropriate, and at this point, further consideration is still required.

The inversion model outputs varied in range of friction coefficient, but areas where the coefficient is high and low are consistent. The inversion simulations performed with ISSM show that the basal friction coefficient is lowest, and near zero near the Slessor Glacier outlet, but also low near the BIS outlet and upglacier from both outlets up to the three tributaries beneath Slessor Glacier. These results are similar to what is predicted in this area by others when conducting Antarctic-wide friction coefficient inversions (e.g., Morlighem et al., 2013; Arthern et al., 2015). Additionally, the coefficient of basal friction remains low beneath the tributaries where ice flow speed is low ($40 - 90$ m/year) when compared to the outlet and DDT area ($300 - 400$ m/year). This demonstrates that fast basal sliding is not necessarily restricted to just areas of fast ice flow. Indeed, Morlighem et al. (2013) found that for approximately 80% of Antarctica, the basal velocity at any given location could exceed 30% of the measured surface velocity at that same location. However, these results are quite different from what is suggested by Rippin et al. (2006), where they suggest that STC and STS (c.f., figure 2.5) move solely by ice deformation.

The low basal drag coefficient beneath areas of fast observed ice flow is consistent with areas of water accumulation and low effective pressure from the GlaDS output, and so the consistency between the models suggests that there is an active subglacial system beneath Slessor Glacier giving rise to fast ice flow speeds (figure 4.3 and table 4.1). An arborescent channel network with large channel CSA and discharge forms in all GlaDS model runs where basal friction is predicted to be the lowest, and also where observed velocities are fastest for grounded ice. These results would not be expected for a mountain glacier where seasonal variation and surface melt are major drivers of the subglacial hydrological system, but are consistent with the SS drainage system beneath Antarctica.
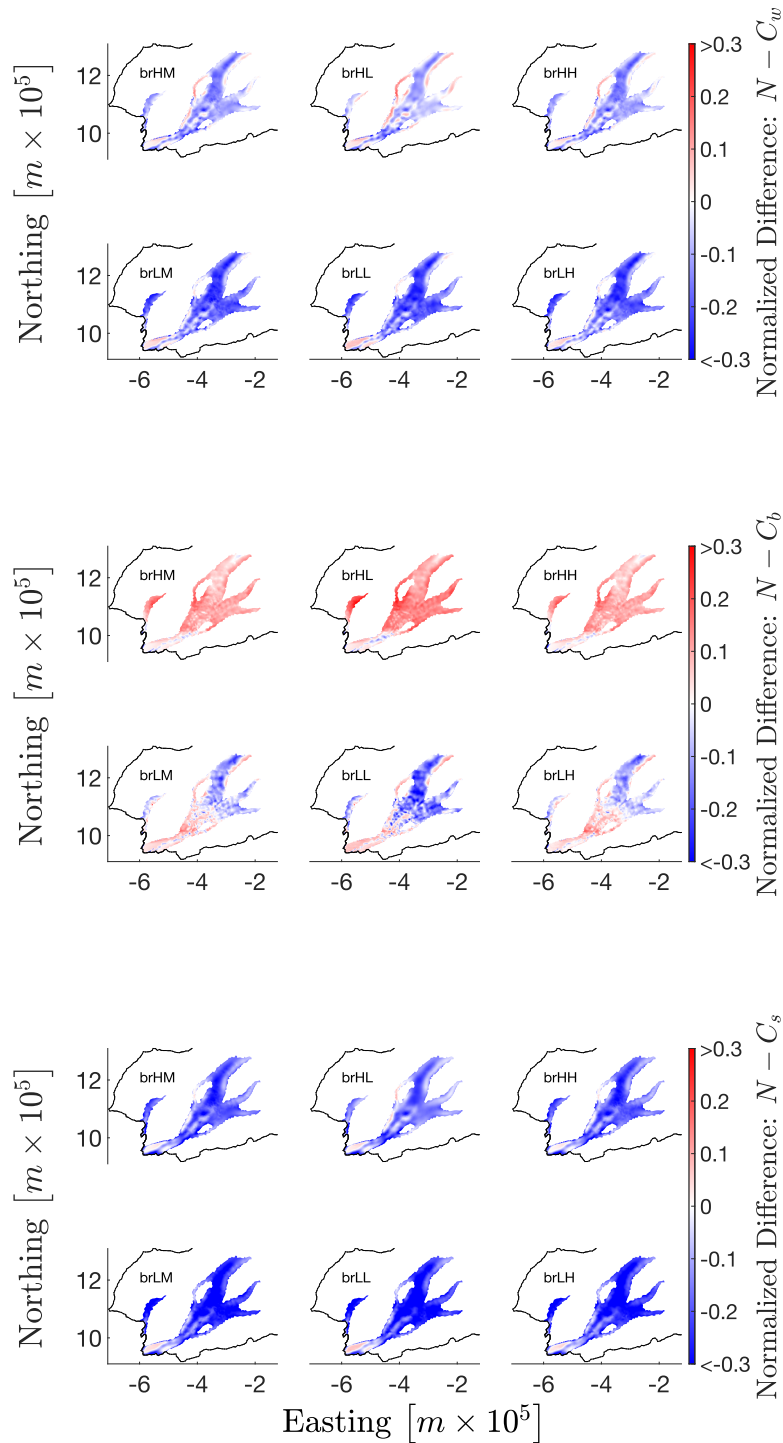
Figure 4.3: Difference plots between normalized effective pressure for each base run and friction coefficient from the three friction law inversions. Difference is restricted to areas with observed ice velocity ≥ 50 m/year. Model run parameterizations are denoted by inset labels, and relevant friction law is denoted on colour bars. Colour bar is capped at ± 0.3 to highlight areas with small differences.

Table 4.1: Mean of absolute value of difference between normalized effective pressure and friction coefficient for all base runs.

Friction Law	Base Run	Mean Normalized Difference
Weertman	brHM	0.09
Weertman	brHL	0.07
Weertman	brHH	0.09
Weertman	brLM	0.14
Weertman	brLL	0.14
Weertman	brLH	0.14
Budd	brHM	0.08
Budd	brHL	0.11
Budd	brHH	0.08
Budd	brLM	0.07
Budd	brLL	0.10
Budd	brLH	0.06
Schoof	brHM	0.16
Schoof	brHL	0.13
Schoof	brHH	0.16
Schoof	brLM	0.21
Schoof	brLL	0.21
Schoof	brLH	0.21

Subglacial water pressure is expected to be near overburden across the entire domain for SS drainage in Antarctica, with the most pressurized areas (i.e., lowest effective pressure) occurring beneath areas of fast ice flow. However, the basal friction coefficient is low in areas of fast ice flow only, which suggests that low values of effective pressure and basal friction will be a proxy for one another in areas of fast ice flow. For this reason, the consistency of the two models will be assessed by comparing where low effective pressure and basal friction coefficient agree on nodes that correspond to an observed surface velocity ≥ 50 m/year from the MeASUREs surface velocity data set (Mouginot et al., 2019).

Effective pressure for each base run is normalized to the range $[0, 1]$, and similarly, the inferred basal friction coefficients from each friction law are normalized to the range $[0, 1]$. From here, the difference between the two quantities is taken to assess their consis-

tency. The normalized differences using the Weertman and Budd friction laws are generally smaller than the Schoof friction law. However, the results from the normalized differences using the Weertman and Schoof friction laws suggest the highest tested value of sheet conductivity (10^{-3} m$^{7/4}$kg$^{-1/2}$) produces the most consistency between effective pressure and basal friction coefficient, but the results from the normalized difference using the Budd friction law suggest the lowest tested value of sheet conductivity (10^{-4} m$^{7/4}$kg$^{-1/2}$) is more consistent, albeit not by a significant amount. These results imply that the Budd friction law is most appropriate for the Slessor Glacier study area as the Budd friction coefficient is most consistent with effective pressure for the GlaDS simulations that use a sheet conductivity of 10^{-4} m$^{7/4}$kg$^{-1/2}$, i.e., the base runs with the most pressurized domain. Moreover, the normalized differences using the Budd friction law are smallest for the higher two values of channel conductivity, which suggests a channel conductivity $\geq 5 \times 10^{-2}$ m$^{3/4}$kg$^{-1/2}$ may be most appropriate. Constraining the channel conductivity is an important result as both channel and sheet conductivity are difficult to measure directly, as well as difficult to constrain from subglacial hydrology modeling alone, especially in the absence of radar-based specularity data.

It is worth addressing the existence of a channelized system persisting > 500 km from the grounding line as is simulated by GlaDS in many of the transient simulations. As stated earlier, no subglacial hydrology models have simulated a channelized system of this spatial extent to date. However, there are several factors that could allow such a system to form. Slessor Glacier is within a very large drainage basin ($\sim 570,000$ km^2) with funnel-like geometry not just near the grounding line, but up to the three tributaries as well. These topographic controls allow the large volume of water generated from geothermal heat and friction upglacier to funnel into the tributaries, and then down to the grounding line. The GlaDS simulations suggest that sufficient water is generated to melt large R-channels that can persist at a pressure near overburden year-round from the Slessor Glacier grounding line up to the three tributaries. A perennial channelized system of this magnitude could alter the current understanding of subglacial drainage networks in Antarctica, and this should motivate observational studies to be conducted in this area.

4.3   Ice Shelf Melt Rates and Basal Channels

Discharge rates near the grounding line can be compared to melt rate data and basal topography at the base of the Filchner Ice Shelf to assess how well the model outputs agree with observations. For this analysis, all 48 transient model runs are considered, and only edges that record a discharge greater than 0.1 m^{3}s^{-1} at the final time step of model runs are considered. There are three areas of significant melt on the Slessor Glacier and BIS drainage outlet (figure 4.4).
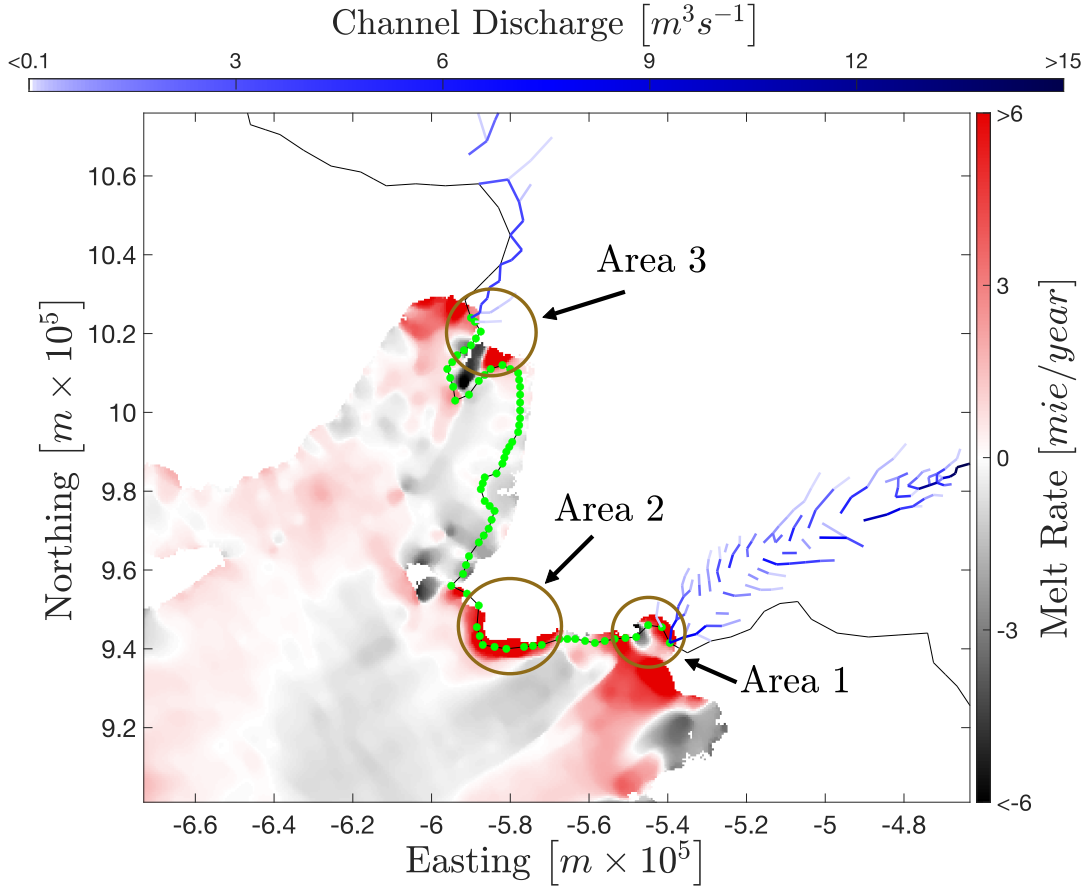
Figure 4.4: Areas of locally high ice shelf melt rate on the Filchner Ice Shelf. A positive melt rate corresponds to melting. Channel discharge on GlaDS mesh edges from brLM are overlain in shades of blue. An outline of the model boundary is in black, green dots represent grounding line nodes, and brown ellipses represent three areas of high observed shelf melt rates. Melt rate data is from Adusumilli et al. (2020).

All transient runs discharge water in areas 1 and 3. At area 1, there is an average shelf melt rate of approximately 16 mie/year, and across all 48 transient model runs there is an average discharge of 19.5 m^{3}s^{-1}. Similarly, at area 3, there is an observed melt rate of approximately 10 mie/year and a mean channel discharge of 17.9 m^{3}s^{-1}. The higher melt rate measured at area 1 is consistent with the higher mean discharge measured at this area. A summary of discharge across the base runs as opposed to the average of all model runs is presented in table 4.2.

Table 4.2: Discharge at areas 1 and 3 at the final time step of the base runs. The discharge measured at area 3 for brHL is less than 0.1 m^{3}s^{-1} so it is not recorded.

Run	Discharge at area 1 [m^{3}s^{-1}]	Discharge at area 3 [m^{3}s^{-1}]
brHM	11.9	2.7
brHL	1.22	$< Q_0$
brHH	12.1	3.0
brLM	15.0	3.3
brLL	4.5	0.4
brLH	15.7	43.2

At area 2, there is a measured discharge of approximately 18 mie/year, yet the mean channel discharge measured here is 0.01 m^{3}s^{-1}, which is less than Q_0. There are several reasons that could explain the absence of significant discharge here, including insufficient refinement of the mesh due to the $\sim 20,000$ node restriction in Matlab, topography smoothing in the DDT area (figure 2.6), little melt water input (figure 3.5, subfigure (c)), and improper estimation of the grounding line (e.g., Le Brocq et al. (2013) use a grounding line for Slessor Glacier that suggests the entire DDT area is floating).

Channel discharge locations at the Slessor Glacier grounding line are used to deduce where basal channels on the Filchner Ice Shelf are located, and hillshading is applied to the basal topography data to highlight topographic depressions (figure 4.5).
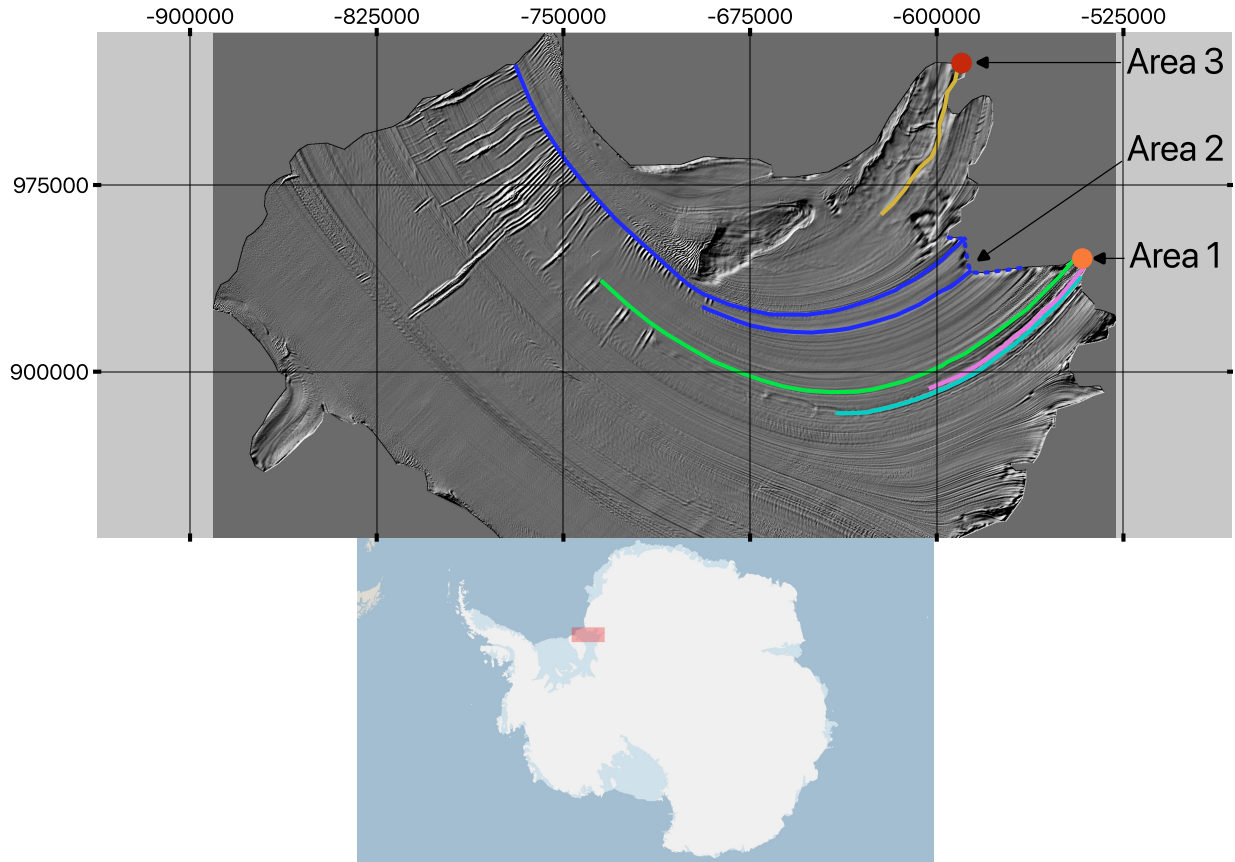
Figure 4.5: Basal topography of the Filchner Ice Shelf. Coloured lines represent basal channels and coloured circles represent areas of modeled discharge in areas 1 and 3. The zone of high observed shelf melt rate from Adusumilli et al. (2020) where models do not simulate discharge at the grounding line (area 2) is represented by a dotted blue line, and two basal channels originating from that area are shown by blue lines. Hillshade is applied to the basal topography data to highlight topographic depressions, and the study area is shown in the image below.

At area 1, three basal channels appear to have formed beneath the ice shelf. The cyan, pink and green channels have lengths of 118 km, 81 km and 224 km, and widths of 1.4 km, 1.1 km and 1.0 km, respectively. There is also a 70 km-long basal channel beginning at area 3 that has a width of 3.1 km. At the area of melt where transient model runs do not predict discharge over the grounding line (dotted blue line in figure 4.5), two channels form. The longer of the two channels in this area spans the entire ice shelf with a length of 240.0 km, and the shorter is 117.9 km long, and these two channels have widths of 0.9 km and 0.6 km, respectively. All channels tend to follow the direction of ice flow on the Filchner Ice Shelf.

There are two large rifts[1] on the Filchner Ice Shelf upstream from a basal pinning point[2],

---

[1]A rift is a full-ice-thickness fracture perpendicular to the direction of ice flow. They are a known precursor to iceberg calving.

[2]A pinning point is an area of locally high basal topography that re-grounds a floating ice shelf. Pinning

and there is a clear pattern of ice rigidity near these rifts; ice rigidity is high, suddenly lowers, and then raises again (solid black lines in figure 4.6). This is likely a consequence of the rift being accounted for in the input data for ISSM, and is in turn what is causing the change in rigidity at the exact rift sites.

The high rigidity upstream of the fractures could have played a role in their formation; indeed, Emetc et al. (2018) demonstrate that locations of rigid ice can be used as a precursor to detect the location of fractures on ice shelves.
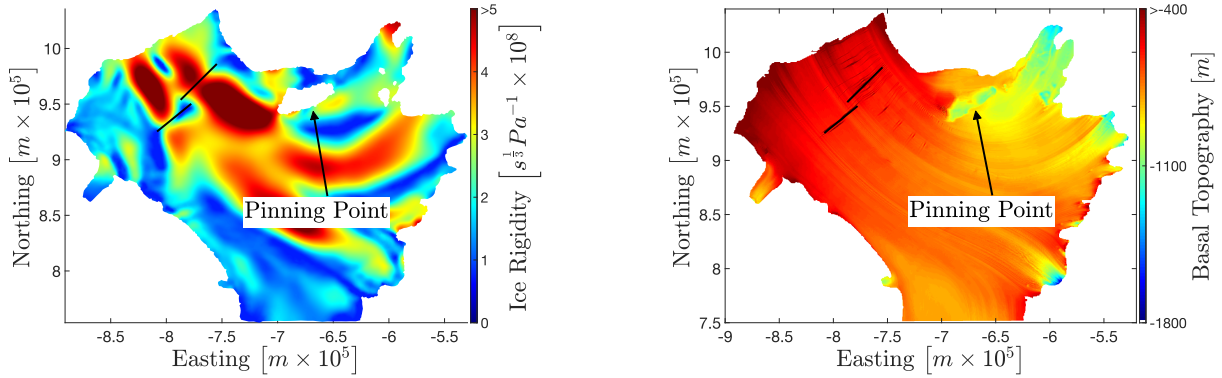
Figure 4.6: Inferred ice rigidity and ice shelf basal elevation. Pinning point is indicated with a black arrow, and two solid black lines indicate two large fractures in the ice shelf. Basal topography is in meters with respect to height above sea level.

The results presented in table 4.2, and the evidence of basal channels on the Filchner Ice Shelf are used to supplement the choice of base run parameterization made in section 4.2. One key difference here is that it is evident that base runs with a low channel conductivity are not simulating sufficient discharge at the BIS and Slessor Glacier outlets to reflect the high shelf melt rates and ice shelf basal channels. Indeed, brHL does not record a significant discharge here at all, yet has the lowest mean normalized difference across all base runs for both the Weertman and Schoof friction laws.

This is a key finding as it was not evident from the sensitivity test alone which value of channel conductivity was most appropriate for the Slessor Glacier study. At this point, the sensitivity test and a comparison with observed ice shelf data together suggest that brLM and brLH are most likely to be representing the subglacial hydrological system beneath Slessor Glacier (figure 4.7). Additionally, the comparison with observed ice shelf data further supports the choice of the Budd friction law being most appropriate for the Slessor Glacier study are as it was the only friction law tested that suggested the higher values of channel conductivity better reflect the subglacial hydrological system. Thus, the normalized difference method accurately constrained both channel and sheet conductivity when using the Budd friction law.

points provide additional buttressing force through basal drag Cuffey and Paterson (2010).
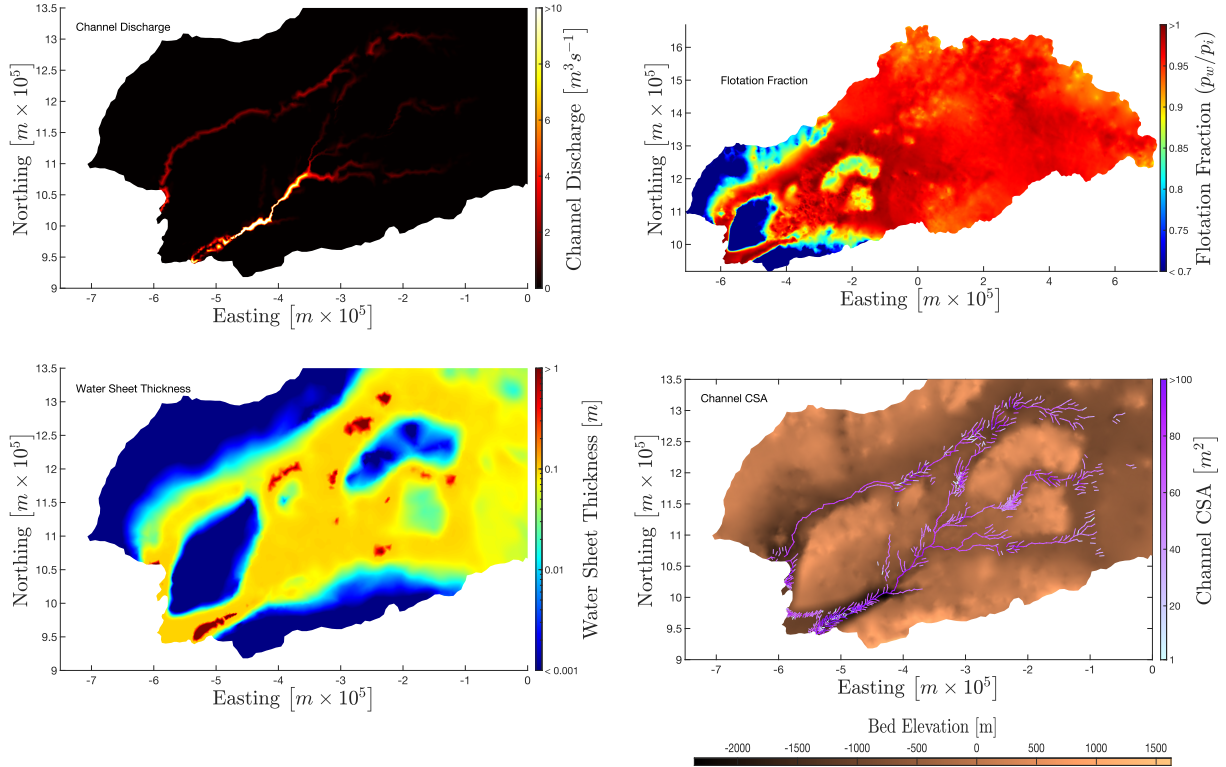
Figure 4.7: Results form brLM which have been found to most likely be representative of the subglacial hydrological network beneath Slessor Glacuer and the BIS.

4.4 Comparison with Existing Literature

To assess the outputs of the subglacial hydrology and inversion models, comparisons can be made with existing literature that has provided data on Antarctic wide subglacial water flux, subglacial lake locations, and basal friction.

4.4.1 Subglacial Water Flux

Willis et al. (2016) modeled several hydrological characteristics of subglacial basins in Antarctica that can be compared to the outputs from the sensitivity test performed in this thesis. One key difference between the model outputs from Willis et al. (2016) and the work here is that Slessor Glacier and Bailey Ice Stream are within two separate drainage basins, where the Bailey Ice Stream drainage basin has an area of 3.37×10^{11} m^2 and the Slessor Glacier drainage basin area is 2.42×10^{11} m^2, giving a total area of 5.79×10^{11} m^2 ($\sim 0.09 \times 10^{11}$ m^2 larger than the area calculated for this thesis). The total discharge calculated by Willis et al. (2016) was based on total accumulated melt flux for the drainage basin, and the discharge for BIS and Slessor Glacier are 20.51 m^{3}s^{-1} and 33.63 m^{3}s^{-1}, respectively. In the model runs performed in this thesis, efficient drainage across the grounding line occurs at two locations, one at the BIS outlet (area 3) and another at the

98

Slessor Glacier outlet (area 1). The mean discharge at the BIS outlet in the sensitivity test is 17.9 m³s⁻¹, which is 2.6 m³s⁻¹ lower than the modeled discharge by Willis et al. (2016), and at the Slessor Glacier outlet, the mean discharge in the sensitivity test 19.5 m³s⁻¹, 14.1 m³s⁻¹ lower than what was modeled by Willis et al. (2016). It is worth noting that the outputs from the sensitivity test just refer to channelized output and there is water exiting the domain from the distributed sheet as well.

Le Brocq et al. (2013) also modelled subglacial water flux beneath the Antarctic ice sheet, and these results are compared to the base runs graphically in figure 4.8 by interpolating the flux onto the GlaDS mesh (figure 2.8).
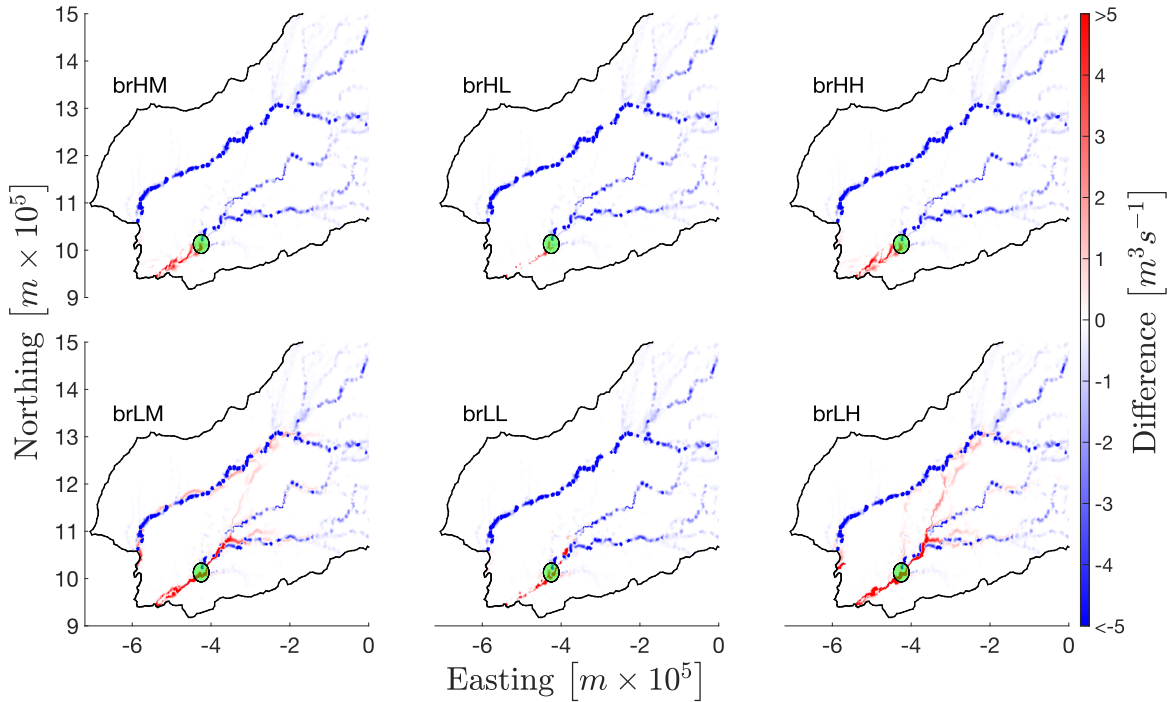
Figure 4.8: Comparison of channel discharge between model outputs from the sensitivity test (red) and an Antarctic-wide model simulation of subglacial water flux performed by Le Brocq et al. (2013) (blue). Slessor Glacier grounding line used by Le Brocq et al. (2013) is represented by opaque green circle. Colour bar is capped at ±5 m³s⁻¹ to highlight differences between the two models.

At the BIS outlet, Le Brocq et al. (2013) record a discharge of approximately 26 m³s⁻¹, which is 8.1 m³s⁻¹ higher than the mean discharge here in the sensitivity test. At the Slessor Glacier outlet suggested by Le Brocq et al. (2013), their model suggests a water flux of approximately 10 m³s⁻¹, which is 9.5 m³s⁻¹ lower than the average discharge at the Slessor Glacier outlet across all 48 model runs.

Discrepancy between the simulated flux from Le Brocq et al. (2013) and Willis et al. (2016) is likely due to a number of reasons including a difference in drainage basin and model boundaries between these projects, as well as assumptions made for each of these

models. Both Le Brocq et al. (2013) and Willis et al. (2016) use the Shreve equation (Shreve, 1972), which assumes overburden water pressure across the entire Antarctic continent. This introduces a significant amount of error into their calculations. Their methods also lump discharge from both channelized and distributed drainage into one, as opposed to more accurately prescribing independent means of representing those drainage modes as in the GlaDS model. Moreover, it was demonstrated in section 3.1.2 that water input has a significant control on model outputs, and the two studies discussed here use different water inputs than what was used in the sensitivity test. Willis et al. (2016) calculate basal melt flux using a three-dimensional ice flux flow model and Le Brocq et al. (2013) use modeled subglacial melt rates calculated by Pattyn (2010). These different volumes of water driving the models add to the discrepancy in subglacial water flux.

4.4.2 Subglacial Lakes

Although the hydrology model setup used here is not ideal for analyzing subglacial lake activity beneath Slessor Glacier, the water sheet thickness can still be analyzed to see where the base runs suggest subglacial lakes form and drain (figure 4.9). The time step corresponding to the maximum water sheet thickness will be used to determine where the model suggests lakes form, and to be considered a lake, the feature must have at least one node with a water sheet thickness greater than 1 m, and the feature must show up across at least all base runs with an equivalent sheet conductivity. The latter is necessary as the runs with a lower sheet conductivity often have water pooling in several different locations due to the distributed system conducting water poorly, which makes it difficult to discern what might be a subglacial lake location (e.g., subfigure brLL in figure 4.9). Lake locations are compared to shape files for predicted subglacial lake locations from Smith et al. (2009), however, in the most recent inventory of Antarctic subglacial lakes (Livingstone et al., 2022), subglacial lakes $Slessor_2$ and $Slessor_3$ from Smith et al. (2009) have been determined to be just one subglacial lake, now labelled $Slessor_{23}$ (Slessor23 in figure 4.9, subfigure brHM). As well, neighbouring subglacial lakes $Slessor_4$ and $Slessor_5$ from Smith et al. (2009) and Livingstone et al. (2022) will be labelled Slessor45 and treated as one location for convenience.
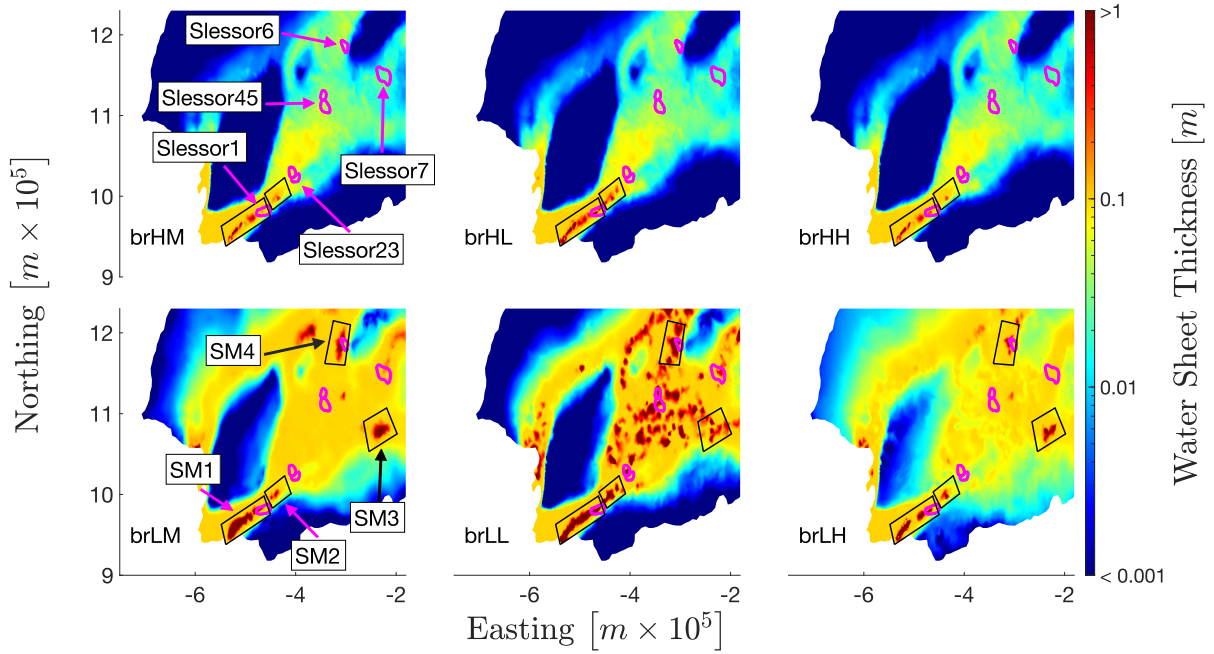
Figure 4.9: Predicted subglacial lake locations at time step corresponding to maximum water sheet thickness. Black polygons represent potential subglacial lake locations from the model runs and magenta polygons represent subglacial lake locations from Smith et al. (2009). Modeled lake locations are labeled in subfigure brLM and use naming convention SM, and observed lake locations use a naming scheme based on the one suggested by Livingstone et al. (2022).

Modeled lakes that are here called SM1 and SM2 occur for all base runs, and these locations likely correspond with observed lakes Slessor1 and Slessor2, respectively. There are two additional modeled subglacial lake locations, SM3 and SM4, and they only appear in the base runs with the lowest tested value of sheet conductivity. Modeled lake SM3 is not recorded in the most recent inventory of subglacial lakes and could correspond to a subglacial lake location not currently found, but may be an artifact erroneously produced by the model. Lastly, modeled lake SM4 corresponds very closely with the location of subglacial lake Slessor6 in the most recent inventory (Livingstone et al., 2022). The base runs with a lower sheet conductivity simulating SM4 provides further evidence that the lowest tested value of sheet conductivity, 10^{-4} m$^{7/4}$kg$^{-1/2}$, is most appropriate.

Nearly all modeled subglacial lake locations in the base runs fill and drain slowly as the transient run approaches SS, excepting modeled lake SM1 in brLL, where the lake initially drains, enters a quiescent period, and then refills in $\sim$ 13 years (figure 4.10, subfigure SM1, magenta line). This is comparatively longer than the entire drain and fill cycle of the slightly upglacier Slessor$_{23}$ measured by Fan et al. (2022), which lasted only $\sim$ 5.6 years.
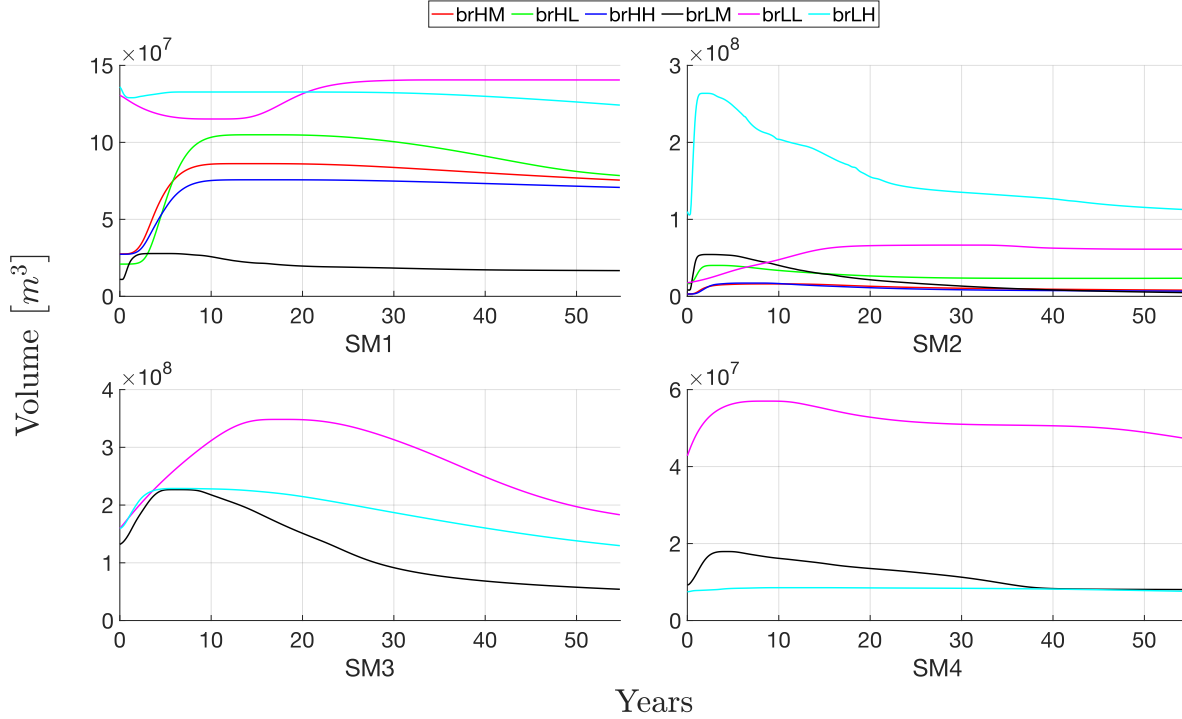
Figure 4.10: Volume across all time steps of node that corresponds to highest water sheet thickness in the modeled subglacial lake locations.

4.4.3 Basal Friction Coefficient

Two Antarctic-wide basal friction inversions have been conducted by Morlighem et al. (2013) and Arthern et al. (2015). Both inversions predict a low coefficient of basal friction beneath the Slessor Glacier and BIS outlets, extending up to the three tributaries beneath Slessor Glacier. Morlighem et al. (2013) conclude that at Slessor Glacier, low friction is not restricted to the DDT area and grounding line, but widespread far into the drainage basin of Slessor Glacier, which is consistent with the findings found here. The results presented by Morlighem et al. (2013) and Arthern et al. (2015) are from simplified, linear basal friction laws that do not account for subglacial water pressure, and because of these assumptions, the results presented in this study are stronger as, at the very least, each friction law is nonlinear, but for the Budd and Schoof friction laws, a dependency on effective pressure is introduced, which better represents subglacial processes. A second strength is that a higher resolution basal friction coefficient is provided, better capturing the small scale processes in an area of nontrivial bed geometry at the Slessor Glacier/BIS study area.

4.5 A Workflow for Model Validation Using Inverse Methods

The ideal model to predict the future behaviour of ice masses in Antarctica would completely couple subglacial hydrology to ice dynamics, and have a plethora of past data to accurately calibrate all model parameters. However, coupling ice dynamics to subglacial hydrology is theoretically and computationally demanding, and the necessary data for calibration is covered by kilometre-thick ice in one of the most remote and difficult areas to access on Earth. To compensate for these difficulties, subglacial hydrology and ice dynamics models tend to remain uncoupled, and when they are coupled, major assumptions are made, e.g., Pimentel and Flowers (2011) assume distributed drainage in one dimension only, and Hoffman and Price (2014) assume an idealized mountain glacier. More recently, Cook et al. (2020) coupled a three-dimensional Stokes ice dynamics model, the two-dimensional GlaDS model, and a one-dimensional ocean plume model to investigate subglacial hydrology and ice dynamics processes at Store Glacier, West Greenland. While this was an ambitious project that yielded enlightening results, simplifications like using a linear Weertman-type friction law, not performing a sensitivity test to determine the appropriate GlaDS parameterization, and a lack of of 2-way coupling between the GlaDS and Stokes models are prominent limitations to the study, but necessary to decrease computational cost and time. The previous three examples highlight why independent modeling projects still exist and also why there does not yet exist a computationally efficient means of completely coupling ice dynamics to subglacial hydrology. To this end, a tractable workflow that incorporates subglacial hydrology and ice dynamics will now be given, and while supplementing the model outputs with observed data will certainly increase the confidence in results, is not necessary.

A sensitivity test is an essential part of any subglacial hydrology modeling project as model parameters like sheet conductivity and water input have profound effects on model output, yet remained poorly constrained. Moreover, models are prone to numerical errors in areas of steep topography changes, and effort must be made to understand the role topography plays in parameterization and model output. A typical sensitivity test by itself would highlight the effects of sensitive model parameters such as sheet conductivity, channel conductivity, and water input, and from there, the modeler is left to decide the most appropriate parameterizations based on the current knowledge of subglacial hydrology in the study area. However, without an additional means of model validation, the confidence in the choice of model parameterization can be limited. This was demonstrated in this thesis by having no clear ideal choice of channel conductivity from the sensitivity test alone, despite its importance in the development of a subglacial hydrological system. Indeed, a channel conductivity of 10^{-3} m$^{3/4}$kg$^{-1/2}$ produced no clear difference in effective pressure when compared to outputs from other simulations using different values of channel conductivity, but caused GlaDS to simulate too little discharge at area 3 in figure 4.4, an area likely contributing to the formation of a 70 km channel on the base of the Filchner Ice Shelf.

This leaves the modeler desiring another means of model validation, which would typ-

ically involve comparing the outputs to observed data. However, if data is not readily available, the modeler is somewhat stuck. This is where comparing subglacial hydrology model results with an ice dynamics model can be used. In areas of fast observed grounded ice flow Antarctica, one would also expect low effective pressure as well as a low basal drag coefficient, and so the two could be compared to one another by some means, such as inverse methods. The ISSM model (Larour et al., 2012) as well as the MeASUREs surface velocity data set (Mouginot et al., 2019) are both free to use and access, and performing inversions as those described in this study are significantly less computationally demanding than even GlaDS hydrology simulations. This allows one to easily infer the basal friction coefficient for several friction laws without the need of external computational resources, and then a comparison of effective pressure and the basal friction coefficient can be made via normalization. The strength of including the normalized differences was demonstrated in this study by showing that at the Slessor Glacier study area, the Budd friction law was most appropriate, and the results from the normalized difference using the Budd friction law accurately constrained both the sheet and channel conductivity. However, it is important to remember that the most effective means of model validation will always be a direct comparison to observed data. This claim is highlighted in this study by comparing simulated outlet discharge from GlaDS to observed ice shelf melt rates and basal channel locations on the bottom of the Filchner Ice Shelf. Both the Weertman and Schoof friction laws resulted in normalized differences that imply a channel conductivity of 10^{-3} m$^{3/4}$kg$^{-1/2}$ agrees best with results from the subglacial hydrology model. Yet, the base runs with this parameterization result in negligible discharge at the origin of a large channel on the base of the Filchner Ice Shelf.

At this point, a choice of appropriate parameterization(s) based on the values tested in this project can be made. Putting all these results together suggest that the parameterizations for brLM and brLH are the most appropriate of the tested parameterizations to use for modeling subglacial hydrology at the Slessor Glacier study area. It is important to highlight that it is not singular values of sheet and channel conductivity that are concluded to be most appropriate, but rather these parameters have been *bounded*. The ideal sheet conductivity for the Slessor Glacier area should be $< 10^{-3}$ m$^{7/4}$m$^{-1/2}$, and the ideal channel conductivity should be $\geq 5 \times 10^{-2}$ m$^{3/4}$kg$^{-1/2}$. To constrain further, a wider range of values should be tested, however, due to the high computational demand and time necessary to run a very wide range of values, the values suggested here are deemed sufficient for the scope of this project.

Applying a sensitivity test along with a comparison of ice dynamics model outputs and, if available, observed data provide a tractable means of model validation to Antarctic subglacial hydrology modeling projects. Additional means of model validation are crucial for Antarctic glaciological modeling as completely coupling ice dynamics to subglacial hydrology has not yet been achieved, and furthermore, several important parameters remain poorly constrained both spatially and temporally due to data being difficult to acquire beneath the AIS.

Chapter 5

Conclusion

5.1 General Conclusions

A suite of 48 transient subglacial hydrology runs were computed with the GlaDS subglacial hydrology model at the Slessor Glacier study area in Antarctica. Spatially variable water input and basal velocity are interpolated onto the mesh that was calculated following the methods proposed by Seroussi et al. (2020). All model configurations result in an efficient drainage system comprised of R-channels forming at two locations, one at the Slessor Glacier outlet, and another at the BIS outlet. The 48 model runs form a sensitivity test which was used to investigate the effects of varying sheet conductivity, channel conductivity, water input, and basal velocity. Sheet conductivity and water input had a dramatic impact on the configuration and extent of the efficient drainage system; a constant water input following a linear ramp up scheme or a low value of sheet conductivity resulted in the spatial extent of the efficient drainage system increasing from $\sim$ 190 km upglacier from the grounding line to $>$ 500 km. Channel conductivity imposed a control on the rate of discharge exiting the grounding line, as well as the arboresence of R-channels forming in the efficient drainage system. Finally, the constant basal velocity altered the effective pressure of model runs as it is directly linked to the cavity opening rate of the distributed drainage mode.

The ice dynamics model, ISSM, was used to infer ice rigidity of the floating Filchner Ice Shelf as well as the of basal friction coefficient beneath the Slessor Glacier study area from three different friction laws. The Weertman friction law is related to sliding velocity and basal shear stress, and the Budd and Schoof friction laws introduce an effective pressure term in their parameterizations, and for this value, the modeled effective pressure at the end of each base run was used, resulting in 13 basal friction coefficient inversion simulations. The recovered velocities from the stress balance simulations and low values of the basal friction coefficient persisting from the grounding line up to the tributaries of Slessor Glacier suggest that much of the ice motion at inland areas of Slessor Glacier is a consequence of basal sliding rather than the internal deformation of ice. This is consistent with findings by others (e.g., Morlighem et al., 2013; Arthern et al., 2015).

It has been demonstrated that when the appropriate friction law is selected, inverse method results can effectively be used as an additional source of model validation, and can help determine the most appropriate parameterization of the GlaDS subglacial hydrology at Slessor Glacier, and likely in other areas as well. This is a particularly helpful method when observed data (e.g., specularity content) are not available to the modeler, and a direct comparison of model output like water volume and effective pressure is not possible. By normalizing the inferred basal friction coefficient and effective pressure, both of which are expected to be low in areas of fast observed ice flow, the parameterizations most likely to be representing reality in the study area can be determined using a Budd friction law.

To support this choice of parameterization, discharge rates at the Slessor Glacier and BIS grounding line are compared to areas of locally high shelf melt rates as well as locations of basal channels on the floating Filchner Ice Shelf. The GlaDS model successfully reproduces high discharge at two of the three locations of locally high shelf melt rates on the Slessor Glacier and BIS grounding line across all 48 transient runs. Inverting 25 m-resolution REMA surface data reveals the location of several ice shelf basal channels that correspond to the areas of modeled channel discharge on the grounding line as well as areas of high shelf melt rates. From these results, the higher two of the three tested values of channel conductivity are deemed most appropriate.

Without direct measurements of sheet and channel conductivity, it is not possible to completely constrain sheet and channel conductivity, as well as other model parameters. To this end, it is suggested that an appropriate range of values or bound is determined as opposed to specific values, and for this project, a sheet conductivity $< 10^{-3}$ m$^{7/4}$kg$^{-1/2}$ and a channel conductivity $\geq 5 \times 10^{-2}$ m$^{7/4}$kg$^{-1/2}$ are the presented appropriate values determined from the sensitivity test, comparison with the inferred Budd basal friction coefficient, and direct comparison to observed shelf melt rate and ice shelf basal channel locations.

The results from the hydrology and ice dynamics models are compared with previously measured and/or modeled subglacial water flux, subglacial lake locations, and coefficient of basal friction. Le Brocq et al. (2013) and Willis et al. (2016) modeled Antarctic-wide subglacial water flux, and while some values are consistent with what is modeled in this projects, others are off by as much as 14.1 m^{3}s^{-1}. This is likely due to differences in drainage basin area, calculations based on assuming ice overburden pressure everywhere, representation of the efficient and distributed drainage, and volumes of water input. Despite this modeling project not being ideal to represent subglacial lakes, the outputs from the base runs correspond well with three subglacial lake locations from Smith et al. (2009) and Livingstone et al. (2022), as well as a fourth location that has not been recorded on any of the subglacial lake inventories. Finally, the coefficient of basal friction is compared to Antarctic-wide inversion simulations. The inverse methods used here successfully reproduce the areas of high and low basal friction coefficient as predicted by Morlighem et al. (2013) and Arthern et al. (2015).

Inferred channels on the base of the Filchner Ice Shelf have implications for future sea level rise from this area. Dow et al. (2018c) demonstrated that ice shelf thinning due to basal channels played a major role in fracturing on the Nansen ice shelf which led to a

large calving event, and further fracturing post-calving. Moreover, the inversion simulation over the Filchner Ice Shelf produces variable ice rigidity, notably on either side of two rifts (figure 4.6) - ice shelf features that are known a precursor to iceberg calving (Li et al., 2017). Furthermore, Khazendar et al. (2007) demonstrated that a variable ice rigidity played a key role in the disintegration of Larsen B Ice Shelf, and large calving events have occurred on the Filchner Ice Shelf in the past: three large tabular icebergs with a total area of ~ 11500 km^2 calved off of the Filchner Ice Shelf in 1986 (Li et al., 2017).

The removal of the Filchner Ice Shelf would have two major implications for Slessor Glacier and the BIS. First, the grounding line of these two glaciers host low friction and effective pressure, and a lack of back-stress from an ice shelf would likely result in a large flux of ice flowing directly into the ocean. Second, both Slessor Glacier and the BIS are situated on retrograde slopes (more pronounced for Slessor Glacier), meaning the loss of a fringing ice shelf could result in fast, unstable grounding line retreat.

To summarize the points made in the last two paragraphs, the following features motivate further investigation of Slessor Glacier, BIS, and the Filchner Ice Shelf, especially considering rising global average surface and ocean temperatures:

- A low coefficient of friction and effective pressure at the Slessor Glacier/BIS grounding line,

- a variable ice rigidity field inferred on the Filchner Ice Shelf,

- the presence of several basal channels and two rifts on the Filchner Ice Shelf,

- a history of calving events in this area,

- and Slessor Glacier and BIS containing sea level equivalents of 2.92 ± 0.04 m and 0.209 ± 0.06 m of ice, respectively (Morlighem et al., 2020).

5.2 Improvements and Future Work

This project, and others like it, provide insight into directions that future work should take in the field of subglacial hydrology and ice dynamics modeling.

For subglacial hydrology modeling, there are several issues that should be addressed. Areas that host locally high bed elevation, thin ice, and large gradients in topography remain as problematic areas in subglacial hydrology modeling, yet there is no agreed upon method for how to handle these areas. Moreover, some common practices such as imposing a minimum ice thickness, a maximum bed elevation, and/or topographic smoothing result in small-scale features not being represented, and when synthetic topography is imposed, small-scale features are misrepresented. In the future, modelers should look into treating these areas specifically in the models, or at the very least, coming to a consensus on how to consistently mediate these issues by altering the topography.

The design of the sensitivity test in this project could also be expanded upon in several ways. Hager et al. (2021) consider two additional parameters in their sensitivity test, the

maximum bedrock bump height (h_r in the GlaDS model) and the bed roughness, both of which exhibit controls on the subglacial drainage system. Furthermore, the maximum channel CSA of the channels was set to 500 m² to ensure numerical stability of the model, despite this limit not existing in reality. Finally, for both the ice dynamics and subglacial hydrology model, including at least one other model of each type would be an effective way to reduce model bias (e.g., the Shakti subglacial hydrology model (Sommers et al., 2018) or the Toolkit for Advanced Optimization (TAO) inversion method within ISSM (Munson et al., 2012)), and increase confidence in conclusions based on model outputs.

The model validation technique of comparing subglacial hydrology and ice dynamics models can be improved by testing this in regions such as Greenland and mountain glaciers where more data exists, as well as other locations in Antarctica that others have previously modeled (e.g., Thwaites Glacier). Ensuring this method is effective in areas with lots of relevant observed data would prove to be a worthwhile endeavour as any additional means of model validation to Antarctic modelers is beneficial. Moreover, the results from this study suggest the Budd friction law is predicting a basal friction coefficient that is most consistent with the effective pressure and observed ice shelf data, despite the law erroneously implying basal drag can reach arbitrarily high values. This is surprising as the Schoof friction law directly addressed this issue, and it would be expected that this law would provide more realistic outputs than the Weertman and Budd friction laws. To this end, it is likely that further investigation of basal friction laws should be considered at other glaciers with different geometries, basal sediment/bed rock compositions, etc.

Future work in the Slessor Glacier study area should look into modeling subglacial lake activity following a model setup similar to Dow et al. (2018a) at Recovery Glacier. Slessor Glacier hosts several active subglacial lakes, and to understand the subglacial hydrological system beneath it, the impact the lakes draining and filling must be understood and well represented. In addition, there is an area on the grounding line where no significant channel discharge was simulated yet ice shelf melt rates are high (Adusumilli et al., 2020), and there is disagreement between whether or not the tributaries are moving due basal slip as modeled in this study and by others (Morlighem et al., 2013; Arthern et al., 2015), or ice deformation (Rippin et al., 2006).

There are two fundamental next steps that need to be taken in order for major improvements to be made to modeling in glaciology. The first, and most important, is for data collection to catch up to the pace of model creation and methodology. The sheet and channel conductivity in particular have major implications for the configurations of drainage networks, yet remain poorly constrained both temporally and spatially. Model outputs are limited by the assumptions they make and the quality of the data they have, and conclusions drawn from those outputs must bear in mind that model validation is difficult, especially in Antarctica. The second major step is to completely, and efficiently couple subglacial hydrology to ice dynamics, and reduce the number of assumptions. Recent work has shown that coupling subglacial hydrology to ice dynamics is possible (e.g., Pimentel and Flowers, 2011; Hoffman and Price, 2014; Cook et al., 2020), however these models are simplified versions based on assumptions that limit how representative of reality the outputs are.

The work and results provided in this thesis demonstrate appropriate configurations of the subglacial hydrological network, as well as determine ice rigidity and basal drag coefficient fields at Slessor Glacier, East Antarctica. Additionally, a new method of subglacial hydrology model validation is proposed by comparing outputs from an ice dynamics model based on inverse methods. In the most general sense, the results and methods used in this thesis aid the scientific community in understanding the evolution of ice masses in Antarctica, which will play a major role in global sea level rise in the future.

References

Adusumilli, S., Fricker, H. A., Medley, B., Padman, L., and Siegfried, M. R. Interannual variations in meltwater input to the southern ocean from Antarctic ice shelves. *Nature Geoscience*, 13(9):616–620, 2020. doi: 10.1038/s41561-020-0616-z.

Alley, R. B., Lawson, D. E., Larson, G. J., Evenson, E. B., and Baker, G. S. Stabilizing feedbacks in glacier-bed erosion. *Nature*, 424(6950):758–760, 2003. doi: 10.1038/nature01839.

Arthern, R. J., Hindmarsh, R. C. A., and Williams, C. R. Flow speed within the Antarctic Ice Sheet and its controls inferred from satellite observations. *Journal of Geophysical Research: Earth Surface*, 120(7):1171–1188, 2015. doi: https://doi.org/10.1002/2014JF003239.

Ashmore, D. W. and Bingham, R. G. Antarctic subglacial hydrology: current knowledge and future challenges. *Antarctic Science*, 26(6):758–773, 2014. doi: 10.1017/S0954102014000546.

Babaniyi, O., Nicholson, R., Villa, U., and Petra, N. Inferring the basal sliding coefficient field for the stokes ice sheet model under rheological uncertainty. *The Cryosphere*, 15 (4):1731–1750, 2021. doi: 10.5194/tc-15-1731-2021.

Bakker, P., Clark, P. U., Golledge, N. R., Schmittner, A., and Weber, M. E. Centennial-scale holocene climate variations amplified by Antarctic Ice Sheet discharge. *Nature*, 541 (7635):72–76, 2017. doi: 10.1038/nature20582.

Bamber, J. L., Riva, R. E. M., Vermeersen, B. L. A., and LeBrocq, A. M. Reassessment of the potential sea-level rise from a collapse of the West Antarctic Ice Sheet. *Science*, 324(5929):901–903, 2009. doi: 10.1126/science.1169335.

Barnes, J. M., Dias dos Santos, T., Goldberg, D., Gudmundsson, G. H., Morlighem, M., and De Rydt, J. The transferability of adjoint inversion products between different ice flow models. *The Cryosphere*, 15(4):1975–2000, 2021. doi: 10.5194/tc-15-1975-2021.

Brinkerhoff, D., Aschwanden, A., and Fahnestock, M. Constraining subglacial processes from surface velocity observations using surrogate-based bayesian inference. *Journal of Glaciology*, 67(263):385–403, 2021. doi: 10.1017/jog.2020.112.

Brondex, J., Gagliardini, O., Gillet-Chaulet, F., and Durand, G. Sensitivity of grounding line dynamics to the choice of the friction law. *Journal of Glaciology*, 63(241):854–866, 2017. doi: 10.1017/jog.2017.51.

Budd, W. F., Keage, P. L., and Blundy, N. A. Empirical studies of ice sliding. *Journal of Glaciology*, 23(89):157–170, 1979. doi: 10.3189/S0022143000029804.

Budd, W. and Jacka, T. A review of ice rheology for ice sheet modelling. *Cold Regions Science and Technology*, 16(2):107–144, 1989. ISSN 0165-232X. doi: https://doi.org/10.1016/0165-232X(89)90014-1.

Burton-Johnson, A., Dziadek, R., and Martin, C. Review article: Geothermal heat flow in Antarctica: current and future directions. *The Cryosphere*, 14(11):3843–3873, 2020. doi: 10.5194/tc-14-3843-2020.

Clarke, G. K. Subglacial processes. *Annual Review of Earth and Planetary Sciences*, 33 (1):247–276, 2005. doi: 10.1146/annurev.earth.33.092203.122621.

Cook, S. J., Christoffersen, P., Todd, J., Slater, D., and Chauché, N. Coupled modelling of subglacial hydrology and calving-front melting at Store Glacier, West Greenland. *The Cryosphere*, 14(3), 2020. doi: 10.5194/tc-14-905-2020.

Cook, S. J. and Swift, D. A. Subglacial basins: Their origin and importance in glacial systems and landscapes. *Earth-Science Reviews*, 115(4):332–372, 2012. ISSN 0012-8252. doi: https://doi.org/10.1016/j.earscirev.2012.09.009.

Creyts, T. T. and Schoof, C. G. Drainage through subglacial water sheets. *Journal of Geophysical Research: Earth Surface*, 114(F4), 2009. doi: https://doi.org/10.1029/2008JF001215.

Cuffey, L. M. and Paterson, W. S. B. *The physics of glaciers (4th ed.)*. Butterworth-Heinemann/Elsevier, 2010.

De Fleurian, B., Werder, M. A., Beyer, S., Brinkerhoff, D. J., Delaney, I., Doe, C. F., Downs, J., Gagliardini, O., Hoffman, M. J., Hooke, R. L., and et al. SHMIP the subglacial hydrology model intercomparison project. *Journal of Glaciology*, 64(248):897–916, 2018. doi: 10.1017/jog.2018.78.

Diez, A., Matsuoka, K., Ferraccioli, F., Jordan, T. A., Corr, H. F., Kohler, J., Olesen, A. V., and Forsberg, R. Basal settings control fast ice flow in the Recovery/Slessor/Bailey region, East Antarctica. *Geophysical Research Letters*, 45(6):2706–2715, 2018. doi: https://doi.org/10.1002/2017GL076601.

Dow, C. F., Werder, M. A., Nowicki, S., and Walker, R. T. Modeling Antarctic subglacial lake filling and drainage cycles. *The Cryosphere*, 10(4):1381–1393, 2016. doi: 10.5194/tc-10-1381-2016.

Dow, C. F., Werder, M. A., Babonis, G., Nowicki, S., Walker, R. T., Csatho, B., and Morlighem, M. Dynamics of active subglacial lakes in Recovery Ice Stream. *Journal of Geophysical Research: Earth Surface*, 123(4):837–850, 2018a. doi: https://doi.org/10.1002/2017JF004409.

Dow, C., McCormack, F., Young, D., Greenbaum, J., Roberts, J., and Blankenship, D. Totten Glacier subglacial hydrology determined from geophysics and modeling. *Earth and Planetary Science Letters*, 531:115961, 2020. ISSN 0012-821X. doi: https://doi.org/10.1016/j.epsl.2019.115961.

Dow, C. F., Kavanaugh, J. L., Sanders, J. W., and Cuffey, K. M. A test of common assumptions used to infer subglacial water flow through overdeepenings. *Journal of Glaciology*, 60(222):725–734, 2014. doi: 10.3189/2014JoG14J027.

Dow, C. F., Karlsson, N. B., and Werder, M. A. Limited impact of subglacial supercooling freeze-on for Greenland ice sheet stratigraphy. *Geophysical Research Letters*, 45(3):1481–1489, 2018b. doi: https://doi.org/10.1002/2017GL076251.

Dow, C. F., Lee, W. S., Greenbaum, J. S., Greene, C. A., Blankenship, D. D., Poinar, K., Forrest, A. L., Young, D. A., and Zappa, C. J. Basal channels drive active surface hydrology and transverse ice shelf fracture. *Science Advances*, 4(6):eaao7212, 2018c. doi: 10.1126/sciadv.aao7212.

Echelmeyer, K. A., Harrison, W. D., Larsen, C., and Mitchell, J. E. The role of the margins in the dynamics of an active ice stream. *Journal of Glaciology*, 40(136):527–538, 1994. doi: 10.3189/S0022143000012417.

Edwards, T. L., Nowicki, S., Marzeion, B., Hock, R., Goelzer, H., Seroussi, H., Jourdain, N. C., Slater, D. A., Turner, F. E., Smith, C. J., McKenna, C. M., Simon, E., Abe-Ouchi, A., Gregory, J. M., Larour, E., Lipscomb, W. H., Payne, A. J., Shepherd, A., Agosta, C., Alexander, P., Albrecht, T., Anderson, B., Asay-Davis, X., Aschwanden, A., Barthel, A., Bliss, A., Calov, R., Chambers, C., Champollion, N., Choi, Y., Cullather, R., Cuzzone, J., Dumas, C., Felikson, D., Fettweis, X., Fujita, K., Galton-Fenzi, B. K., Gladstone, R., Golledge, N. R., Greve, R., Hattermann, T., Hoffman, M. J., Humbert, A., Huss, M., Huybrechts, P., Immerzeel, W., Kleiner, T., Kraaijenbrink, P., Le clec'h, S., Lee, V., Leguy, G. R., Little, C. M., Lowry, D. P., Malles, J.-H., Martin, D. F., Maussion, F., Morlighem, M., O'Neill, J. F., Nias, I., Pattyn, F., Pelle, T., Price, S. F., Quiquet, A., Radić, V., Reese, R., Rounce, D. R., Rückamp, M., Sakai, A., Shafer, C., Schlegel, N.-J., Shannon, S., Smith, R. S., Straneo, F., Sun, S., Tarasov, L., Trusel, L. D., Van Breedam, J., van de Wal, R., van den Broeke, M., Winkelmann, R., Zekollari, H., Zhao, C., Zhang, T., and Zwinger, T. Projected land ice contributions to twenty-first-century sea level rise. *Nature*, 593(7857):74–82, 2021. doi: 10.1038/s41586-021-03302-y.

Emetc, V., Tregoning, P., Morlighem, M., Borstad, C., and Sambridge, M. A statistical fracture model for Antarctic ice shelves and glaciers. *The Cryosphere*, 12(10):3187–3213, 2018. doi: 10.5194/tc-12-3187-2018.

Fan, Y., Hao, W., Zhang, B., Ma, C., Gao, S., Shen, X., and Li, F. Monitoring the hydro-logical activities of Antarctic subglacial lakes using CryoSat-2 and ICESat-2 altimetry data. *Remote Sensing*, 14(4), 2022. ISSN 2072-4292. doi: 10.3390/rs14040898.

Flowers, G. E. Modelling water flow under glaciers and ice sheets. *Proceedings of the Royal Society A: Mathematical, Physical and Engineering Sciences*, 471(2176):20140907, 2015. doi: 10.1098/rspa.2014.0907.

Fountain, A. G. and Walder, J. S. Water flow through temperate glaciers. *Reviews of Geophysics*, 36(3):299–328, 1998. doi: https://doi.org/10.1029/97RG03579.

Fretwell, P., Pritchard, H. D., Vaughan, D. G., Bamber, J. L., Barrand, N. E., Bell, R., Bianchi, C., Bingham, R. G., Blankenship, D. D., Casassa, G., Catania, G., Callens, D., Conway, H., Cook, A. J., Corr, H. F. J., Damaske, D., Damm, V., Ferraccioli, F., Forsberg, R., Fujita, S., Gim, Y., Gogineni, P., Griggs, J. A., Hindmarsh, R. C. A., Holm-lund, P., Holt, J. W., Jacobel, R. W., Jenkins, A., Jokat, W., Jordan, T., King, E. C., Kohler, J., Krabill, W., Riger-Kusk, M., Langley, K. A., Leitchenkov, G., Leuschen, C., Luyendyk, B. P., Matsuoka, K., Mouginot, J., Nitsche, F. O., Nogi, Y., Nost, O. A., Popov, S. V., Rignot, E., Rippin, D. M., Rivera, A., Roberts, J., Ross, N., Siegert, M. J., Smith, A. M., Steinhage, D., Studinger, M., Sun, B., Tinto, B. K., Welch, B. C., Wilson, D., Young, D. A., Xiangbin, C., and Zirizzotti, A. Bedmap2: improved ice bed, surface and thickness datasets for Antarctica. *The Cryosphere*, 7(1):375–393, 2013. doi: 10.5194/tc-7-375-2013.

Fricker, H. A., Carter, S. P., Bell, R. E., and Scambos, T. Active lakes of Recovery Ice Stream, East Antarctica: a bedrock-controlled subglacial hydrological system. *Journal of Glaciology*, 60(223):1015–1030, 2014. doi: 10.3189/2014JoG14J063.

Garbe, J., Albrecht, T., Levermann, A., Donges, J. F., and Winkelmann, R. The hys-teresis of the Antarctic Ice Sheet. *Nature*, 585(7826):538–544, 2020. doi: 10.1038/s41586-020-2727-5.

Gilbert, J. C. and Lemaréchal, C. Some numerical experiments with variable-storage quasi-newton algorithms. *Mathematical Programming*, 45(1):407–435, 1989. doi: 10.1007/BF01589113.

Glen, J. W. and Perutz, M. F. The creep of polycrystalline ice. *Proceedings of the Royal Society of London. Series A. Mathematical and Physical Sciences*, 228(1175):519–538, 1955. doi: 10.1098/rspa.1955.0066.

Golledge, N. R., Levy, R. H., McKay, R. M., and Naish, T. R. East Antarctic Ice Sheet most vulnerable to Weddell Sea warming. *Geophysical Research Letters*, 44(5):2343–2351, 2017. doi: https://doi.org/10.1002/2016GL072422.

Hager, A. O., Hoffman, M. J., Price, S. F., and Schroeder, D. M. Persistent, extensive chan-nelized drainage modeled beneath Thwaites Glacier, West Antarctica. *The Cryosphere Discussions*, 2021:1–27, 2021. doi: 10.5194/tc-2021-338.

Hansen, P. C. The l-curve and its use in the numerical treatment of inverse problems. *Computational Inverse Problems in Electrocardiology*, 4:119–142, 01 2001.

Hecht, F. bamg: Bidimensional anisotropic mesh generator, 01 1998.

Herman, F., Beaud, F., Champagnac, J.-D., Lemieux, J.-M., and Sternai, P. Glacial hydrology and erosion patterns: A mechanism for carving glacial valleys. *Earth and Planetary Science Letters*, 310(3):498–508, 2011. ISSN 0012-821X. doi: https://doi.org/10.1016/j.epsl.2011.08.022.

Hewitt, I. J. Modelling distributed and channelized subglacial drainage: the spacing of channels. *Journal of Glaciology*, 57(202):302–314, 2011. doi: 10.3189/002214311796405951.

Hoffman, M. and Price, S. Feedbacks between coupled subglacial hydrology and glacier dynamics. *Journal of Geophysical Research: Earth Surface*, 119(3):414–436, 2014. doi: https://doi.org/10.1002/2013JF002943.

Hooke, R. L., Laumann, T., and Kohler, J. Subglacial water pressures and the shape of subglacial conduits. *Journal of Glaciology*, 36(122):67–71, 1990. doi: 10.3189/S0022143000005566.

Hovelsrud, G. K., Poppel, B., van Oort, B., and Reist, J. D. Arctic societies, cultures, and peoples in a changing cryosphere. *AMBIO*, 40(1):100–110, 2011. doi: 10.1007/s13280-011-0219-4.

Howat, I. M., Porter, C., Smith, B. E., Noh, M.-J., and Morin, P. The reference elevation model of Antarctica. *The Cryosphere*, 13(2):665–674, 2019. doi: 10.5194/tc-13-665-2019.

Hui, F., Ci, T., Cheng, X., Scambo, T. A., Liu, Y., Zhang, Y., Chi, Z., Huang, H., Wang, X., Wang, F., and et al. Mapping blue-ice areas in Antarctica using ETM and MODIS data. *Annals of Glaciology*, 55(66):129–137, 2014. doi: 10.3189/2014AoG66A069.

Iken, A. The effect of the subglacial water pressure on the sliding velocity of a glacier in an idealized numerical model. *Journal of Glaciology*, 27(97):407–421, 1981. doi: 10.3189/S0022143000011448.

Iken, A. and Bindschadler, R. A. Combined measurements of subglacial water pressure and surface velocity of Findelengletscher, Switzerland: Conclusions about drainage system and sliding mechanism. *Journal of Glaciology*, 32(110):101–119, 1986. doi: 10.3189/S0022143000006936.

Indrigo, C., Dow, C. F., Greenbaum, J. S., and Morlighem, M. Drygalski Ice Tongue stability influenced by rift formation and ice morphology. *Journal of Glaciology*, 67(262):243–252, 2021. doi: 10.1017/jog.2020.99.

Joughin, I., Smith, B. E., and Holland, D. M. Sensitivity of 21st century sea level to ocean-induced thinning of Pine Island Glacier, Antarctica. *Geophysical Research Letters*, 37(20), 2010. doi: https://doi.org/10.1029/2010GL044819.

Khazendar, A., Rignot, E., and Larour, E. Larsen b ice shelf rheology preceding its disintegration inferred by a control method. *Geophysical Research Letters*, 34(19), 2007. doi: https://doi.org/10.1029/2007GL030980.

Koike, K, Yoshida, H., Omura, M., Shibuya, K., and Doi, K. Temporal changes in crevasses in the middle Slessor Glacier, Coats Land, East Antarctica through SAR data analysis. *Earth, Planets and Space*, 64(3):257–267, 2012. doi: 10.5047/eps.2011.10.003.

Larour, E., Seroussi, H., Morlighem, M., and Rignot, E. Continental scale, high order, high spatial resolution, ice sheet modeling using the Ice Sheet System Model (issm). *Journal of Geophysical Research: Earth Surface*, 117(F1), 2012. doi: https://doi.org/10.1029/2011JF002140.

Le Brocq, A. M., Ross, N., Griggs, J. A., Bingham, R. G., Corr, H. F. J., Ferraccioli, F., Jenkins, A., Jordan, T. A., Payne, A. J., Rippin, D. M., and Siegert, M. J. Evidence from ice shelves for channelized meltwater flow beneath the Antarctic Ice Sheet. *Nature Geoscience*, 6(11):945–948, 2013. doi: 10.1038/ngeo1977.

Li, R., Xiao, H., Liu, S., and Tong, X. A systematic study of the fracturing of Ronne - Filchner Ice Shelf, Antarctica, using multisource satellite data from 2001 to 2016. *The Cryosphere Discussions*, 2017:1–38, 2017. doi: 10.5194/tc-2017-178.

Livingstone, S. J., Li, Y., Rutishauser, A., Sanderson, R. J., Winter, K., Mikucki, J. A., Björnsson, H., Bowling, J. S., Chu, W., Dow, C. F., Fricker, H. A., McMillan, M., Ng, F. S. L., Ross, N., Siegert, M. J., Siegfried, M., and Sole, A. J. Subglacial lakes and their changing role in a warming climate. *Nature Reviews Earth & Environment*, 3(2): 106–124, 2022. doi: 10.1038/s43017-021-00246-9.

Lliboutry, L. Physical processes in temperate glaciers. *Journal of Glaciology*, 16(74): 151–158, 1976. doi: 10.3189/S002214300003149X.

MacAyeal, D. R. The basal stress distribution of Ice Stream E, Antarctica, inferred by control methods. *Journal of Geophysical Research: Solid Earth*, 97(B1):595–603, 1992. doi: https://doi.org/10.1029/91JB02454.

McMillan, M., Corr, H., Shepherd, A., Ridout, A., Laxon, S., and Cullen, R. Three-dimensional mapping by CryoSat-2 of subglacial lake volume changes. *Geophysical Research Letters*, 40(16):4321–4327, 2013. doi: https://doi.org/10.1002/grl.50689.

Morlighem, M., Seroussi, H., Larour, E., and Rignot, E. Inversion of basal friction in Antarctica using exact and incomplete adjoints of a higher-order model. *Journal of Geophysical Research: Earth Surface*, 118(3):1746–1753, 2013. doi: https://doi.org/10.1002/jgrf.20125.

Morlighem, M., Rignot, E., Binder, T., Blankenship, D., Drews, R., Eagles, G., Eisen, O., Ferraccioli, F., Forsberg, R., Fretwell, P., Goel, V., Greenbaum, J. S., Gudmundsson, H., Guo, J., Helm, V., Hofstede, C., Howat, I., Humbert, A., Jokat, W., Karlsson, N. B., Lee, W. S., Matsuoka, K., Millan, R., Mouginot, J., Paden, J., Pattyn, F., Roberts, J.,

Rosier, S., Ruppel, A., Seroussi, H., Smith, E. C., Steinhage, D., Sun, B., Broeke, M. R. v. d., Ommen, T. D. v., Wessem, M. v., and Young, D. A. Deep glacial troughs and stabilizing ridges unveiled beneath the margins of the Antarctic ice sheet. *Nature Geoscience*, 13(2):132–137, 2020. doi: 10.1038/s41561-019-0510-8.

Mouginot, J., Rignot, E., and Scheuchl, B. Continent-wide, interferometric sar phase, mapping of Antarctic ice velocity. *Geophysical Research Letters*, 46(16):9710–9718, 2019. doi: https://doi.org/10.1029/2019GL083826.

Munson, T., Sarich, J., Wild, S., Benson, S., and McInnes, L. C. Tao 2.0 users manual. Technical Report ANL/MCS-TM-322, Mathematics and Computer Science Division, Argonne National Laboratory, 2012. http://www.mcs.anl.gov/tao.

Nardi, L., Sorror, C., Badran, F., and Thiria, S. Yao: A software for variational data assimilation using numerical models. In Gervasi, O., Taniar, D., Murgante, B., Laganà, A., Mun, Y., and Gavrilova, M. L., editors, *Computational Science and Its Applications – ICCSA 2009*, pages 621–636, Berlin, Heidelberg, 2009. Springer Berlin Heidelberg.

Paolo, F. S., Fricker, H. A., and Padman, L. Volume loss from Antarctic ice shelves is accelerating. *Science*, 348(6232):327–331, 2015. doi: 10.1126/science.aaa0940.

Pattyn, F. Antarctic subglacial conditions inferred from a hybrid ice sheet/ice stream model. *Earth and Planetary Science Letters*, 295(3):451–461, 2010. ISSN 0012-821X. doi: https://doi.org/10.1016/j.epsl.2010.04.025.

Paxman, G. J. G., Jamieson, S. S. R., Ferraccioli, F., Bentley, M. J., Forsberg, R., Ross, N., Watts, A. B., Corr, H. F. J., and Jordan, T. A. Uplift and tilting of the Shackleton Range in East Antarctica driven by glacial erosion and normal faulting. *Journal of Geophysical Research: Solid Earth*, 122(3):2390–2408, 2017. doi: https://doi.org/10.1002/2016JB013841.

Pimentel, S. and Flowers, G. E. A numerical study of hydrologically driven glacier dynamics and subglacial flooding. *Proceedings of the Royal Society A: Mathematical, Physical and Engineering Sciences*, 467(2126):537–558, 2011. doi: 10.1098/rspa.2010.0211.

Prior-Jones, M. R., Bagshaw, E. A., Lees, J., Clare, L., Burrow, S., Werder, M. A., Karlsson, N. B., Dahl-Jensen, D., Chudley, T. R., Christoffersen, P., and et al. Cryoegg: development and field trials of a wireless subglacial probe for deep, fast-moving ice. *Journal of Glaciology*, 67(264):627–640, 2021. doi: 10.1017/jog.2021.16.

Pritchard, H. D., Ligtenberg, S. R. M., Fricker, H. A., Vaughan, D. G., van den Broeke, M. R., and Padman, L. Antarctic ice-sheet loss driven by basal melting of ice shelves. *Nature*, 484(7395):502–505, 2012. doi: 10.1038/nature10968.

Ranganathan, M., Minchew, B., Meyer, C. R., and Gudmundsson, G. H. A new approach to inferring basal drag and ice rheology in ice streams, with applications to West Antarctic ice streams. *Journal of Glaciology*, 67(262):229–242, 2021. doi: 10.1017/jog.2020.95.

Reeves, G. smooth2a,(https://www.mathworks.com/matlabcentral/fileexchange/23287-smooth2a). MATLAB Central File Exchange. Retrieved June 11, 2022., 2022.

Rignot, E., Mouginot, J., and Scheuchl, B. Ice flow of the Antarctic Ice Sheet. *Science*, 333(6048):1427–1430, 2011. doi: 10.1126/science.1208336.

Rignot, E., Bamber, J. L., van den Broeke, M. R., Davis, C., Li, Y., van de Berg, W. J., and van Meijgaard, E. Recent Antarctic ice mass loss from radar interferometry and regional climate modelling. *Nature Geoscience*, 1(2):106–110, 2008. doi: 10.1038/ngeo102.

Rippin, D., Bamber, J., Siegert, M., Vaughan, D., and Corr, H. Basal conditions beneath enhanced-flow tributaries of Slessor Glacier, East Antarctica. *Journal of Glaciology*, 52 (179):481–490, 2006. doi: 10.3189/172756506781828467.

Röthlisberger, H. Water pressure in intra- and subglacial channels. *Journal of Glaciology*, 11(62):177–203, 1972. doi: 10.3189/S0022143000022188.

Schoof, C. The effect of cavitation on glacier sliding. *Proceedings of the Royal Society A: Mathematical, Physical and Engineering Sciences*, 461(2055):609–627, 2005. doi: 10.1098/rspa.2004.1350.

Schoof, C. Ice sheet grounding line dynamics: Steady states, stability, and hysteresis. *Journal of Geophysical Research: Earth Surface*, 112(F3), 2007. doi: https://doi.org/10.1029/2006JF000664.

Schoof, C. Ice-sheet acceleration driven by melt supply variability. *Nature*, 468(7325): 803–806, 2010. doi: 10.1038/nature09618.

Schroeder, D. M., Blankenship, D. D., Raney, R. K., and Grima, C. Estimating subglacial water geometry using radar bed echo specularity: Application to Thwaites Glacier, West Antarctica. *IEEE Geoscience and Remote Sensing Letters*, 12(3):443–447, 2015. doi: 10.1109/LGRS.2014.2337878.

Schwanghart, W. and Scherler, D. TopoToolbox 2 – MATLAB-based software for topographic analysis and modeling in Earth surface sciences. *Earth Surface Dynamics*, 2: 1–7, 2014. doi: 10.5194/esurf-2-1-2014.

Seroussi, H., Nowicki, S., Payne, A. J., Goelzer, H., Lipscomb, W. H., Abe-Ouchi, A., Agosta, C., Albrecht, T., Asay-Davis, X., Barthel, A., Calov, R., Cullather, R., Dumas, C., Galton-Fenzi, B. K., Gladstone, R., Golledge, N. R., Gregory, J. M., Greve, R., Hattermann, T., Hoffman, M. J., Humbert, A., Huybrechts, P., Jourdain, N. C., Kleiner, T., Larour, E., Leguy, G. R., Lowry, D. P., Little, C. M., Morlighem, M., Pattyn, F., Pelle, T., Price, S. F., Quiquet, A., Reese, R., Schlegel, N.-J., Shepherd, A., Simon, E., Smith, R. S., Straneo, F., Sun, S., Trusel, L. D., Van Breedam, J., van de Wal, R. S. W., Winkelmann, R., Zhao, C., Zhang, T., and Zwinger, T. ISMIP6 Antarctica: a multi-model ensemble of the Antarctic ice sheet evolution over the 21st century. *The Cryosphere*, 14(9):3033–3070, 2020. doi: 10.5194/tc-14-3033-2020.

Shepherd, T., Bamber, J., and Ferraccioli, F. Subglacial geology in Coats Land, East Antarctica, revealed by airborne magnetics and radar sounding. *Earth and Planetary Science Letters*, 244(1):323–335, 2006. ISSN 0012-821X. doi: https://doi.org/10.1016/j.epsl.2006.01.068.

Shewchuk, J. R. Delaunay refinement algorithms for triangular mesh generation. *Computational Geometry*, 22(1):21–74, 2002. ISSN 0925-7721. doi: https://doi.org/10.1016/S0925-7721(01)00047-5. 16th ACM Symposium on Computational Geometry.

Shreve, R. L. Movement of water in glaciers. *Journal of Glaciology*, 11(62):205–214, 1972. doi: 10.3189/S002214300002219X.

Siegert, M. J. Lakes beneath the ice sheet: The occurrence, analysis, and future exploration of Lake Vostok and other Antarctic subglacial lakes. *Annual Review of Earth and Planetary Sciences*, 33(1):215–245, 2005. doi: 10.1146/annurev.earth.33.092203.122725.

Siegfried, M. R. and Fricker, H. A. Thirteen years of subglacial lake activity in Antarctica from multi-mission satellite altimetry. *Annals of Glaciology*, 59(76pt1):42–55, 2018. doi: 10.1017/aog.2017.36.

Siegfried, M. R., Schroeder, D. M., and Sauthoff, W. *Investigating a large subglacial lake drainage in East Antarctica with ice-penetrating radar*, pages 3120–3124. 2021. doi: 10.1190/segam2021-3582777.1.

Smith, B. E., Fricker, H. A., Joughin, I. R., and Tulaczyk, S. An inventory of active subglacial lakes in Antarctica detected by icesat (2003–2008). *Journal of Glaciology*, 55(192):573–595, 2009. doi: 10.3189/002214309789470879.

Sommers, A., Rajaram, H., and Morlighem, M. Shakti: Subglacial hydrology and kinetic, transient interactions v1.0. *Geoscientific Model Development*, 11(7):2955–2974, 2018. doi: 10.5194/gmd-11-2955-2018.

Stål, T., Reading, A. M., Halpin, J. A., and Whittaker, J. M. Antarctic geothermal heat flow model: Aq1. *Geochemistry, Geophysics, Geosystems*, 22(2):e2020GC009428, 2021. doi: https://doi.org/10.1029/2020GC009428. e2020GC009428 2020GC009428.

Sun, S., Pattyn, F., Simon, E. G., Albrecht, T., Cornford, S., Calov, R., Dumas, C., Gillet-Chaulet, F., Goelzer, H., Golledge, N. R., and et al. Antarctic Ice Sheet response to sudden and sustained ice-shelf collapse (ABUMIP). *Journal of Glaciology*, 66(260):891–904, 2020. doi: 10.1017/jog.2020.67.

Thomas, R. H., Sanderson, T. J. O., and Rose, K. E. Effect of climatic warming on the west Antarctic Ice Sheet. *Nature*, 277(5695):355–358, 1979. doi: 10.1038/277355a0.

van den Broeke, M., van de Berg, W. J., and van Meijgaard, E. Firn depth correction along the Antarctic grounding line. *Antarctic Science*, 20(5):513–517, 2008. doi: 10.1017/S095410200800148X.

Van Wessem, J. M. and Laffin, M. K. Regional Atmospheric Climate Model 2 (RACMO2), version 2.3p2 (2.3pw) [data set], 2020.

Van Wessem, J., Reijmer, C., Morlighem, M., Mouginot, J., Rignot, E., Medley, B., Joughin, I., Wouters, B., Depoorter, M., Bamber, J., and et al. Improved representation of east Antarctic surface mass balance in a regional atmospheric climate model. *Journal of Glaciology*, 60(222):761–770, 2014. doi: 10.3189/2014JoG14J051.

Walder, J. S. Röthlisberger channel theory: its origins and consequences. *Journal of Glaciology*, 56(200):1079–1086, 2010. doi: 10.3189/002214311796406031.

Weertman, J. On the sliding of glaciers. *Journal of Glaciology*, 3(21):33–38, 1957. doi: 10.3189/S0022143000024709.

Wei, W., Blankenship, D. D., Greenbaum, J. S., Gourmelen, N., Dow, C. F., Richter, T. G., Greene, C. A., Young, D. A., Lee, S., Kim, T.-W., Lee, W. S., and Assmann, K. M. Getz Ice Shelf melt enhanced by freshwater discharge from beneath the West Antarctic Ice Sheet. *The Cryosphere*, 14(4):1399–1408, 2020. doi: 10.5194/tc-14-1399-2020.

Werder, M. A. The hydrology of subglacial overdeepenings: A new supercooling threshold formula. *Geophysical Research Letters*, 43(5):2045–2052, 2016. doi: https://doi.org/10. 1002/2015GL067542.

Werder, M. A., Hewitt, I. J., Schoof, C. G., and Flowers, G. E. Modeling channelized and distributed subglacial drainage in two dimensions. *Journal of Geophysical Research: Earth Surface*, 118(4):2140–2158, 2013. doi: https://doi.org/10.1002/jgrf.20146.

Wilkens, N., Behrens, J., Kleiner, T., Rippin, D., Rückamp, M., and Humbert, A. Thermal structure and basal sliding parametrisation at Pine Island Glacier – a 3-D full-Stokes model study. *The Cryosphere*, 9(2):675–690, 2015. doi: 10.5194/tc-9-675-2015.

Willis, I. C., Pope, E. L., Leysinger Vieli, G. J.-M., Arnold, N. S., and Long, S. Drainage networks, lakes and water fluxes beneath the Antarctic Ice Sheet. *Annals of Glaciology*, 57(72):96–108, 2016. doi: 10.1017/aog.2016.15.

Wright, A. and Siegert, M. A fourth inventory of Antarctic subglacial lakes. *Antarctic Science*, 24(6):659–664, 2012. doi: 10.1017/S095410201200048X.